

**MS Imaging of Antibiotics within *Staph. epidermidis* Bacterial Biofilms by Laser
Desorption Postionization**

BY

GERALD LYNN GASPER

B.S., University of Illinois at Chicago, 2005

M.S., University of Illinois at Chicago, 2007

THESIS

Submitted as partial fulfillment of requirements
for the degree of Doctor of Philosophy in Chemistry
in the Graduate College of the
University of Illinois at Chicago, 2011

Chicago, Illinois

Defense Committee:

Luke Hanley, Chair and Advisor
Mike Trenary
Tim Keiderling
Scott Shippy
Jerry Moore, MassThink

This thesis is dedicated to the many individuals in my life that have mentored me knowingly and unknowingly while diligently keeping me on a path both balanced and focused.

Thank you all for guiding and inspiring me along this most turbulent journey.

J. Gasper Sr., D. Sunseri, J. Carroll, Dr. K. Stagliano, P.E. Kennedy III., J. Adolphus,
Franco and Fede, A.M. Gasper, J. Behnke, Sgt. S. Fields, J. Erikson,

Dr. L. Hanley, Dr. A. Roy, D. Ray, J. DiNuzzo, N.S. Gasper.

“Scientists wonder how certain things work, so they try more and more to find out how and why. Whether or not their work will lead to something useful, they don’t care, because they don’t know, and for that matter, they’re not that interested. If you develop science only with the idea to do something useful, then your chances of discovering something useful are less than if you apply your mind to finding something essential.”

-Gerhard Herzberg

ACKNOWLEDGEMENTS

To my father whose introduction to chemistry along with endless intellectual support allowed me to foster and pursue my love of science. I am grateful for the mentorship and invaluable intellectual resources made available by Dr. Ross Carlson of the Center for Biofilm Engineering at Montana State University, Bozeman, MT. I am thankful for the collaboration with Dr. Musahid Ahmed of the Chemical Sciences Division, Lawrence Berkeley National Laboratory, whose resources lead to many great investigations of my work and fulfilled a dream of mine to work with their great national laboratory. A debt of gratitude is owed to the many contributing co-authors that have been critical, patient, and supportive of my work. To Dr. J.F. Moore for endless hours discussing engineering and science and being my greatest advocate through these years. To the members of the Hanley Group (past and present), thank you for the many lessons exchanged in and outside of the laboratory. Most importantly, to my advisor Dr. Luke Hanley who took a chance on a curious undergraduate, and subsequently inherited a stubborn and untamed graduate student. Thank you for your infinite guidance and patience that provided me the room needed to grow. Because of you, I am now a driven and humble scientist.

GLG

TABLE OF CONTENTS

<u>CHAPTER</u>	<u>PAGE</u>
ACKNOWLEDGEMENTS	IV
TABLE OF CONTENTS	V
LIST OF TABLES	IX
LIST OF FIGURES	X
LIST OF ABBREVIATIONS	XII
SUMMARY	XIII
1 INTRODUCTION.....	1
1.1 Biofilms	1
1.1.1 Biofilm Infection.....	1
1.1.2 Biofilm Growth Cycle.....	2
1.1.3 Biofilm Extracellular Polymeric Substance.....	3
1.1.4 Biofilm Communication and Quorum Sensing.....	3
1.1.5 Biofilm Antimicrobial Resistance.....	4
1.1.6 Biofilm Growth Types.....	4
1.2 Laser Desorption Postionization Mass Spectrometry	6
1.2.1 General Description of Technique.....	6
1.2.2 Single Photon Ionization.....	8
1.3 MS Imaging	12
1.4 MS Methods to Image Biofilms	15
1.4.1 Vacuum MS Methods	15
1.4.1.1 Matrix Assisted Laser Desorption Ionization	15
1.4.1.2 Secondary Ionization Mass Spectrometry.	16
1.4.1.3 Laser Desorption Postionization Mass Spectrometry.....	17
1.4.2 Atmospheric Pressure MS Methods.....	17
1.5 Depth Profiling.....	18
1.6 Matrix Enhancement.....	19

TABLE OF CONTENTS (CONT.)

CHAPTER	PAGE
2 EXPERIMENTAL	21
2.1 Instrumentation	21
2.1.1 First Generation LDPI-MS	21
2.1.2 Second Generation LDPI-MS	23
2.1.2.1 MS Imaging and Data Collection	26
2.1.2.2 Instrument Control Experiments.....	27
2.1.3 LDPI-MS at the Advanced Light Source.....	27
2.1.4 Scanning Electron Microscopy.....	29
2.1.5 Analyte and Signal Decay Experiment.....	30
2.1.6 Mass Calibration	30
2.2 Sample Preparation.	31
2.2.1 Neat Sample Preparation.....	31
2.2.2 Growth of Membrane Colony Biofilm and Treatment.	31
2.2.3 Drip Flow Biofilms on ITO Slides and Silicon Wafers.....	32
2.2.4 Cross Sectioning of Membrane Biofilms.....	34
2.2.5 Biofilm Viability Studies.....	35
2.2.6 Matrix Application.....	36
2.3 LDPI-MS Mechanical Instrumental Upgrades.	36
3 VACUUM ULTRAVIOLET, 7.87 EV, POSTIONIZATION OF LASER DESORBED NEUTRALS TO DETECT ANTIBIOTICS IN <i>STAPHYLOCOCCUS EPIDERMIDIS</i> BACTERIAL BIOFILMS:	41
3.1 INTRODUCTION	42
3.2 EXPERIMENTAL	42
3.3 RESULTS AND DISCUSSION	42
3.3.1 Detection of Neat Antibiotics	42
3.3.2 Detection of Antibiotics in Bacterial Biofilms	45
3.3.3 Bacterial Biofilm Viability Study	46
3.4 CONCLUSION	49

TABLE OF CONTENTS (CONT.)

CHAPTER	PAGE
4 TUNABLE POSTIONIZATION OF LASER DESORBED NEUTRALS BY SYNCHROTRON RADIATION TO DETECT ANTIBIOTICS AND EXTRACELLULAR MATERIAL IN <i>STAPHYLOCOCCUS EPIDERMIDIS</i> BACTERIAL BIOFILMS.....	50
4.1 INTRODUCTION.....	51
4.2 EXPERIMENTAL.....	52
4.3 RESULTS AND DISCUSSION	53
4.3.1 Photoionization of Thermal Desorbed Neat Antibiotics.....	53
4.3.2 Detection of Neat Antibiotics.....	54
4.3.3 Analysis of Biofilms Treated with Rifampicin Antibiotic.....	57
4.3.4 LDPI-MS Comparison of Biofilms with and without Antibiotic Treatment.....	61
4.3.5 Laser Desorption Effects.....	65
4.4 CONCLUSIONS	67
5 COMPARING VACUUM AND EXTREME ULTRAVIOLET RADIATION FOR POSTIONIZATION OF LASER DESORBED NEUTRALS FROM BACTERIAL BIOFILMS AND ORGANIC FULLERENES.....	70
5.1 INTRODUCTION.....	71
5.2 EXPERIMENTAL.....	71
5.3 RESULTS AND DISCUSSION	72
5.3.1 EUV LDPI-MS of Neat Organic Samples.....	72
5.3.2 EUV LDPI-MS of Doped Bacterial Biofilms.....	74
5.4 CONCLUSION	76
6 MS IMAGING OF ANTIBIOTICS DISTRIBUTION AND UPTAKE WITHIN BACTERIAL BIOFILMS BY 7.87 EV LASER DESORPTION POSTIONIZATION	77
6.1 INTRODUCTION.....	78
6.2 EXPERIMENTAL.....	78

TABLE OF CONTENTS (CONT.)

<u>CHAPTER</u>	<u>PAGE</u>
6.3 RESULTS AND DISCUSSION	79
6.3.1 Determination of Parent Ions as Radical Cations.	79
6.3.2 Detection of Neat Antibiotics by LDPI-MS.	80
6.3.3 Assignment of Parent and Fragment Ions.	81
6.3.4 Detection of Antibiotics in Bacterial Biofilm by 7.87 eV LDPI-MS.	85
6.3.5 Differences in Antibiotic Fragmentation Present in Biofilm	86
6.3.6 MS Imaging Antibiotics without Matrix.....	87
6.3.7 MS Imaging Antibiotics with Matrix.....	93
6.3.8 Depth Profiling of Biofilm Cross Sections.	99
6.3.9 Imaging Resolution, Speed, and Other Parameters.	100
6.4 CONCLUSION	103
 CITED LITERATURE	 107
APPENDIX A. ANTIBIOTIC CHEMICAL STRUCTURES AND FRAGMENTATION	118
CIRRICULUM VITA.....	123

LIST OF TABLES

<u>TABLE</u>	<u>PAGE</u>
Table 1: Values of rifampicin parent to fragment ion ratios (M/F) for LDPI-MS of rifampicin doped biofilm at 10.5 and 20 eV.....	76
Table 2: Antibiotic fragmentation during 7.87 eV LDPI-MS.....	83

LIST OF FIGURES

FIGURE	PAGE
Figure 1: Cartoon depicting biofilm growth by membrane and drip flow methods.	4
Figure 2. Cartoon of flow cell for drip flow biofilm growth.	5
Figure 3: SEM image of <i>S. epidermidis</i> grown by membrane and drip flow.	6
Figure 4. Generic mass spectrum.	7
Figure 5: General schematic of LDPI-MS (top view).	8
Figure 6: Cartoon depicting single and multiple ionization mechanisms.	11
Figure 7. Schematic of MS imaging experiment.	13
Figure 8. General scheme for 3D MS imaging by z-stacking or tissue sectioning.	14
Figure 9: First generation LDPI-MS with linear extraction.	23
Figure 10: Second generation LDPI-MS.	24
Figure 11: Computer aided drawing of second generation LDPI-MS instrument.	25
Figure 12: Schematic of TOF-SIMS instrument at the Advanced Light Sources.	28
Figure 13: Cartoon depicting preparation of colony biofilm.	32
Figure 14: Picture of membrane biofilm.	33
Figure 15. Image and schematic of drip flow cell for biofilm growth.	34
Figure 16. <i>S. epidermidis</i> cell viability using tetracycline gradient test strips.	35
Figure 17: Four segments of LDPI-MS instrument (top view).	38
Figure 18: CAD rendering and cross section of second generation LDPI-MS ion optics.	40
Figure 19: 7.87 eV LDPI-MS of neat antibiotics.	43
Figure 20: 7.87 eV LDPI-MS of antibiotic doped bacterial biofilms.	46
Figure 21: Viability study of <i>S. epidermidis</i> with tetracycline.	47
Figure 22: 7.87 eV LDPI-MS of 8 μ M tetracycline in colony biofilm.	48
Figure 23: PIE of thermally desorbed neat antibiotics.	53
Figure 24: LDPI-MS of neat rifampicin at photon energies 8 – 12.5 eV.	55
Figure 25: LDPI-MS of neat trimethoprim at photon energies 8 – 12.5 eV.	57
Figure 26: LDPI-MS of rifampicin doped biofilm at photon energies 8 – 12.5 eV.	59
Figure 27: Peptidoglycan layer in the outer membrane of Gram-positive bacteria.	60
Figure 28: LDPI-MS of trimethoprim doped biofilm at photon energies 8 and 10.5 eV.	62
Figure 29: Comparison of biofilm control and antibiotic doped biofilm.	63

LIST OF FIGURES (CONT.)

<u>FIGURE</u>	<u>PAGE</u>
Figure 30: LDPI-MS of neat biofilm at photon energies 8 – 12.5 eV.	64
Figure 31: Decay curve of rifampicin LDPI-MS signal intensity.....	66
Figure 32: EUV LDPI-MS of fullerene.	73
Figure 33: Parent to fragment signal profile by EUV LDPI-MS of neat fullerene.....	73
Figure 34: 7.87 eV LDPI-MS (UIC) of neat C ₆₂	74
Figure 35: EUV LDPI-MS of rifampicin doped biofilm grown on ITO slide.....	75
Figure 36: Showing radical cationization using 7.87 eV LDPI-MS.....	80
Figure 37: 7.87 eV LDPI-MS of ten neat antibiotics.....	84
Figure 38: 7.87 eV LDPI-MS of antibiotic doped membrane biofilm.	85
Figure 39: MS image of rifampicin distribution in sector of membrane biofilm.	88
Figure 40: LDPI-MS image of rifampicin concentration gradient in biofilm.	90
Figure 41: Integration of rifampicin signal intensity along gradient axis.....	91
Figure 42: LDPI-MS image, SEM, and optical image of drop flow biofilm.....	92
Figure 43: LDPI-MS spectra of ciprofloxacin fragments.	94
Figure 44: Cartoon of matrix experiment.	95
Figure 45: LDPI-MS spectra of regions of interest for matrix and non-matrix areas.....	96
Figure 46: LDPI-MS images of ciprofloxacin doped biofilm with CHCA matrix.....	98
Figure 47: LDPI-MS image of trimethoprim doped biofilm cross section.....	100
Figure 48: LPDI-MS signal decay of rifampicin doped membrane biofilm.....	102

LIST OF ABBREVIATIONS

CAD	computer aided drafting
CHCA	α -cyano-4-hydroxycinnamic acid
CFU	colony forming unit (per mL)
CNC	computer numerical control
DIOS	desorption/ionization on silicon
EPS	extracellular polymeric substance
EUV	extreme ultraviolet
eV	electron volt
IMFP	inelastic mean free path
IMS	imaging mass spectrometry
IE	ionization energy
IP	ionization potential
LC-MS	liquid chromatography-mass spectrometry
LD	laser desorption
LDPI	laser desorption postionization
MALDI	matrix-assisted laser desorption/ionization
MCP	dual microchannel plate
MPI	multiphoton ionization
MS	mass spectrometry
PIE	photoionization efficiency
QS	quorum sensing
R2PI	two-photon ionization
SEM	scanning electron microscopy
SIMS	secondary ionization mass spectrometry
SNMS	secondary neutral mass spectrometry
SPI	single photon ionization
ToF	time of flight
VUV	vacuum ultraviolet
YLF	yttrium lithium fluoride
XPS	x-ray photoelectron spectroscopy

SUMMARY

A biofilm is a microbial network adhered to a surface while acting collectively to perform functions to sustain viability. Bacterial biofilms can be robust and capable of surviving harsh environments such as extreme pH and temperature. They are commonly found as human microflora on the skin and as oral plaques. Among many of their unique qualities, biofilms are able to thwart antimicrobial strategies. Biofilms are characterized by qualities that distinguish them from their solution-dwelling counterparts. They include features such as adherence, growth and proliferation on a variety of surfaces. Biofilms act in a consortium via a cooperative signaling mechanism referred to as quorum sensing. Biofilms secrete an extracellular polymeric substance (EPS) into the extracellular region to perform adhesion to a surface, cohesion between cells, digestion, recycling, and the formation of fluid channels throughout. The biofilm's ability to effectively persist during antimicrobial treatments creates a need for better understanding these complex biological systems.

Studies have attempted to further understand the biofilm mechanisms that make them well adapted to survive antimicrobial treatments. Research has covered a number of areas to improve the general knowledge of how biofilms perform various processes, such as: production of EPS material, quorum sensing, inhibition of antimicrobials, and surface interaction. For example, studying chemical properties of EPS can lead to new strategies to create agents to alter, and effectively reduce, biofilm adhesive properties. Understanding biofilm phenotypic expression for EPS production could lend to reducing or disabling adhesion altogether. In order to investigate these and other aspects of biofilms, new analysis methods need to be developed. For chemical information pertaining to the biofilm and its surrounding environment, an analytical method of great potential is mass spectrometry.

Mass spectrometry (MS) provides chemical identification and structural elucidation. MS techniques are important to extract this chemical information to qualitatively monitor not only the presence of a chemical species, but also changes that may have occurred as a result of interaction with the surface or the surrounding environment. Quantitative capabilities can provide additional information to describe exactly how much of a substance is present. These analytical methods allow for monitoring of multiple chemical species simultaneously, allowing the ability to correlate one chemical species with another.

MS imaging provides additional information that correlates chemical information with spatial distribution. This technique can be performed by rastering the analytical microprobe across the sample area of interest while collecting MS data and addressing this information with spatial coordinates. From a global spectrum representing all chemical species present in the sample, a spatial map or distribution of signal intensity from a user-defined mass, or mass range, is produced representing the investigated sample area.

Laser desorption postionization mass spectrometry (LDPI-MS) is a powerful analytical technique capable of imaging small molecules. LDPI-MS is a laser-based method which ionizes gaseous neutral molecules introduced by laser desorption of a solid phase analyte into vacuum. This method decouples desorption and ionization events to provide improved control and characterization of the analyte. As a soft ionization method, LDPI-MS imposes less excess energy to the analyzed system that would otherwise lead to increased spectral complexity and hinder chemical identification. In addition to its aforementioned abilities, LDPI-MS is selective, sensitive, and able to investigate complex chemical models.

Experimental investigations of bacterial biofilms with LDPI-MS will cover four chapters in this thesis. Chapter 3 describes the development of 7.87 eV LDPI-MS to detect antibiotics

within intact bacterial colony biofilms. Antibiotics with structures indicative of sub-7.87 eV ionization energy were examined for their ability to be detected by 7.87 eV LDPI-MS. Tetracycline, sulfadiazine, and novobiocin were successfully detected neat as dried films physisorbed on porous silicon oxide substrates. Tetracycline and sulfadiazine were then detected within intact *S. epidermidis* colony biofilms, the former with a LOD in the micromolar concentration range.

Chapter 4 investigates LDPI-MS at photon energies above 7.87 eV. At photon energies from 8.0 – 12.5 eV, tunable vacuum ultraviolet synchrotron radiation was used to ionize antibiotics and extracellular neutrals that were laser desorbed both neat and from intact bacterial biofilms. Different extracellular material was observed by LDPI-MS in response to rifampicin or trimethoprim antibiotic treatment. Data will demonstrate that 10.5 eV LDPI-MS displays the optimum trade-off between improved sensitivity and minimum fragmentation.

Chapter 5 continues the previous chapter and extends into the extreme ultraviolet region with radiation from 8 - 24 eV. These investigations used the synchrotron to postionize laser desorbed neutrals of antibiotic-treated biofilms and a modified fullerene using LDPI-MS. Results showed detection of the parent ion, various fragments, and extracellular material from biofilms using LDPI-MS with both vacuum and extreme ultraviolet photons. Parent ions were observed for both cases, but extreme ultraviolet photons (16 - 24 eV) induced more fragmentation than vacuum ultraviolet (8 - 14 eV) photons.

Chapter 6 shows how LDPI-MS was used to image the distribution of antibiotics within intact bacterial biofilms. LDPI-MS using 7.87 eV energy photons detected a wide range of antibiotics both neat and within intact *S. epidermidis* biofilms grown both on membranes and by drip flow. Most of the antibiotics detected possess secondary and tertiary aromatic amines which are expected to display ionization energies below 7.87 eV photon energies. Cross sectioning was used to depth

profile antibiotics within biofilm slices with depth resolution of $\sim 30 \mu\text{m}$. LDPI-MS produced images with a resolution $\sim 30 \mu\text{m}$ by continuous motion scanning of the sample. Limits of detection were ~ 20 fmol for detection of ciprofloxacin when CHCA matrix was added.

1 INTRODUCTION

1.1 Biofilms

A biofilm is a cellular network adhered to a surface. Bacterial biofilms are found in many aspects of life, including industry, nature, and the human domain. In industry, biofilms participate in biofouling pipelines, material corrosion, and introduce problems in water remediation. Biofouling has profound effects such as material degradation, reducing effectiveness of material heat transfer, and mechanical blockage of fluid piping (Coetser and Cloete, 2005). Electrochemical processes can be initiated by microbes on metallic surfaces to begin corrosion (Flemming and Cloete, 2010). Biofilms are found naturally on the bedrock of streams in the form of algae, within and near hot springs, and in soil. In the human domain, bacterial biofilms dwell in the oral cavity as oral plaques as well as on skin as part of protective microflora against other more aggressive pathogens (Stewart et al., 2004).

Biofilms possess unique qualities that distinguish them from their planktonic, solution dwelling counterparts. Biofilms colonize to form a dense cellular network that is characterized as adhering to a surface. Biofilms have the ability to adhere to surfaces of various compositions and effectively colonize on plastics, metals, and ceramics. Their ability to communicate with each other and maintain a strong cellular network allows them to sustain viability (Kudo et al., 1987). Their ability to sustain infections makes them a more important area of research.

1.1.1 Biofilm Infection.

Bacterial biofilms are a major cause of infection in hospitals and surgical implants (Stewart et al., 2004). For example, *Staphylococcus epidermidis* is a gram positive microbe capable of forming a bacterial biofilm and responsible for many hospital catheter infections

(Götz, 2002). Biofilms can cause persistent and antibiotic-resistant infections (Stewart et al., 2001), the treatment of which is of major concern in hospital and outpatient settings. Physicians observe up to 65% of bacterial infections are due to biofilms (Thomas et al., 2004) and 70% of hospital infections are the result of *S. epidermidis* with significant impact in the following surgical areas: implant infections (20 - 50%), prosthetic cardiac valve (40 - 50%), catheter infections (50 - 70%), central nervous shunts (48 - 67%), neurosurgical procedures (>50%) (O’Gara, 2001).

1.1.2 Biofilm Growth Cycle.

The biofilm growth cycle includes three general stages. All biofilms must initiate attachment to a given surface. With the assistance of an adhesive material, known as extracellular material (discussed further in next section), cells will anchor to the surface and each other to resist detachment into the surrounding solution or environment. After adherence to the surface, the biofilm will begin the next stage of growth, called colonization. During this period, the biofilm will spread across a surface laterally while excreting the adhesive material. Once the biofilm is established on a surface, nutrient channels will naturally form from the heterogeneous growth in three-dimensional space. These liquid channels will provide pathways for nutrient and waste transport as well as chemical messaging. The final stage includes the release of both dead and viable biofilm cells. In the case of an antimicrobial attack, dead cells will protect the biofilm bulk by chemical quenching, or chemically deactivating, and eventually be signaled to detach in order to expose deeper layers to an available nutrient supply. In order to spread the biofilm to more distant places, viable cells will detach and migrate to start the entire process again (Otto, 2009).

Maintaining this dense cellular network is the foundation of the biofilm's strength. The next section will discuss the adhesive material and two major activities as a consequence of this cellular network. Methods to grow model biofilms in the laboratory will be discussed as well.

1.1.3 Biofilm Extracellular Polymeric Substance.

The biofilm is encased in an extracellular polymeric substance (EPS) that allows adhesion to various material surfaces and cohesion to each other. This material includes polysaccharides, and nucleic acids (Flemming and Wingender, 2010). EPS comprises nearly 90% of the biofilm biomass and contributes significantly to the structural qualities that characterize biofilms. This extracellular matrix provides the three-dimensional structure of the biofilm, is described as “cathedral” and resembles mushroom-like formations (Stewart and Franklin, 2008). The fluid channels present throughout the biofilm allow for nutrient and waste transfer. In addition, digestion can occur outside the cell in order to recycle raw cellular material.

1.1.4 Biofilm Communication and Quorum Sensing.

Biofilms employ a form of chemical communication called quorum sensing (QS). This characteristic allows this network of cells to work collectively and coordinate various tasks such as cell growth, adhesion, and death. In addition, quorum sensing may act in response to external factors with the release of virulence factors to protect against foreign invaders, including antimicrobials.

1.1.5 Biofilm Antimicrobial Resistance.

A number of current hypotheses for explaining biofilm antibiotic tolerance include an alleged ability to inhibit the diffusion of antibiotics (Stewart, 2003; Musk and Hergenrother, 2006; Lopez et al., 2010), physiological heterogeneity due to chemical and nutrient gradients in biofilms (Stewart and Franklin, 2008), the coordinated regulation of genes via the exchange of chemical signal molecules including the process of quorum sensing (Straight and Kolter, 2009), and the generation of metabolically dormant persister cells (Lewis, 2010; Otto, 2009).

1.1.6 Biofilm Growth Types.

Biofilms can be grown by two popular methods. One method is on a polycarbonate membrane mounted on solid nutrient agar (Xu et al., 1998). In this technique, a small area in the center of a porous membrane is inoculated. The effective size of a single bacterial cell is larger than the membrane pore size, keeping the bacterial colony at the surface of the membrane. In the case of *S. epidermidis*, cells are $\sim 1 \mu\text{m}$ and membrane pore size is near $0.2 \mu\text{m}$. Membrane biofilms are sessile and fixed to the surface under conditions without fluid flow making them weakly attached and easily removed from the surface. Nevertheless, this method produces relatively thick ($\sim 300 \mu\text{m}$) biofilms.

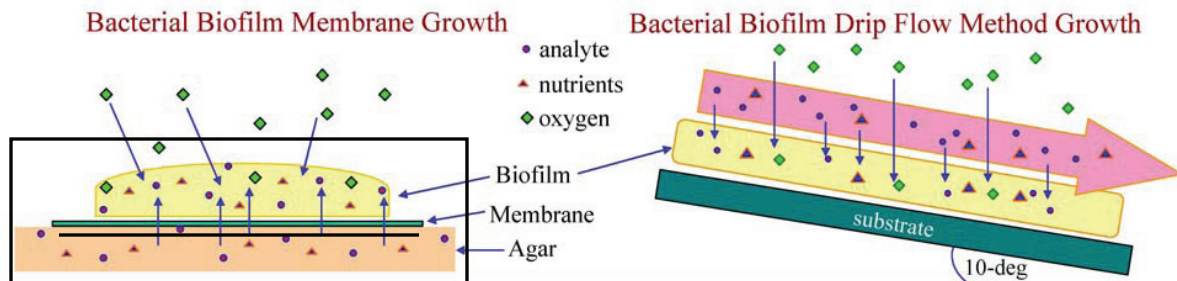


Figure 1: Cartoon depicting biofilm growth by membrane and drip flow methods.

Nutrients are either solid (TSA, tryptic soy agar) or fluid (TSB, tryptic soy broth) under flow. Biofilm growth platforms are defined by polycarbonate membrane and rigid substrates.

Figure 1 (right), depicts biofilms grown by drip flow where fluid shear is introduced by drop-wise (pump-feed) administration of nutrient supply. The effective fluid force induces a phenotypic response resulting in the production of EPS material. The additional EPS material creates a more robust biofilm that is stronger and more mechanically resistant to removal from the surface. Figure 2 is a more general schematic of a flow cell for preparing drip flow biofilms. It is typically comprised of an inlet and outlet for nutrient flow, and a general chamber where the substrate is located and mounted for biofilm growth to occur. Figure 3 shows scanning electron microscope (SEM) images of membrane and drip flow biofilms where the difference in EPS material in these two growth methods is more apparent. Growth by drip flow does produce thinner biofilms (~100 - 150 μm) compared to membrane.

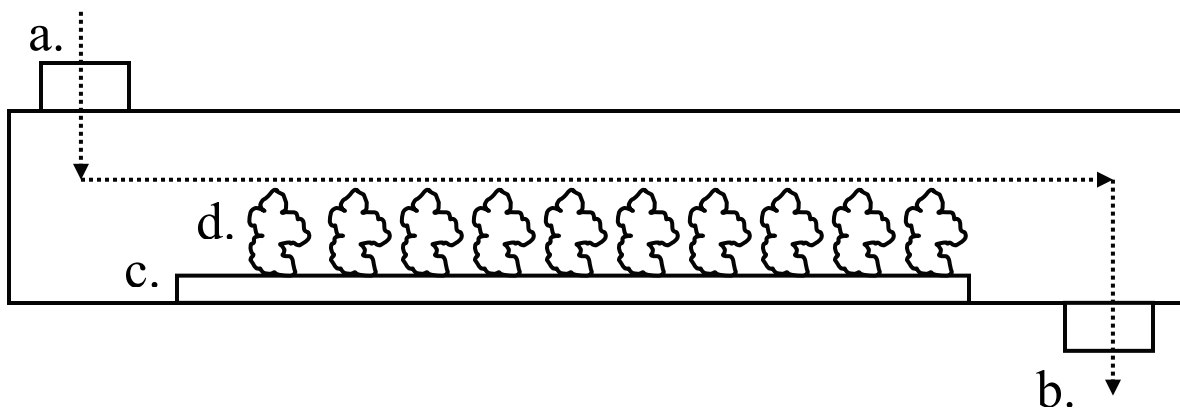


Figure 2. Cartoon of flow cell for drip flow biofilm growth.

Within the flow cell, the following labels indicate: (a) liquid nutrient inlet, (b) liquid nutrient outlet, (c) substrate, and (d) biofilm. Dotted arrows indicate direction of liquid flow.

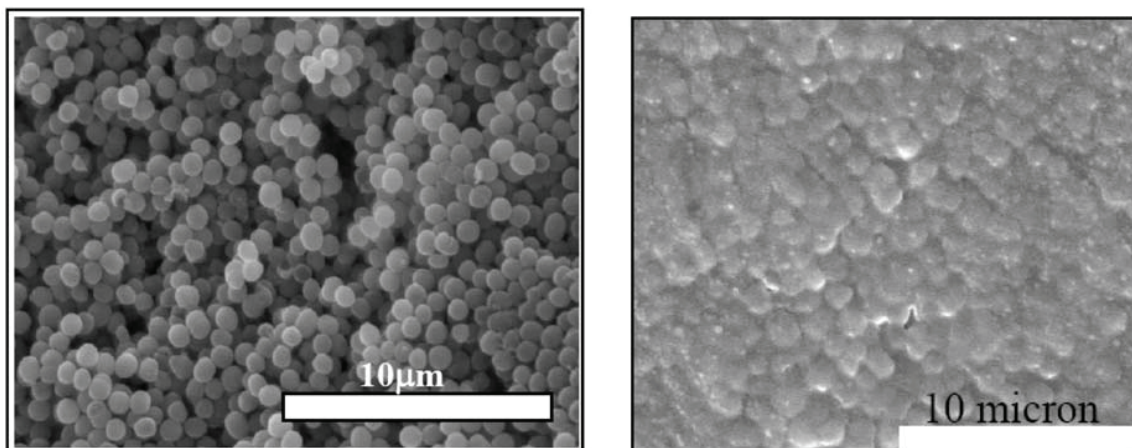


Figure 3: SEM image of *S. epidermidis* grown by membrane and drip flow.
Panels: (left) biofilm grown on polycarbonate membrane, (right) biofilm grown by drip flow. Scale bar = 10 μm

1.2 Laser Desorption Postionization Mass Spectrometry

1.2.1 General Description of Technique.

LDPI is an *in vacuo* mass spectrometric technique using two lasers. An ultraviolet (UV) laser initiates desorption of neutral molecules from a solid surface via phase explosion thereby ejecting neutrals into a vaporous phase (Akhmetov et al., 2010). The second laser serves to ionize the neutral plume by causing an electron ejection due to photon ionization. With the formation of a stable radical cation (odd-electron), ion optics accelerate these charged particles and further focus them to remove energetic distributions in the ion packet. Using a time of flight (ToF) analyzer, ions of various masses are separated by timing their individual arrival to a detector after traveling through a fixed distance. A spectrum is created showing mass to charge (m/z , where charge is one) verses ion abundance (the number of ions that arrive at a given time), which allows chemical identification along with structural elucidation.

Figure 4 provides a generic mass spectrum of ampicillin (MW: 349). Fragments represent loss of various functional groups that have dissociated from the parent molecule. For example,

terminal group A dissociated to display a peak near 17 μsec . The difference between the peak at 17 and 15 μsec resulted from loss of a hydroxyl group.

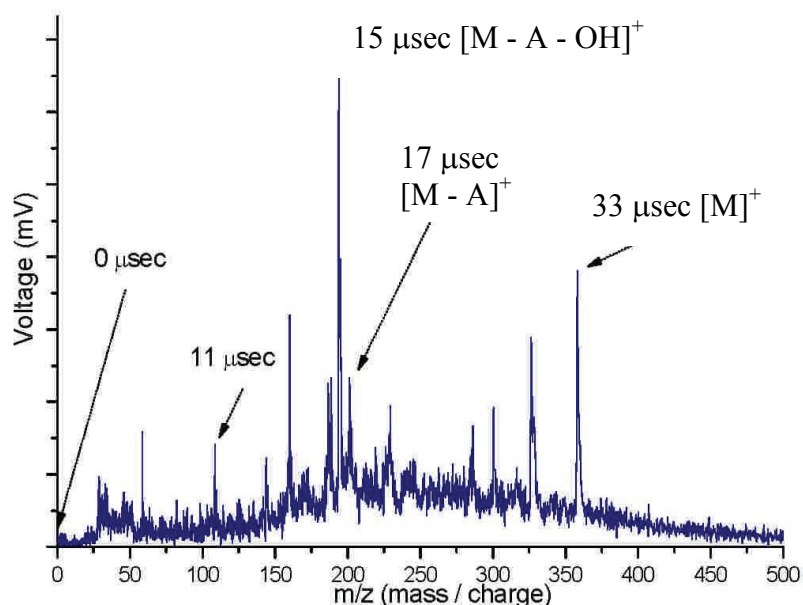


Figure 4. Generic mass spectrum.

Mass spectrum showing mass to charge ratio (m/z) and voltage (ion abundance). Peaks indicate the parent ion (M^+) and the various fragments indicating loss of various chemical terminal groups.

The LDPI-MS instrument is composed of four segments shown in Figure 5, including: load lock, main chamber, ToF, and laser table. The load lock provides introduction of sample to vacuum and transfer into the main chamber. The laser table contains lasers and optics for beam refinement. The ToF tube contains the drift space for ion separation along with detectors for ion collection. In addition, an ion mirror in the ToF reduces energetic distributions of the ion packets to provide improved resolution (note the ions from the ion mirror do not take a curved trajectory back through the ToF). The main chamber performs processes that introduce the sample into vacuum and ionize vapor phase molecules for mass spectrometric analysis. More detail is provided in Chapter 2, Section: LDPI-MS Mechanical Instrument Upgrades.

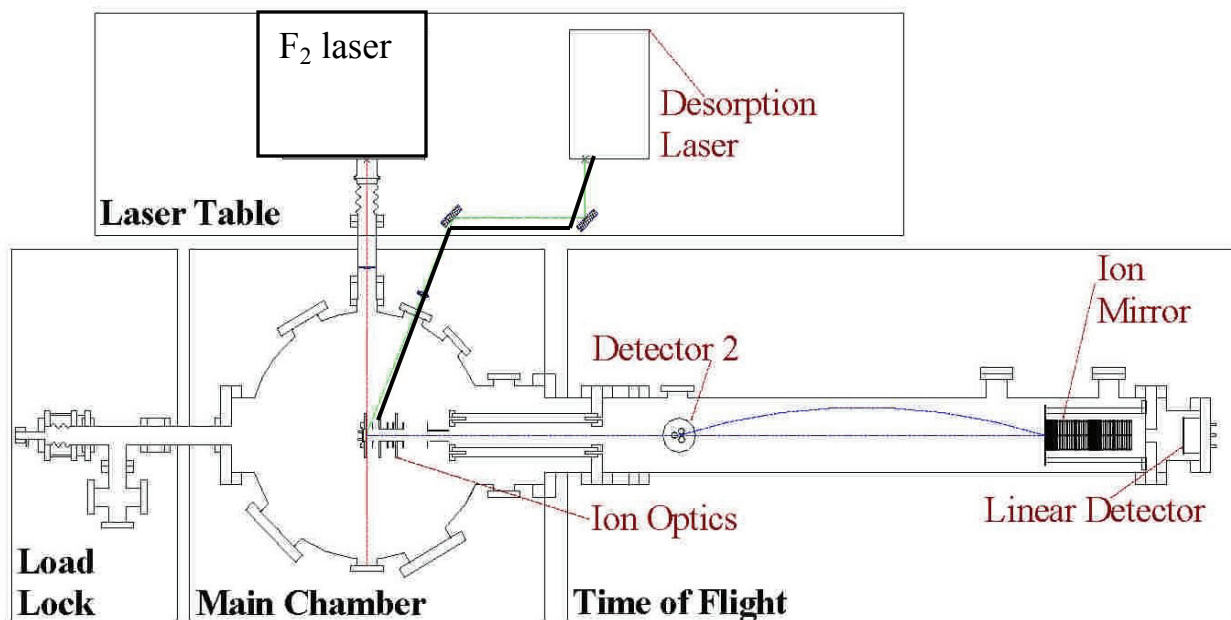


Figure 5: General schematic of LDPI-MS (top view).

Top view of LDPI-MS instrument which contains four segments: load lock, main chamber, ToF tube, and laser table.

1.2.2 Single Photon Ionization.

LDPI-MS employs single photon ionization (SPI) with VUV radiation to effectively ionize gaseous neutrals. SPI is typically performed near the ionization threshold, where irradiating VUV photon energies are within a few eV of analyte ionization energies, minimizing excess energy within the parent ion that can otherwise lead to dissociation (Hanley and Zimmerman, 2009).

In the case the analyte ionization energy is slightly above that of the source, derivatization can be performed. By chemically “tagging” the analyte, the overall ionization threshold can be lowered to allow removal of an electron. Prior work demonstrated that tagging with 6-aminoquinolyl-N-hydroxysuccinimidyl carbamate allowed detection of a known quorum sensing

peptide within intact *Bacillus subtilis* biofilms by 7.87 eV VUV LDPI-MS (Edirisinghe et al., 2007).

SPI is used in LDPI-MS to postionize the abundant gas-phase neutral molecules ejected by laser desorption. During a SPI process, a single photon is absorbed to form an ion by virtue of the system containing the energy necessary to eject a photoelectron. Most carbon-containing species will undergo SPI with 10.5 eV photons. Utilizing an ionization source below 10.5 eV will reduce the number of chemical classes that are observable. This renders LDPI-MS with lower photon energies chemically selective for low ionization energy species, simplifying mass spectra and minimizing background signal. SPI mechanisms were discussed in greater detail along with other fundamental aspects of VUV SPI and LDPI-MS in the literature (Akhmetov et al., 2010).

This approach can also minimize analyte fragmentation if a stable radical cation can be formed (Hanley and Zimmerman, 2009). The excess energy above the ionization energy will typically be distributed among the vibrational modes of the ion that will lead to dissociation of bonds to form neutral-ion fragments.

As >99% of the molecules ejected by laser desorption are neutrals, VUV photoionization of these neutrals can provide significantly increased signal compared to detection of directly emitted ions at low power densities. Postionization of laser desorbed neutrals with 7.87 eV photons from a molecular fluorine laser will single photon ionize various low ionization energy compounds including secondary, tertiary, and aromatic amines as well as various fused ring aromatics, tryptophan containing peptides, and pharmaceuticals (Finch et al., 2005; Hanley et al., 2006; Edirisinghe et al., 2006).

The concept of sensitivity in mass spectrometry describes the efficiency with which ions are created and detected by a given technique. However, sensitivity can be more clearly defined via equations for ion yield. Ion yield of gaseous neutrals by SPI is described by the following equation:

$$Y(\text{spi})^+ = \sigma I N \quad (1.1).$$

where ion yield (Y^+) is defined by cross section (σ), laser intensity (I), and density of gaseous neutrals (N). Laser intensity can also describe the density of photons or power per area ($J/s/cm^2$). Whereas, flux describes the number of photon per time (photon/s). The cross section describes the probability that a given chemical class will absorb a photon at a given energy to eject an electron (Akhmetov et al., 2010). Whereas, resonant two-photon ionization (R2PI) has the following equation:

$$Y(\text{mpi})^+ = \sigma_1 \sigma_2 I_1 I_2 N \quad (1.2).$$

Additional terms for cross section describe each absorbed photon in the process. Cross sections for SPI are greater than the product of cross sections for R2PI ($\sigma > \sigma_1 \sigma_2$). This means that R2PI requires greater laser intensity compared with SPI to give similar ion yield.

Figure 6 displays a general cartoon depicting the difference between SPI and R2PI. In the case of R2PI, photon energy can be matched to that of an intermediate electronic state and produce selective ionization channels (Boesl, 1991). Specifically, cross sections σ_1 and σ_2 for MPI are highly species dependent. In the case photons of equivalent, or resonant, energies are

absorbed, the cross section increases significantly to produce high ion yields. However, the process is so chemically specific, R2PI can be considered too selective and not ideal for more general studies. However, in the case where multiple photons are absorbed, the excess energy present in the ion can be greater, thereby leading to greater fragmentation of the parent ion.

In the case of SPI, the photon energy must be greater than the ionization energy of the chemical species ($h\nu > IE$). However, in the case of R2PI with one UV laser, two photons must overcome the IE ($2h\nu > IE$) and must have resonant intermediate states (M^*). In the case of R2PI with two UV lasers, the sum of two photons must overcome the IE ($h\nu_1 + h\nu_2 > IE$). These stricter criteria for R2PI along with requirements for strong absorption in the UV/visible often results in induced dissociation of the molecule. There also exist other forms of MPI that are more selective but even less efficient than R2PI.

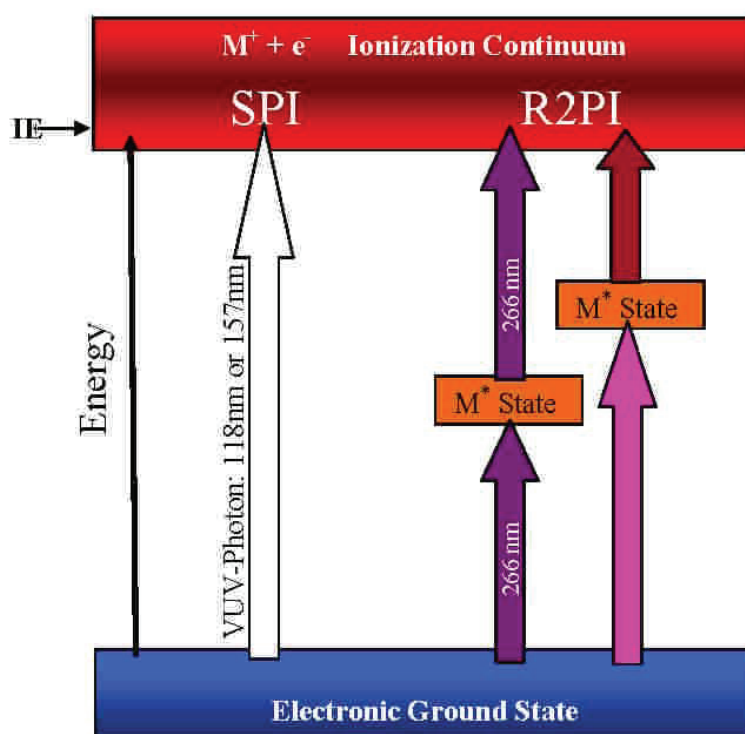


Figure 6: Cartoon depicting single and multiple ionization mechanisms. The cartoon shows electronic states, including (M) ground, (M^*) intermediate, and (M^+) ionization continuum as a result of (SPI) single photon ionization, and (R2PI) resonant two-photon ionization.

1.3 MS Imaging

MS imaging allows correlation of chemical information with biologically relevant structures while maintaining spatial and chemical integrity (Seeley and Caprioli, 2008; Malm et al., 2009; Chughtai and Heeren, 2010; Kurczy et al., 2010; Kroiss et al., 2010; Watrous et al., 2011). Figure 7 provides a general scheme for an MS imaging experiment. In the case of laser based techniques, an imaging experiment will fire a pulsed laser at one location consecutively until sufficient ion signal is collected to produce an averaged spectrum. The sample stage or laser position will move to a new location on the sample and iterate the process until a user-defined area has been surveyed. In order to chemically map this area, a global spectrum is produced from which a user-defined peak is chosen. This peak may be comprised of a mass at a single data point or a mass range. The intensity of this peak is mapped across a contour plot that represents two-dimensional space and peak intensity in the z-axis (typically depicted by a false color scale). Further, multiple peaks or masses can be shown in the same plot to correlate chemical information within the biological structure.

Three dimensional (3D) MS images are similar to stacking 2D MS plots to produce chemical information relating to 3D space. Figure 8 provides a general sequence of how 3D MS imaging may be performed. In one experiment, a bulk sample may be scanned across an area to compile data to produce the contour plot seen in Figure 8a. Figure 8b shows this process can be iterated across the same sample area to produce multiple 2D plots that differ along the z-axis of the sample. The information acquired from Figure 8b can be transformed to produce Figure 8c, a 3D plot, depicting the distribution of different chemical species in 3D space (Svatoš, 2010). In a second experiment, 3D images can be produced by compiling 2D scans of consecutive cross sections (Figure 8b to 8c).

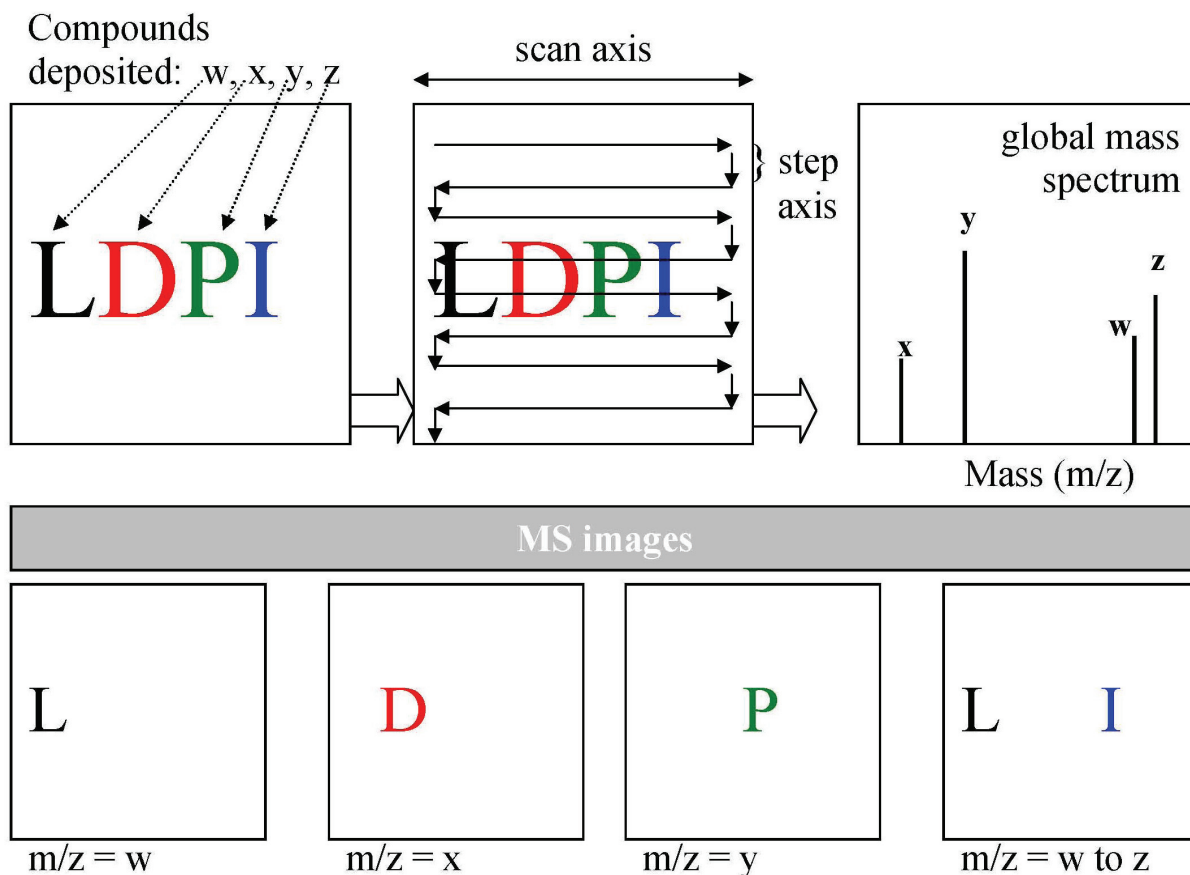


Figure 7. Schematic of MS imaging experiment.

Four chemical compounds (w, x, y, z) were deposited on a sample plate as the respective alphabetic letters (L, D, P, I). The sample area is rastered to collect data from within the area. A global spectrum shows all four chemical constituents present in the imaging sample area. MS images were produced by choosing select mass to charge (m/z) ratios of respective compounds to produce a plot correlating the location of the compound in space. In the final case (far right), the m/z range from “w to z” was selected to display L and I only.

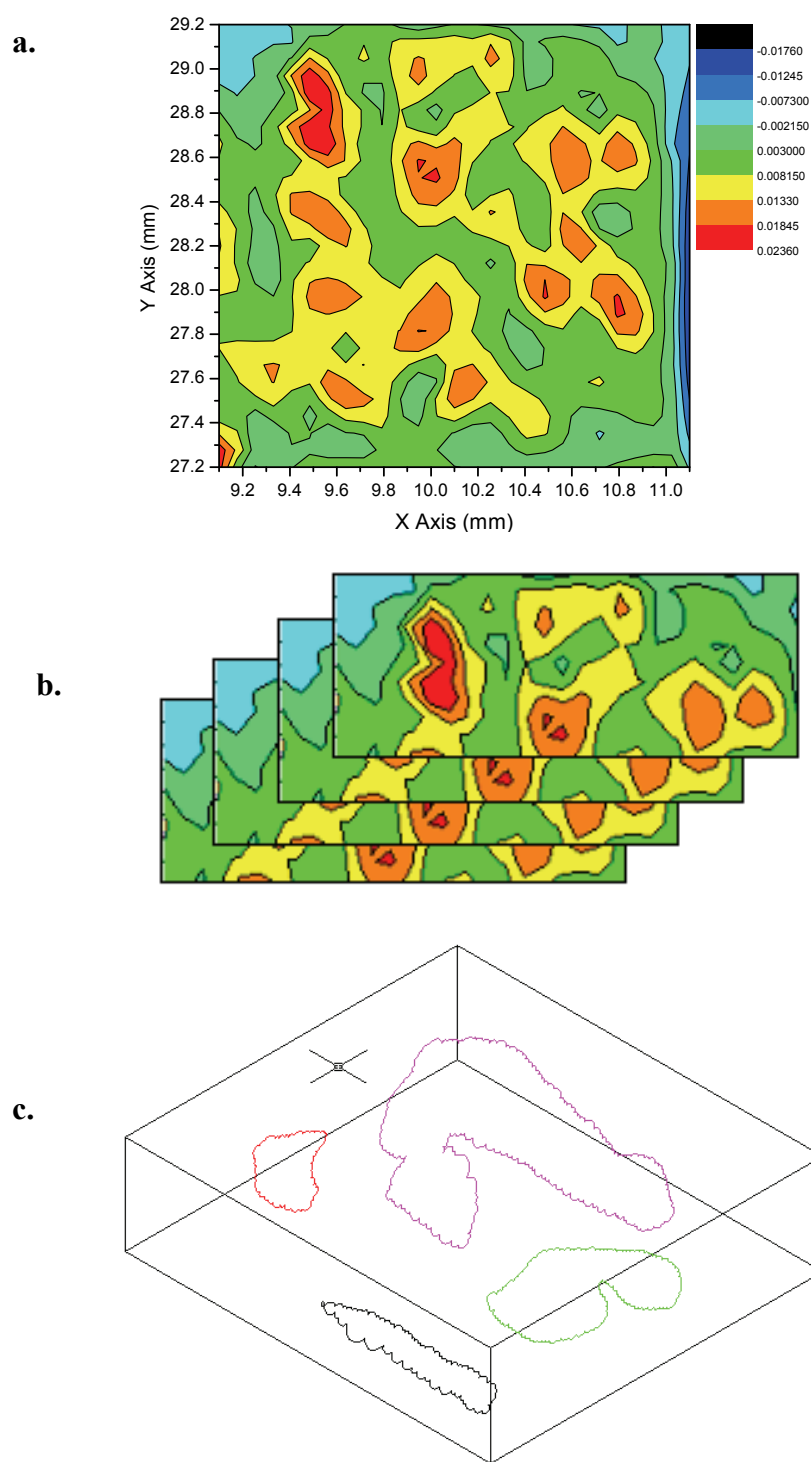


Figure 8. General scheme for 3D MS imaging by z-stacking or tissue sectioning. (a) 2D contour plot of compound X, (b) stacked 2D contour plots at different depth along the z-axis of sample, (c) 3D distribution of respective chemical constituents.

1.4 MS Methods to Image Biofilms

Microscopy has dominated the study of biofilms with the use of methods like confocal laser scanning microscopy (CLSM), SEM, and atomic force microscopy (AFM) (Bridier, et al., 2011; Ray et al., 2010; Méndez-Vilas et al., 2004). Each method possesses requirements that may limit or interfere with an imaging investigation. CLSM requires chemical derivatization of a chromophore to the target molecule for identification or monitoring. While chemical synthesis of chemically tagged analytes is challenging, consideration must be made to determine interference with the integrity of the system. CLSM also performs *in situ* studies only recently available to mass spectrometry. SEM requires a metal vapor deposited coating. Like mass spectrometry, SEM is performed in vacuum and may significantly alter the biological system's structure as a result of dehydration.

Biofilms and other biological material have been imaged by mass spectrometric methods. The next sections will elaborate on two commercially established methods along with the development of methods in postionization to image biofilms.

1.4.1 Vacuum MS Methods

1.4.1.1 Matrix Assisted Laser Desorption Ionization

Matrix assisted laser desorption ionization mass spectrometry (MALDI-MS) has been the premier method to study proteins and high mass components in biological material. With the growing popularity of MS imaging (McDonnell and Heeren, 2007) groups have strived to maintain the spatial integrity of the sample environment to capture more accurate analyte distributions through delicate pretreatment protocols and preparation methods (Lemaire et al., 2006; Altelaar et al., 2007). Matrix requirements pose the risk of target migration and disruption

of the native chemical environment (Heeren et al., 2009). MALDI-MS studied protein extracts of *Staphylococcus* biofilms but requires previous separation and pretreatment (Planchon et al., 2009). Obtaining the appropriate integration of matrix into an intact biofilm may limit their imaging studies.

MALDI-MS is commonly performed directly on biological tissue for MS imaging of molecular species (Todd et al., 2001; Wilkins, 2006; Reyzer and Caprioli, 2007). MALDI-MS has also been used to detect clinically relevant concentrations of drugs in tissue (Reyzer and Caprioli, 2007; Stoeckli et al., 2007). MALDI-MS imaging of biofilms was previously limited by various experimental effects (Edirisinghe et al., 2007), including the difficulty of forming ions from such a high salt environment while preserving the biofilm's structural integrity. However, MALDI-MS has now begun to be applied to the analysis of intact microbial systems (Liu et al., 2010; Watrous et al., 2011). Many of the technical limitation of MALDI-MS reside with controlling the size and distribution of matrix particles (Chughtai and Heeren, 2010). Also, limits of diffraction will impose boundaries to imaging resolution in MALDI and other methods based on laser desorption.

1.4.1.2 Secondary Ionization Mass Spectrometry.

Secondary ionization mass spectrometry (SIMS) has the advantage of surpassing the limits of diffraction and obtaining sub-micron imaging resolution while applying such methods to biological material. SIMS uses atomic and cluster ions in the range of 10 to 100 keV to effectively study the surface (Chughtai and Heeren, 2010), but typically displays limited high mass sensitivity (see Chapter 4). Thiel successfully detected the molecular species of a lipid from a microbial mat (Thiel et al., 2007) of considerable mass ($\sim m/z$ 1600). While work by Tyler used

SIMS to characterize the penetration and distribution of a molecular antimicrobial through a biofilm (Tyler et al., 2006). Other groups have utilized the high mass resolution of SIMS in the low mass range ($m/z < 200$) to isotopically elucidate biological chemical species (Jones et al., 2008; Kraft et al., 2006; Lechene et al., 2007; Ostrowski et al., 2004). The coupling of desorption and ionization events can introduce various issues such as sensitivity to the chemical environment, surface topology, and the relative influence of fields induced by a charging surface.

1.4.1.3 Laser Desorption Postionization Mass Spectrometry.

Methods of postionization attempt to separate the desorption and ionization channels to exploit the desorbed or ejected neutrals evolved from a surface. Postionization strategies have also been applied with success to both MS imaging experiments that utilize either primary ion or infrared laser desorption (Kriegeskotte et al., 2009; Willingham et al., 2009; Nemes et al., 2010; Galhena et al., 2010).

LDPI-MS is an MS imaging technique capable of studying biological samples which decouples the events of desorption and ionization, as discussed in a recent review (Akhmetov et al., 2010). By decoupling desorption and ionization, LDPI-MS minimizes the fluctuation in ionization efficiency with analyte which affects other MS imaging methods (Heeren et al., 2009). For example, 7.87 eV LDPI-MS was previously used to image quorum-sensing peptides and antibiotics within intact biofilms (Edirisinghe et al., 2007).

1.4.2 Atmospheric Pressure MS Methods

Electrospray ionization (ESI) can be used to transfer one or multiple charges to an analyte. Various means have been shown to desorb a sample to introduce analyte to the ESI

plume. A comprehensive review has been performed showing the application of this method as a postionization source (Huang et al., 2010). With infrared (IR) laser ablation, ESI postionization has been applied to various biological systems and successfully used to map biomolecules in animal tissues at atmospheric pressure and with minimal sample pretreatment in a method referred to as LAESI (Nemes et al., 2010; Sampson and Muddiman, 2009). By producing multiply charged species, ESI postionization can elucidate high mass proteins by deconvoluting mass peaks. However, this feature will thereby complicate the overall low mass spectrum. The combination of two ionization mechanism may interfere with quantitation and lead to reductions in sensitivity (Jorabchi et al., 2009). ESI postionization has shown utility for the study of both bacteria (Shiea et al., 2008) and biofilms (Latimer et al., 2009). Another method gaining momentum in the area of MS imaging is called desorption electrospray ionization (DESI) (Watrous et al., 2010; Svatoš, 2010).

1.5 Depth Profiling.

Depth profiling provides an additional degree of chemical-spatial information, but laser desorption/ablation is limited in its ability to allow depth profiling of biological samples. Others have found that mid-infrared, nanosecond laser pulse ablation may allow depth profiling of plant tissue (Nemes et al., 2009). However, work in laser surgery has shown that thermal and/or mechanical degradation of biological samples can result from laser pulses longer than a few picoseconds (Vogel, 2003). It has been shown that 800 nm femtosecond laser pulses may also allow depth profiling without chemical damage (Milasinovic et al., 2010). Nevertheless, new methods are needed for depth profiling.

1.6 Matrix Enhancement.

The purpose of the matrix in MALDI is to aid in the desorption of analyte from the surface into vacuum and to ionize via protonation reaction (Chughtai and Heeren, 2010). Organic matrix is chemically comprised of a chromophore to absorb UV and an acid constituent to perform chemical ionization via protonation. Three popular examples include: α -cyano-4-hydroxycinnamic acid (CHCA), 2,5-dihydroxybenzoic acid (DHB), and 3,5-dimethoxy-4-hydroxycinnamic acid (also known as sinapinic acid, or SA).

As it concerns MS imaging of tissue, matrix must be effectively integrated into the tissue sample under the following general conditions: effective integration of matrix with analyte, minimal diffusion of analyte (solvent effect), homogeneous distribution of matrix crystals, and small matrix crystals (Chughtai and Heeren, 2010). Matrix application has been performed by many methods (Heeren et al., 2009), including: droplet by hand (Sugiura et al., 2006), airbrush (Shimma et al., 2007), electrospray (Chughtai and Heeren, 2010), pneumatic spray, dry coat (Puolitaival et al., 2008), sublimation (Murphy et al., 2009; Hankin et al., 2007), ink jet (Baluya et al., 2007), and most recently, an oscillating capillary nebulizer system (Chen et al., 2008), and nano-spotting (Végyvári et al., 2010).

There are a myriad of factors that contribute to the successful use of matrix in MALDI that include: type of matrix, mass range, type of solvent, solvent ratios, matrix to solvent ratios, matrix to analyte ratio, application of matrix, and matrix purity. It is evident that matrix application is a complex process when one compounds these factors and it has been said that matrix application is “an art” and many have contrived recipes while others have attempted to characterize these factors (Chughtai and Heeren, 2010). In addition, these factors may overlap in their contribution to the MALDI event.

Major issues with matrix include the crystallization or formation of large crystals that interfere with analyte interaction, thereby suppressing desorption and limiting image resolution. Matrix produces general spectral interference in the mass range of the matrix itself. It is known that different matrices have better performance in certain mass ranges. For example, SA is used at high mass, where CHCA is best for low mass.

Recent developments have introduced new means to utilize matrix in mass spectrometry. Matrix combinations have produced more homogenous crystallization. Ionic liquids and solid matrices provide increased sensitivity for specific MS imaging experiments (Heeren et al., 2009) while reducing fragmentation and producing a good coating. (Chan et al., 2009) Coumarins and porphyrin matrices lower the chemical noise at low mass ranges (Chen and Ling, 2002; Ling et al., 1998). Gold nanoparticles are easy to derivatize and can serve as matrices that allow MS imaging at higher resolution (McLean et al., 2005; Su and Tseng, 2007). Addition of potassium acetate (Sugiura et al., 2009) or LiCl (Jackson et al., 2005) to the matrix solution provides selective ionization to detect polar and nonpolar lipids through the formation of adducts.

2 EXPERIMENTAL

2.1 Instrumentation

The LDPI-MS instrumentation underwent multiple upgrades that expanded its capabilities over the course of the work described here. Devices that improved capabilities included translation stages, redesigned ion optics, a new desorption laser, and a digital camera. Certain upgrades will also be described such as the load-lock chamber and sample transfer that did not directly impact the collection of data. The details are explained in these subsequent sections and highlight the specific improvements that distinguished each stage of improvements.

2.1.1 First Generation LDPI-MS

A custom built LDPI-MS was constructed with both linear and reflectron ToF mass spectrometers. The instrument was described in detail previously (Zhou et al., 2007), but has since underwent some changes that are described here. The major parts of this first generation LDPI-MS included the load lock for sample introduction; the main chamber which contains the pulsed ion optics, steering plates, Einzel lens, flight tube, and detectors; the 355 nm Nd:YAG desorption laser; and the postionization laser. Separate dual microchannel plate detectors were used in linear (R.M. Jordan Co., Grass Valley, CA) and reflectron modes (Advanced Performance Detector, Burle, Sturbridge, MA). Data was recorded and processed using a four channel digital oscilloscope with a bandwidth of 1 GHz (TDS5104B series; Tektronix, Portland, OR).

Vacuum was maintained using three turbo pumps backed by mechanical pumps. The base pressures in the instrument were 1×10^{-6} Torr in the load lock, 7×10^{-9} Torr in the main chamber

base and 1×10^{-9} Torr in the ToF tube. Typical operating pressures in the main chamber with a sample loaded was 9×10^{-8} Torr.

Sample desorption was achieved with a pulsed Nd:YAG laser (355 nm, 10 Hz, ~ 4 ns pulse length, Minilite II, Continuum, Santa Clara, CA). The desorption laser power was varied from 0.8 to 11 MW/cm² depending upon sample conditions to maximize desorbed neutral signal while minimizing direct ion formation (prior to postionization). The laser desorbed neutrals were postionized using a molecular fluorine laser (157 nm, 10 Hz, 10 ns pulse length, Optex Pro, Lambda Physik, Ft Lauderdale, FL) running with a gas mixture consisting of 0.075% F₂ gas in helium and fired 3 μ s after the desorption laser pulse. A MgF₂ plano-convex lens (35.3 cm focal length at 180 nm) focused the 6×3 mm² postionization laser beam about 2 mm above the sample to a power density of ~ 1 MW/cm². Each displayed mass spectrum was the average of 64 laser shots collected on a single spatial location on the sample.

The total path length in linear mode was 1.7 m with maximum resolution achieved of 500 at m/z 720 for a 5400 eV acceleration voltage. In order to increase resolution and signal-to-noise ratio, an ion mirror was constructed of 40 plates separated by 0.635 cm and connected using vacuum compatible 1 M Ω resistors (ITT Power Solutions, West Springfield, MA). The ion mirror contained one grid on the last plate (nickel mesh, 117.6 wires/inch, 88.6% transmission, InterNet Inc., internetmesh.net, Minneapolis, MN). Voltage applied to the back of the ion mirror was ~ 1.3 times greater than the acceleration voltage in linear mode. The total path length in reflectron mode was 2.4 m with maximum resolution ($m/\Delta m$) of 1200 achieved at m/z 397.

Linear detection was insufficient given the sample plate and detector face were in the same plane. Despite being insensitive, the production of hot neutrals could not be discriminated against. Hot neutrals occur when the desorption laser creates highly energetic neutral molecules

from the sample surface with enough kinetic energy to strike the detector and produce signal. This leads to false mass identifications. Figure 9 shows the 355 nm desorption laser irradiated the sample surface to produce hot neutrals (1), hot ions (2), and cold ions (3) in vacuum. After ionization, all three travel down the ToF tube. When the ion mirror is turned off, all three strike the linear detector to produce ion current. With the ion mirror ON, only ions (hot and cold) will be reflected toward detector 2.

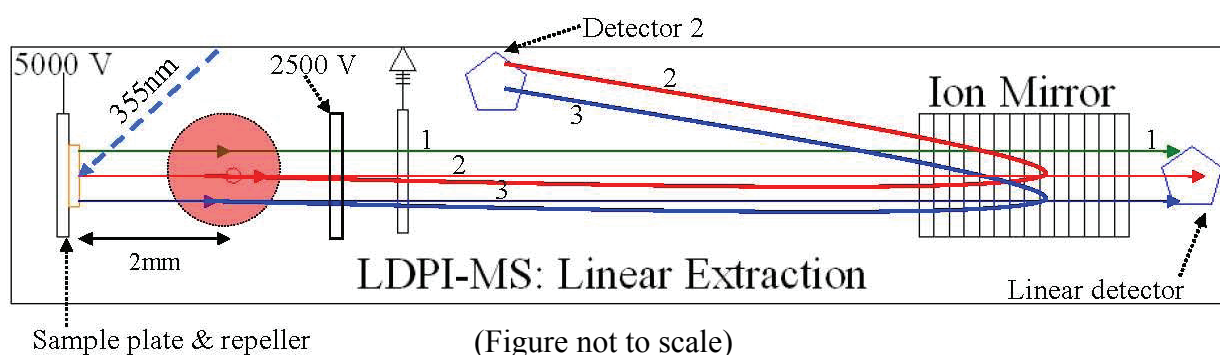


Figure 9: First generation LDPI-MS with linear extraction.

Particles produced during experiment (1) hot neutrals, (2) hot ions, (3) cold ions. Instrument components include: 355 nm YAG desorption laser, sample and repeller plate (5000 V), extraction plate (2500 V), ground plate (0 V), ion mirror, linear detector, detector 2.

2.1.2 Second Generation LDPI-MS

The second generation instrument employed a YLF laser for desorption (Explorer, Spectra-Physics, Stahndorf, Germany) that operated at 349 nm wavelength, 15 ns pulse duration with a 20-25 μm diameter focal spot on the sample, and 8 μJ pulse energy for an irradiance of 100 MW/cm^2 at the surface. The same molecular fluorine laser (157 nm) was used for postionization with an irradiance of $\sim 1 \text{ MW}/\text{cm}^2$. However, both lasers operated ten times faster than the previously stated design, at experimental repetition rates of 100 Hz. Some details of this instrument were described in a recent publication (Akhmetov et al., 2010).

Figure 10 shows reflectron mode was primarily used under this instrument configuration. However, linear detection was available. Hot neutrals (a), and ions (b) escaped vertically from the sample plate. After ionization of cold neutrals (c), these cold ions were extracted through ion optics for detection.

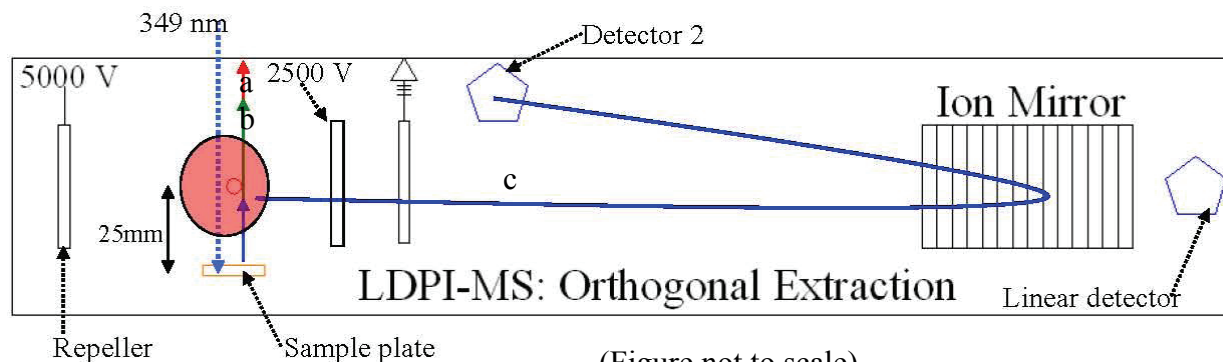


Figure 10: Second generation LDPI-MS

Particles produced during experiment (a) hot neutrals, (b) hot ions, (c) cold neutrals. Instrument components include: 349 nm YLF desorption laser, sample plate, repeller plate (5000 V), extraction plate (2500 V), ground plate (0 V), ion mirror, linear detector, detector 2 (Figure not to scale).

A more detailed drawing of the second generation LDPI-MS is provided in Figure 11. This computer aided draft (CAD) rendering provides a cut away section of the instrument to allow both an external and internal visualization. The LDPI-MS instrument schematic includes: ionization/extraction region ion optics (a, with an inset zoom of the ion optics), reflectron (b), reflectron detector (c), translation stage (d), load lock (e), 349 nm Nd:YLF desorption laser (f), and 7.87 eV (157 nm) molecular fluorine laser for VUV postionization (g), camera assembly (h).

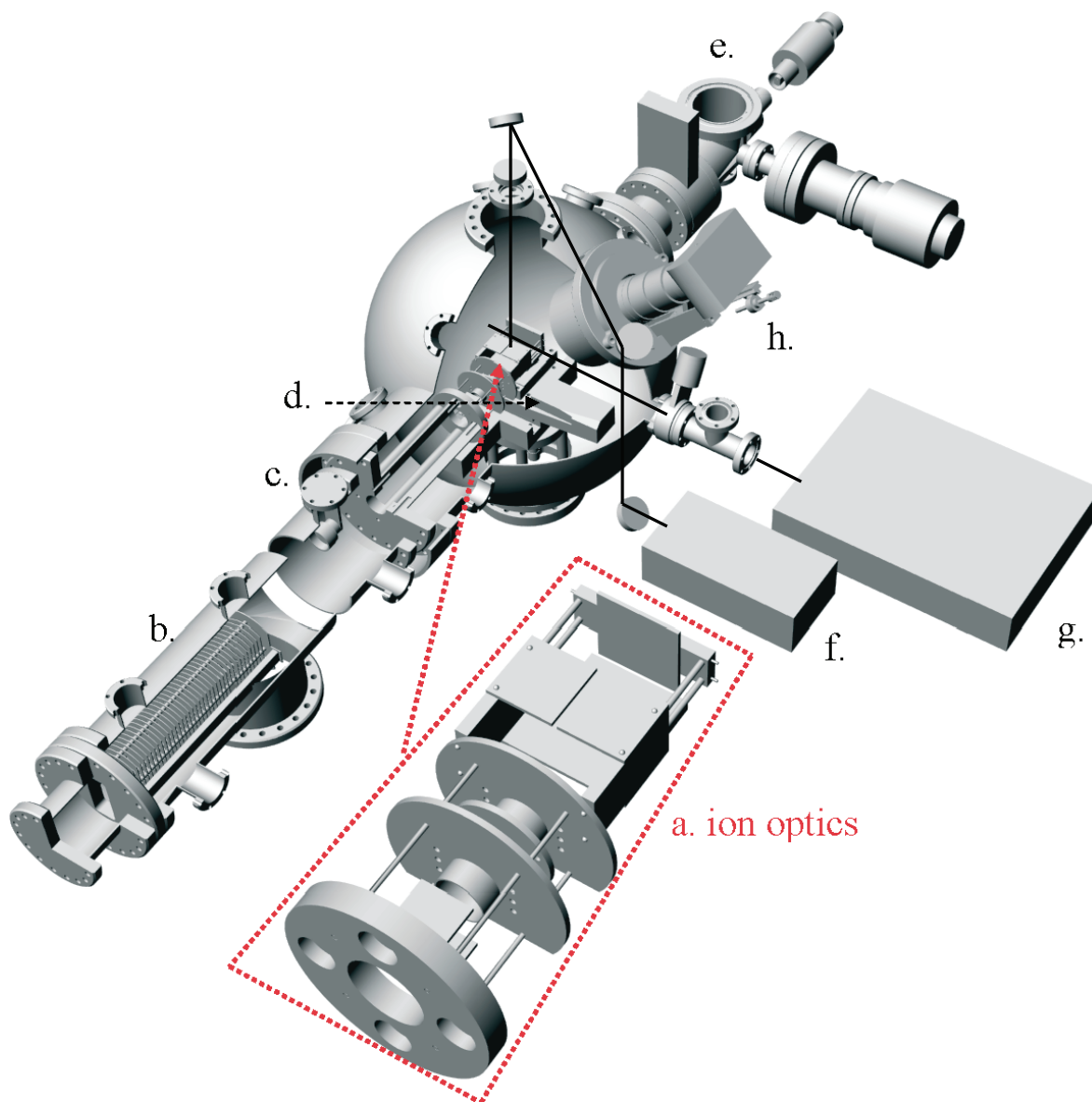


Figure 11: Computer aided drawing of second generation LDPI-MS instrument. LDPI-MS instrument schematic: (a) ionization/extraction region ion optics, (b) reflectron, (c) reflectron detector, (d) translation stage, (e) load lock, (f) 349 nm Nd:YLF desorption laser, and (g) 7.87 eV (157 nm) molecular fluorine laser for VUV postionization, (h) camera assembly. Inset image (a) zoom of LDPI-MS ion optics. Note three mirrors deflecting desorption laser beam.

Most of the spectra presented here were collected using an ion optical design in which ions were extracted along a serpentine path to the ToF analyzer which allowed complete discrimination between postionized neutrals which form a few mm above the sample and directly

desorbed ions (Moore et al., 2010). After desorption and postionization, ions were extracted from the source region via a pulsed positive bias repeller plate, followed by dual-axis alignment with a set of three ceiling and floor plates, focused through an Einzel lens and final alignment with single-axis steering plates before drifting through the ToF analyzer with two stage reflectron. Additional detail about this ion optics design can be found in the following sections discussing instrument upgrades.

Other devices for imaging included UHV stages and digital camera. MS imaging was provided by a vacuum compatible translation stage (Micos USA LLC, Irvine, CA). Optical images were taken with a digital camera (Nikon D300, Nikon Corporation, Japan) equipped with a micro lens (Nikon ED, AF Micro Nikkor, 200 mm, 1:4D).

2.1.2.1 MS Imaging and Data Collection

LDPI-MS images were performed using a set of ultra high vacuum (UHV) translation stages (Micos USA LLC, Irvine, CA) performed a programmed back-and-forth scan with custom written software (LabView, National Instruments Corporation, Austin, TX) under a fixed desorption laser beam removing material from the sample resulting in a neutral plume followed by pulsed postionization. Mass spectra were collected and averaged with a digitizer card (Gage Applied Technologies Inc., Lockport, IL USA) at 100 Hz, and assigned a space coordinate. From this data cube, intensities within a user defined mass range were extracted, integrated, and plotted with space coordinates to form a contour map with Origin8.0 (OriginLab Corporation, Northampton, MA, USA). Contour maps for CHCA matrix study were produced by converting data cube by an in-house MatLab (Math Works, Natick, MA, USA) algorithm and analyzed with

open source software (BioMap, freeware downloaded from www.maldi-msi.org). Three replicate measurements were performed for each sample.

2.1.1.2 Instrument Control Experiments

LDPI-MS control experiments employed a constant pressure of triethylamine vapor leaking into vacuum to monitor stability of the postionization signal. MS images from a surface of uniformly C₆₀-coated silicon substrate were also investigated as a control for signal uniformity.

All LDPI-MS experiments included controls for direct ionization with either desorption or postionization lasers. The presence of direct laser desorption ionization signal (referred to as LD) was tested by simply blocking the postionization laser while desorption laser was fired. Similarly, background due to the postionization laser hitting surfaces or ionizing residual vapor was tested by closing desorption laser shutter. Three to five replicates were run of each sample to ensure validity.

2.1.3 LDPI-MS at the Advanced Light Source

In addition to aforementioned instruments at UIC, some experiments were performed at the Advanced Light Source (Lawrence Berkeley National Laboratory, Berkeley, CA) These studies used a modified commercial secondary ion mass spectrometer (TOF.SIMS 5, ION TOF Inc., Münster, Germany) coupled to a desorption laser (Explorer, Newport, Nd-YLF 349 nm). This instrument was also coupled to synchrotron VUV radiation at the Chemical Dynamics Beamline at the Advanced Light Source (Heimann et al., 1997). The experimental configuration is shown schematically in Figure 12 and was described previously (Takahashi et al., 2009)

except for the coupling of the desorption laser. Adjusting the undulator gap on the beamline allowed tuning of the VUV photon energy from 8.0 to 12.5 eV photon energy with a spectral bandwidth of 0.22 eV (Heimann et al., 1997). An argon gas filter was used to remove higher energy harmonics. The VUV beam was focused by beamline optics to a 280 μm vertical \times 490 μm horizontal waist, which was aligned so that the beam barely grazed the sample. The extraction cone of the mass spectrometer was 1.5 mm above the sample surface (Takahashi et al., 2009).

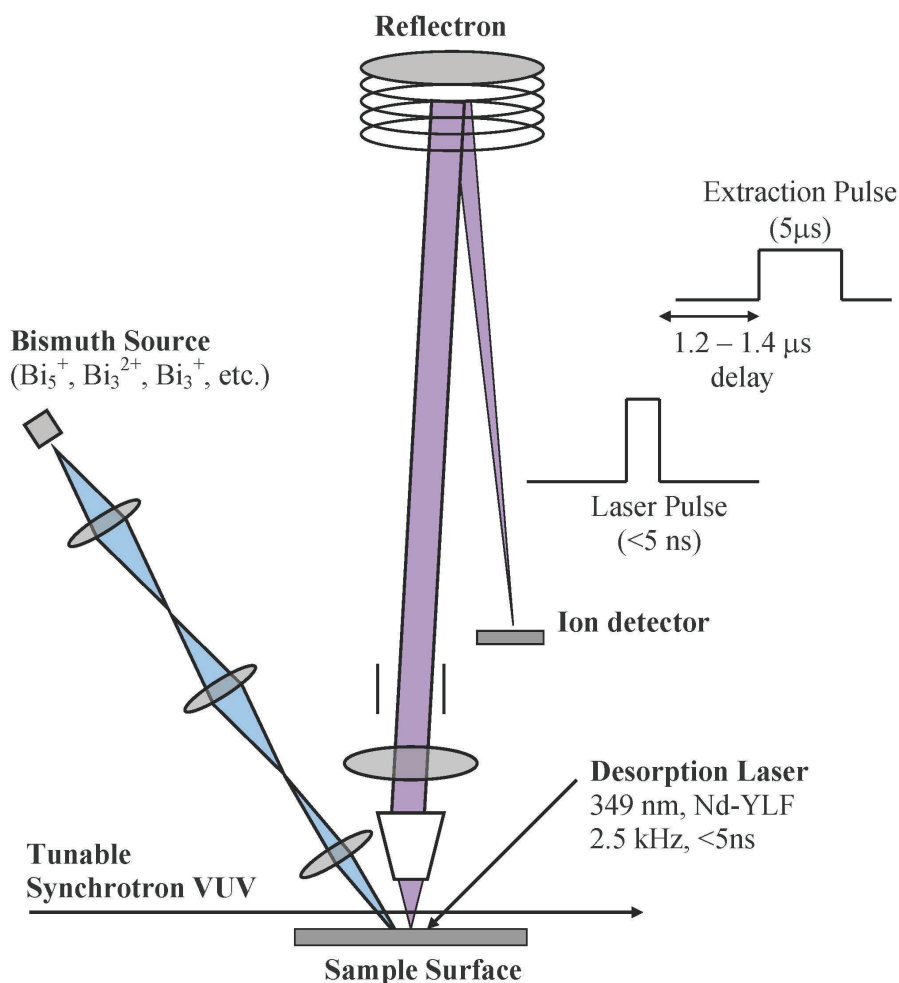


Figure 12: Schematic of TOF-SIMS instrument at the Advanced Light Sources. Schematic of TOF-SIMS instrument adapted for LDPI-MS. Includes added Nd-YLF desorption laser, vacuum ultraviolet synchrotron radiation, and extraction pulse timing scheme.

The Nd:YLF desorption laser was operated at a repetition rate of 2500 Hz and focused to a ~ 300 μm spot diameter. The sample stage was fixed with respect to the desorption laser spot during data acquisition. The < 5 ns pulse delivered peak power densities of $2 - 10$ MW/cm^2 when operated in the range of $6 - 34$ $\mu\text{J}/\text{pulse}$. Desorbed neutrals were photoionized by the quasi-continuous synchrotron radiation, and were extracted by a 5 μs long ion extraction pulse beginning $1.2 - 1.4$ μs after the desorption laser. Mass resolution of the instrument in the LDPI mode was measured as ~ 1000 for a sample of 2,5-dibromotyrosine on a gold substrate, but spectra on biofilms are broader due to charging effects. All displayed spectra are the sum of 143,000 laser shots during sample analysis which occurred in 57 seconds. An instrumental configuration used a 349 nm Nd:YLF desorption laser (Explorer, Newport Corp, 5 ns pulse length, 300 and 25 μm spot, 2 - 100 MW/cm^2) and tunable, monochromatized 8 - 24 eV synchrotron radiation. Mass spectra were averaged from 80,000 to 200,000 laser shots. EUV spectra were not normalized to the beam flux to account for differences in synchrotron fill and beamline transmission at different wavelengths and hence an absolute comparison to the VUV data cannot be performed.

2.1.4 Scanning Electron Microscopy.

SEM (Model S-3000N, Hitachi) with a tungsten electron source operating at 15 keV electron energy under high vacuum was used to obtain images of the colony biofilms. Biofilm samples were treated the same as described above for LDPI-MS except that they were not transferred to agar with antibiotic. The biofilms were then fixed with 2.5% glutaraldehyde in sterilized deionized water, dehydrated by treatment with a gradient series of ethanol:water solutions, dried overnight in a desiccator, and coated with platinum/palladium alloy (Fraud et al.,

2007). Scanning electron micrographs indicated an average *S. epidermidis* microbe diameter of ~0.8 μm and verified an absence of contamination by other microbes (not shown).

2.1.5 Analyte and Signal Decay Experiment

To establish the rate of loss of the analyte signal with successive desorption pulses, a biofilm was grown on a polycarbonate membrane and doped with a saturated solution of rifampicin. An experiment was performed at twenty-two separate single spots to study the analyte signal decay without stage motion. The repetition rate was reduced to 5 Hz so that each spectrum could be recorded without any missed laser shots. A breadth of 4 mass units was integrated from this signal at each of twenty-two locations and this resulting data set averaged to produce a single decay curve plotted against time.

2.1.6 Mass Calibration

Mass calibration was performed with various compounds but most effective were sexithiophene (mol. wt. 494 Da, Sigma-Aldrich) and [6,6] diphenyl C_{62} bis(butyric acid methyl ester) (mol. wt. 1100 Da, Sigma-Aldrich) which covered the mid to high mass range. Calibration curves were constructed with these calibrants where known peaks were assigned using exact mass calculations. Correlation plots between mass and time were fitted with a second-order curve. Coefficients to a second-order polynomial were entered into the instrument, where ion arrival time was directly converted to mass.

2.2 Sample Preparation.

2.2.1 Neat Sample Preparation.

Neat antibiotics (Sigma-Aldrich, Milwaukee, WI, USA) and calibrants were applied to an indium tin oxide (ITO) coated glass microscope slide (Sigma-Aldrich) or stainless steel sample plate (AB Sciex LLC, Foster City, CA, USA) as a dried droplet and analyzed by LDPI-MS, shown in Chapter 3.

2.2.2 Growth of Membrane Colony Biofilm and Treatment.

Protocols for biofilm fixation are not as well established as those for animal tissue (Malm et al., 2009). Figure 13 shows colony biofilm growth and treatment, which generally followed previously published procedures (Xu et al., 1998; Huang et al., 1998; Stewart et al., 2001). A freeze-dried bacterial pellet of *S. epidermidis* ATCC35984 cells (ATCC, Manassus, VA) was rehydrated in 5 mL of tryptic soy broth (Fisher Scientific) in a 15 mL test tube, incubated at 37° C in a water bath, and agitated with a magnetic stir bar to provide oxygenation to planktonic solution for 12 to 18 hours. A new 5 mL of tryptic soy broth solution was prepared, inoculated with 100 µL of stock bacterial solution, and incubated for an additional 12 to 18 hours with agitation. Petri dishes were prepared with 25 mL of tryptic soy agar (Fisher Scientific) each with four ultraviolet sterilized polycarbonate membranes (Millipore, 0.20 µm pore size, 25 mm diameter, Fisher Scientific), which provided structural integrity to the biofilms. Each membrane was inoculated with 10 µL of cultured bacterial solution, and incubated for 71 hours with the transfer of biofilm membranes to fresh agar plates every 24 hours. Biofilm membranes were transferred to agar doped with the desired antibiotic (Sigma-Aldrich) at the given concentration and incubated for the last hour of growth. Figure 14 depicts an image of a mature 72-hours membrane biofilm.

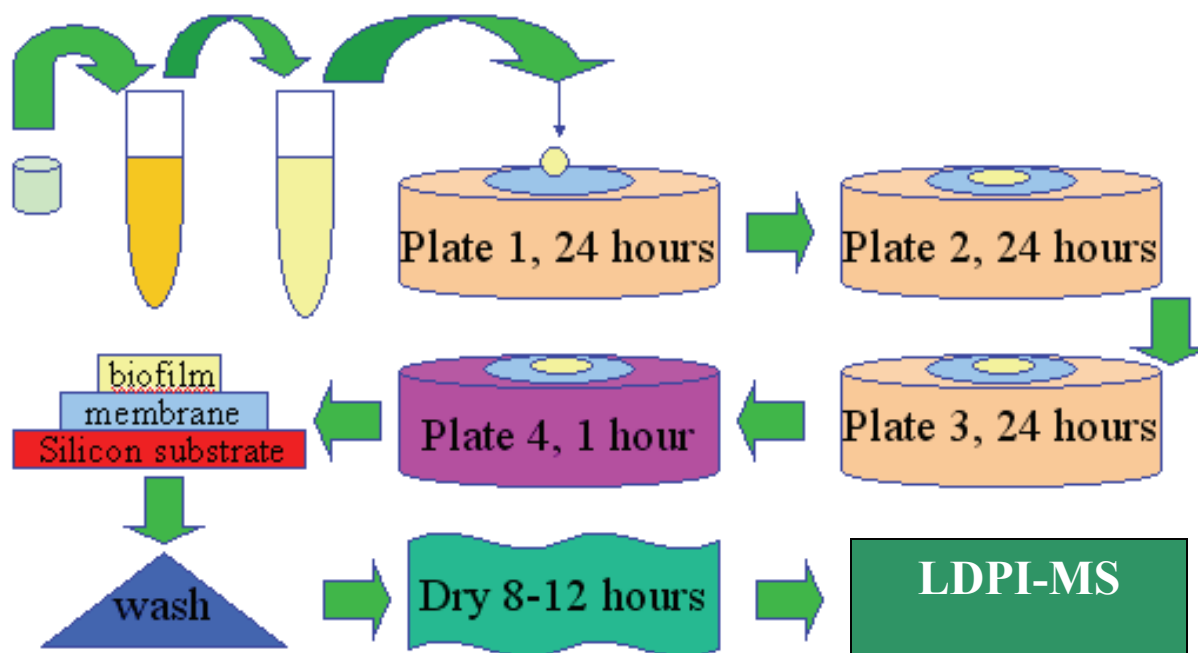


Figure 13: Cartoon depicting preparation of colony biofilm.

Eleven steps: Pellet, hydration, nutrient addition, plate 1 (24 hours), plate 2 (24 hours), plate 3 (24 hours), plate 4 (antibiotic doped, 1 hour), mounting to substrate, wash, dry, LDPI-MS analysis.

The colony biofilm still attached to the polycarbonate membrane was transferred to a silicon substrate and anchored with carbon tape, thereby preventing the biofilm from cracking due to wrinkling or buckling of the membrane. Biofilms were treated with two 50 μ L washes of 1:1 acetonitrile/deionized water solution each followed by 15 minutes of drying. The biofilms were then dried in a desiccator for 6 to 12 hours. The biofilm on the membrane along with the underlying silicon substrate were secured to a stainless steel sample holder with carbon tape for introduction to the vacuum system.

2.2.3 Drip Flow Biofilms on ITO Slides and Silicon Wafers.

Biofilms were also grown directly on substrates by drip flow on silicon wafers (Wafer World Inc., West Palm Beach, FL, USA) and ITO coated glass microscope slides (Sigma-

Aldrich) in accordance with literature methods (Xu et al., 1998; Goeres et al., 2009). Growth on silicon and ITO substrates provided structural rigidity and flatter surfaces than those grown on membranes. Silicon and ITO substrates mounted in flow cell lanes were inoculated with 1 mL bacterial culture containing $\sim 1 \times 10^8$ colony forming units (CFU) per mL. A fresh nutrient supply of 9 mL of tryptic soy broth (TSB, Fischer Scientific) was added to each lane. Flow cells were incubated at 37°C without inclination of the apparatus for 12 hours of static growth to promote initial adhesion of bacterial cells to ITO surface. The second stage of growth (shear growth phase) occurred for 12 hours under a flow of 3.6 mL/hour of full strength TSB with the flow cell apparatus tilted downward at 10°. Drip flow biofilms on ITO substrates were removed and 50 μ L of antibiotic at a concentration of 2 mM was administered to each sample ($\sim 2 \times 2$ cm area). Biofilm concentration was defined by the concentration of the antibiotic administered. Drip flow biofilm experiments on silicon substrate concentration were defined according to the moles of antibiotic per liter of nutrient supply administered during the last hour of growth. Samples were allowed to dry for two hours before instrument introduction. Control biofilms were prepared in the same fashion as the above samples, but without antibiotic doping.

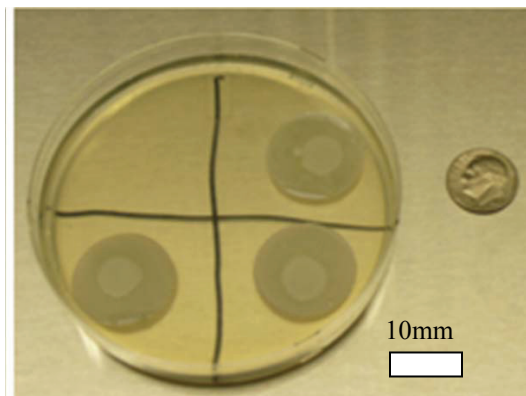


Figure 14: Picture of membrane biofilm.

Membrane bacterial biofilm grown on nutrient agar are about 7 mm in diameter and $\sim 300 \mu$ m thick. Scale bar = 10mm.

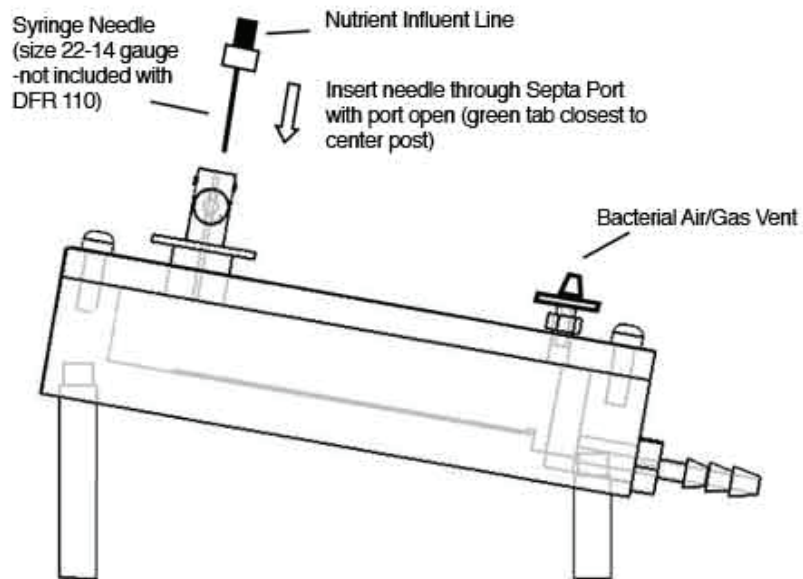


Figure 15. Image and schematic of drip flow cell for biofilm growth. Schematic of drip flow cell showing nutrient inlet line, air/gas vent, and fluid outlet.

2.2.4 Cross Sectioning of Membrane Biofilms

Bacterial biofilms were sectioned on a cryomicrotome according to methods established for optical microscopy (Yu et al., 1994). Biofilms were grown on polycarbonate membranes as described above, then placed on dry ice while optimal cutting temperature (OCT, Sakura Finetek USA Inc., Torrance, CA) compound was applied on top to embed the film. Once the OCT hardened, the membrane could be peeled from the biofilm and additional OCT applied to the membrane-side of the biofilm to completely encase it. The resulting embedded biofilm disk was broken in half to expose the sandwiched biofilm and then mounted on the cryomicrotome. Preliminary slices were taken to obtain a uniform section and then sequential sections were taken and mounted on a silicon chip. Each cross section was mounted horizontally in order to allow MS imaging of antibiotic distribution through the biofilm depth axis. There were three successful

replicates with an associated failure rate of 75%, where failures were due to torn or irregular sectioning.

2.2.5 Biofilm Viability Studies.

Cultures for biofilm cell counts and viability studies were prepared as noted above with the following modifications: after exposure to tetracycline doped agar plates, the biofilm containing membranes were harvested into 9 mL of phosphate buffer solution. The bacterial cells were recovered from the membranes by vigorously vortexing for one minute. The recovered biofilm samples were homogenized and diluted using previously reported techniques (Xu et al., 1998; Huang et al., 1998; Stewart et al., 2001). The minimal inhibitory concentration of tetracycline for planktonic *S. epidermidis* cells was $\sim 0.38 \mu\text{g/ml}$ ($0.86 \mu\text{M}$) as determined using antibiotic gradient test strips (Etest, AB BIODISK, Solna, Sweden) and the manufacturer's guidelines. All samples were run in triplicate and the standard deviations reported as errors.

Figure 16 imaged the result of all three trials.

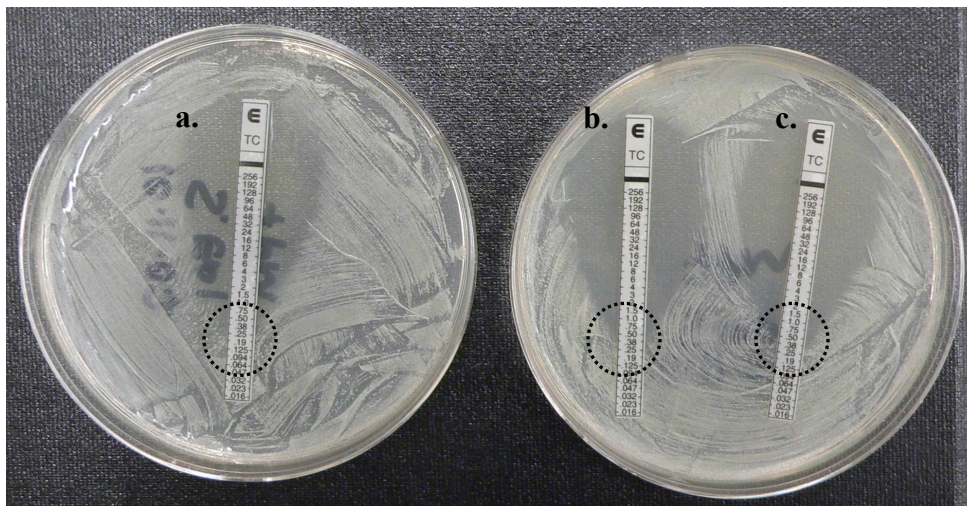


Figure 16. *S. epidermidis* cell viability using tetracycline gradient test strips. Dotted circles highlight colony growth stops (indicated by clear area) near $0.38 \mu\text{g/mL}$ tetracycline in all three trials (a, b, and c).

2.2.6 Matrix Application.

The matrix compound CHCA (Sigma-Aldrich) was applied to biofilm samples by either airbrush or nano spotter. CHCA was applied at a concentration of 20 mg CHCA/mL (70:30 acetonitrile:deionized water with 0.1% TFA) (Todd et al., 2001), with an airbrush (Testors Corp., Rockford, IL, USA) (Hexter, 1980). Two to three coats were sufficient for these studies. Thirty seconds of drying was allowed between coats. Matrix application with nano spotter (NanoLiter Cool-Wave System X, NanoLiter LLC, Henderson, NV, USA) (Végyvári et al., 2010) used three matrix concentrations: 5, 10 and 20 mg CHCA/mL under the same solvent conditions and described above. Matrix-solvent volumes were ~40 – 80 nL, ~350 – 700 μm in size, and a ratio of matrix to analyte per area of 100:1 ($\text{mol}_{\text{matrix}}/\text{mol}_{\text{analyte}}$).

2.3 LDPI-MS Mechanical Instrumental Upgrades.

AutoCAD is a powerful technical drawing software commonly used to communicate, design, and document instrument ideas. Skills in technical drawing provide many important roles in instrumentation design and implementation. The Department of Chemistry at UIC has its own machine shop with computer numerical control (CNC) capabilities. Properly prepared 3D drawings can be emailed to the machine shop, and programmed into the machinery to start production.

Instrument design starts as an objective to add or create a machine component. In many cases the component exists and may simply require installation. In some cases, the component must be cleared for geometry and may require simulation or geometry testing with AutoCad. In other cases, unique components are demanded and prototyping is required. The ability to “build” in 3D within AutoCAD proves another advantage and leads to streamlined results going from

design to prototype. One of the final purposes for preparing technical drawings is to maintain an accurate record of machine components and designs.

Instrumental components were designed and drafted with AutoCAD. Then, prototypes were submitted for custom in house fabrication. Mechanical upgrades were implemented and tested. Some designs were replaced with further improved designs resulting from geometric restrictions or changes to previous user demands. This section will include currently used designs for the second generation LDPI-MS instrument that were designed and implemented. Selected mechanical projects will be discussed, the list of upgrades include: customized sample receiving plate, ion optics, sample stage, translation stage coupling and support structure, laser optics substructure, re-entrant flange for camera, camera mount and translation rail, sample receiving plate, sample transfer arm off-center flange, recessed flange for ion gauge, laser shield, laser periscope, load lock supports, laser optics hardware. These mechanical upgrades lead to new capabilities to perform: laser desorption normal to the sample surface, MS imaging, embedded microscope, rapid sample transfer, higher duty cycle data acquisition, and improved sample throughput.

2.3.1 LDPI-MS Segments

The LDPI-MS instrument is broken into four segments. As shown in Figure 17, the instrument includes a load lock area where samples at atmospheric pressure are introduced into a vacuum environment. The load lock also serves to transfer sample into the main chamber where analysis will take place. An interlock resides between these two chambers to reduce exposure to contaminants and maintain vacuum in the main chamber. Another interlock is found between the main chamber and the ToF to protect the detectors from moisture and oxidation. The main

chamber contains the largest number of components as it is central to physical events that initiate and deliver ions for analysis. The main chamber includes mechanical platforms to mount the sample along with translation stages for controlled programmed movements for MS imaging experiments. A nested flange houses a camera assembly with a micro lens to provide optical sample images. The ion optics are centrally located in the main chamber and used to extract and direct ions produced during the ionization of desorbed neutrals. Lastly, the laser table supports the desorption and ionization lasers along with optics to direct and refine their beams. Also in the laser area, a conversion cell (Xenon cell) filled with Xe gas converts 355 (YAG) to 118 nm (10.5 eV) photons. Both 118 and 157 nm beams are VUV and integrated into the vacuum chamber to prevent absorption by gases.

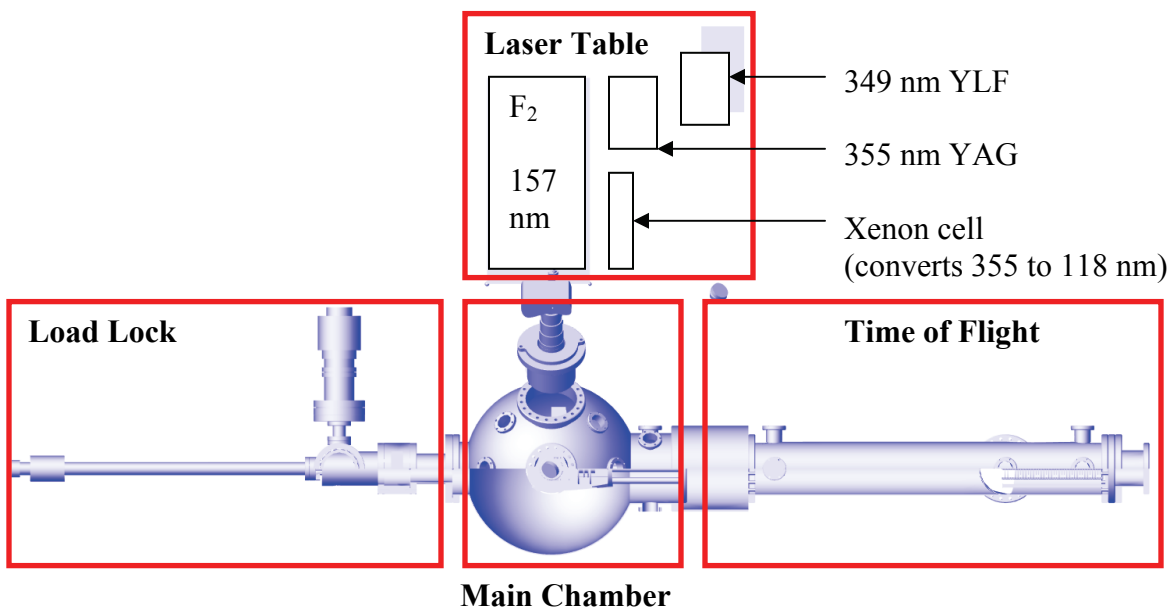


Figure 17: Four segments of LDPI-MS instrument (top view).
 Top view of LDPI-MS instrument is divided into four segments: load lock chamber, main chamber, ToF tube, laser table.

Major components that were implemented into the LDPI-MS instrument will be briefly discussed. Mechanical projects included: ion optics, 118 nm Xe conversion cell, camera mounting assembly, UHV stage mounting assembly, sample transfer arm off-set flange, load lock support assembly, and UHV stage spacer.

2.3.2 LDPI-MS Ion Optics

The LDPI-MS ion optics serves a critical purpose in extracting and directing ions from the source to the ToF analyzer in a serpentine manner that discriminated direct ions ejected from the sample surface (Moore et al., 2010). Figure 18 provides a CAD drawing to display a closer look and a cross section for a more descriptive perspective. The LDPI-MS instrument has undergone an additional upgrade that includes further improvement to the ion optics that will not be covered in this thesis.

The ion optics, shown in Figure 18, was commissioned to accommodate the horizontal geometry of the ToF tube while allowing the sample to be introduced in the same plane as the floor. Ion extraction was performed by positively biasing the sample plate ~4000 V. Next, a pulsed extraction from the “back plate” repelling the ions toward the ToF. The “ceiling plates” created the first serpentine curvature of the ions while the “floor plate” stabilized the ions into a second curved trajectory that led the ion packet through further refining ion optics, such as the Einzel lens and “steering plates”.

Additional devices were constructed to adapt specific upgrades. A camera support assembly was created to mount and stabilize a digital camera for taking optical images of the sample surface to overlay with MS images. The UHV translation stages required a rigid support assembly. An off-set flange was constructed to account for the clearances required for the ion

optics while allowing for smooth sample transfers. With the addition of multiple hardware to the load lock, a support structure was created to reduce the mechanical load imposed on welded joints of the main chamber. Finally, the geometry of the UHV translational stages includes a spacer to allow a complete range of motion.

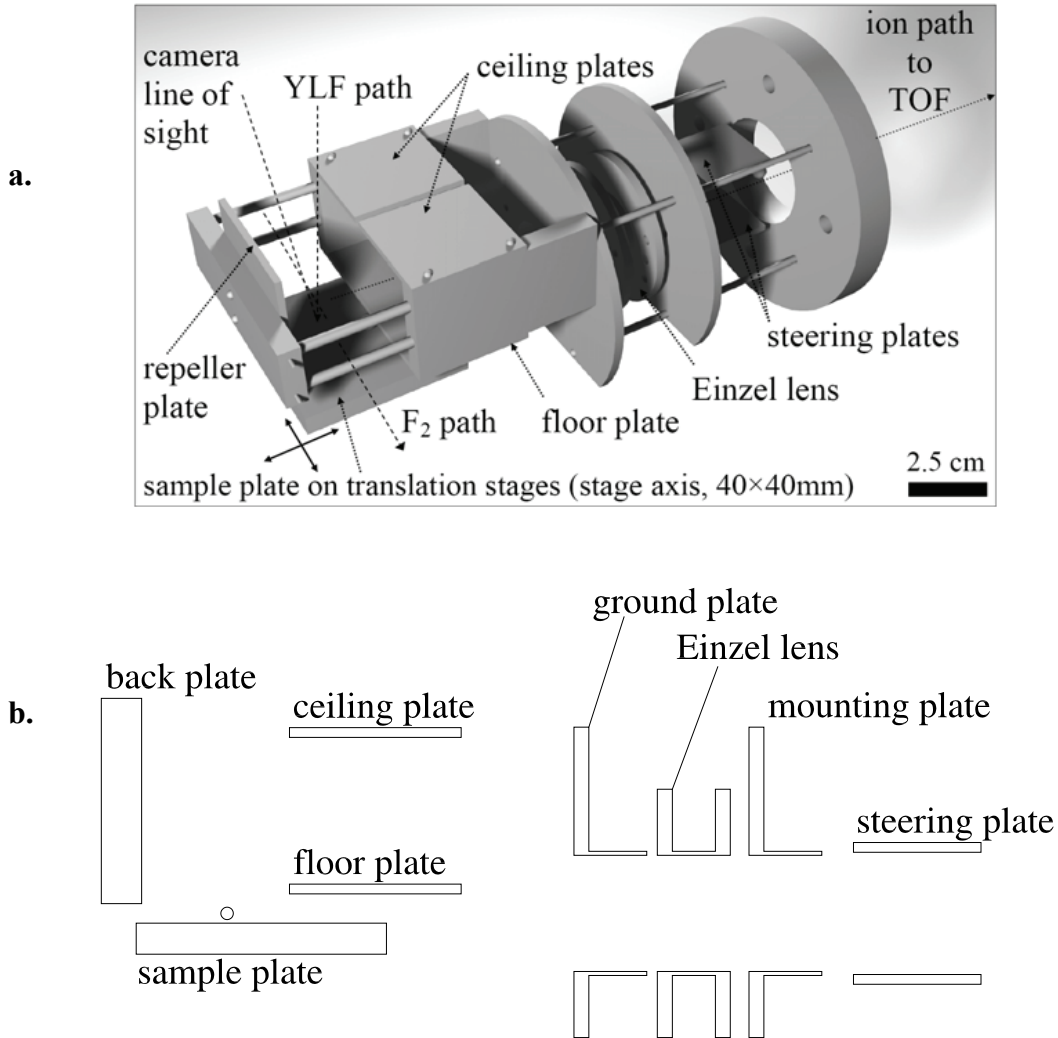


Figure 18: CAD rendering and cross section of second generation LDPI-MS ion optics. (a) Ion optics rendering include: sample plate, repeller plate, ceiling plates, floor plate, ground plate, Einzel lens, and steering plates. Scale bar = 2.5 cm. (b) cross section of ion optics with similar labels.

**3 VACUUM ULTRAVIOLET, 7.87 EV, POSTIONIZATION OF LASER
DESORBED NEUTRALS TO DETECT ANTIBIOTICS IN *STAPHYLOCOCCUS
EPIDERMIDIS* BACTERIAL BIOFILMS:**

3.1 INTRODUCTION

This chapter describes the development of 7.87 eV LDPI-MS to detect antibiotics within intact bacterial biofilms. The experimental configuration of LDPI-MS is essentially that of a MALDI-MS with a molecular fluorine laser added for postionization. Five antibiotics with structures indicative of sub-7.87 eV ionization energies were examined for their ability to be detected by 7.87 eV LDPI-MS without chemical derivatization. Tetracycline, sulfadiazine, and novobiocin were successfully detected neat as dried films physisorbed on porous silicon oxide substrates, then examined within intact *S. epidermidis* bacterial biofilms. Azithromycin and coumermycin A1 were found to not be detectable neat by 7.87 eV LDPI-MS and were not examined further.

3.2 EXPERIMENTAL

The experiments in these investigations were performed with the first generation LDPI-MS with both linear and reflection modes. Biofilms were prepared on membranes with tryptic soy agar (TSA) nutrient medium. Samples were mounted on silicon substrate with conductive carbon tape to maintain a flat surface. Viability studies verified the minimum inhibitory concentrations (MIC) of tetracycline on *S. epidermidis*.

3.3 RESULTS AND DISCUSSION

3.3.1 Detection of Neat Antibiotics

Figure 19 displays the LDPI-MS spectra of tetracycline, sulfadiazine, and novobiocin deposited on separate porous silicon oxide substrates (Wei et al., 1999). The antibiotics were laser desorbed at 355 nm with 0.8 MW/cm² power density, postionized with 7.87 eV vacuum

ultraviolet radiation, then detected in linear ToF mode. Concurrent spectra of each antibiotic were also recorded at the same laser desorption power densities but with the postionization laser beam blocked (data not shown). None of the laser desorption only spectra showed any significant ion formation above $\sim m/z$ 100, indicating that the spectra in Figure 19 represented postionization of laser desorbed neutrals. Furthermore, each sample was tested for and found to lack postionization signal from evaporated species in the absence of laser desorption.

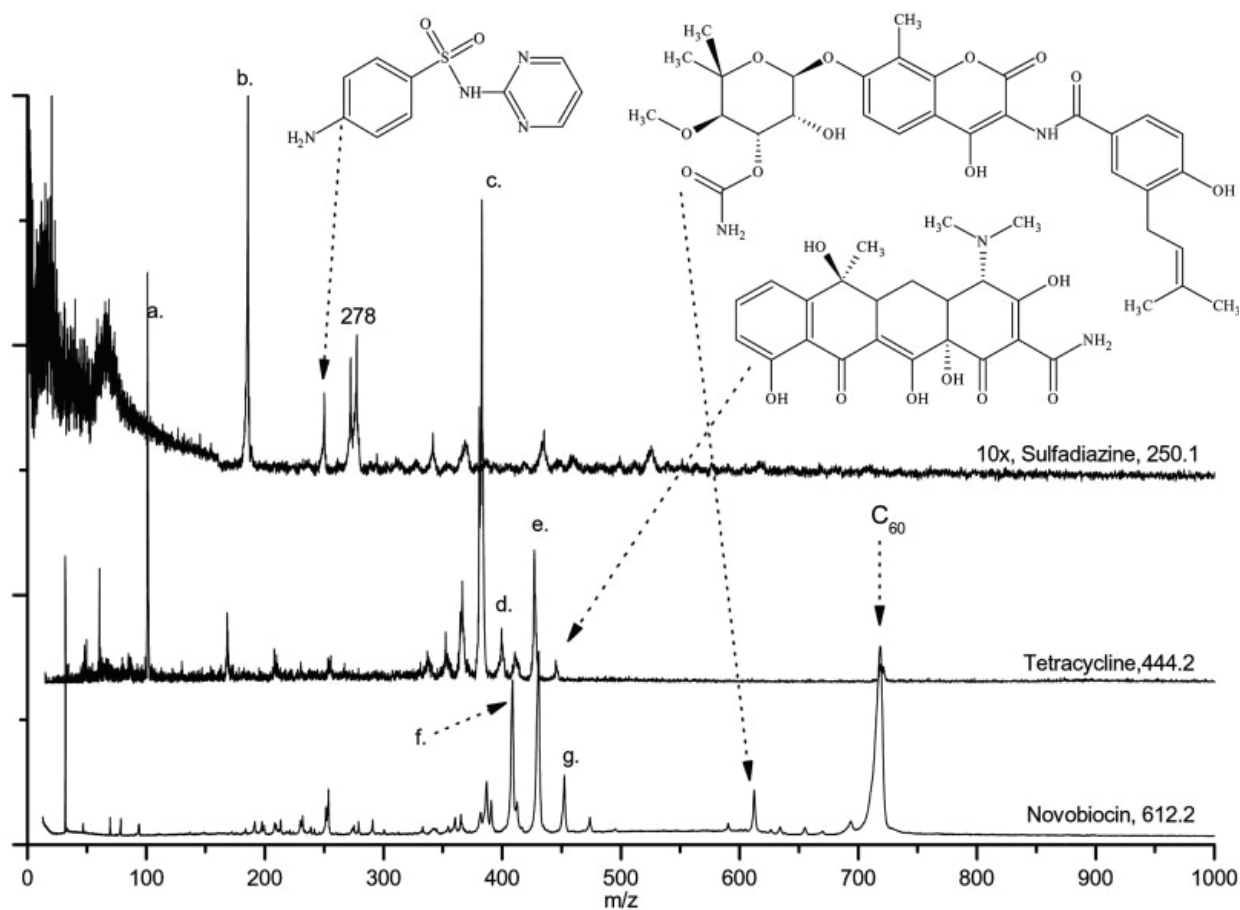


Figure 19: 7.87 eV LDPI-MS of neat antibiotics.

Laser desorption 7.87 eV VUV postionization mass spectra (LDPI-MS) of neat sulfadiazine, tetracycline, and novobiocin physisorbed on porous silicon oxide.

LDPI-MS of novobiocin, tetracycline, and sulfadiazine all displayed intact radical cations at m/z 612, 444, and 250, respectively, of the undissociated parent (structures displayed for each compound in Figure 19 with arrows connecting the chemical structures to the parent ion peaks). Tetracycline displayed several prominent fragments, two of which were readily identified as the parent after loss of hydroxyl or dimethyl amino groups to form $[M-OH]^+$ at m/z 427 (labeled d. on Figure 19) and $[M-NMe_2]^+$ at m/z 400 (labeled e.), respectively. The most intense peak occurred at m/z 383 (labeled c.) and resulted from loss of both groups to form $[M-OHNMe_2]^+$. Other characteristic tetracycline fragment ions appeared at m/z 410 due to loss of a hydroxyl from the m/z 427 fragment and m/z 357 due to loss of an amide group from the m/z 400 fragment. The peak at m/z 365 was not identified, but presumably resulted from a complex rearrangement. Sulfadiazine displayed major fragments at m/z 182 and 183 (labeled b.) which correspond to loss of $C_3H_4N_2$ and $C_3H_3N_2$, respectively. High mass resolution spectra of this peak supported the presence of two components with slightly higher intensity for m/z 183 than m/z 182 (data not shown). Novobiocin displayed fragments at m/z 451 (labeled g.), 433/434, and 408 (labeled f) which resulted from cleavage at the secondary amine where SPI was expected to initiate, with charge retention on the fragment containing the fused ring.

Several peaks in the antibiotic spectra of Figure 19 were assigned to calibrant compounds or impurities. The m/z 101 peak (labeled a.) on the tetracycline spectrum was due to triethylamine vapor leaked into the instrument. The m/z 720 peak labeled C_{60} in the novobiocin and tetracycline spectra was due to the addition of C_{60} to the antibiotic sample prior to analysis. Both triethylamine and C_{60} were used to perform mass calibration and tuning of the instrument. Sulfadiazine displayed a prominent peak at m/z 278 and several lower intensity peaks at higher

masses due to impurities (presumably present in the original compound as purchased) or clustering.

3.3.2 Detection of Antibiotics in Bacterial Biofilms

LDPI-MS was used to detect these antibiotics within intact biofilms without significant interference from any of their other chemical constituents. Figure 20 (top trace) displays LDPI-MS of sulfadiazine on *S. epidermidis* biofilm at 11 mM concentration, prepared by transferring a viable biofilm to an agar plate prepared with this concentration of the antibiotic and allowing the biofilm to equilibrate with the agar plate for one hour. The biofilm sample was then removed from the agar plate, dried overnight, fixed with acetonitrile:water washes, and placed in the load lock. The sample was laser desorbed using $\sim 3 \text{ MW/cm}^2$ power density, postionized, and then detected in reflectron mode. The parent ion of sulfadiazine at m/z 250, its major fragment at m/z 182/183, and the peak at m/z 278 all appeared in the LDPI-MS of the biofilm. No signal above m/z 50 was seen for the LDPI-MS of the biofilm without sulfadiazine (middle trace of Figure 20). Furthermore, no signal at all was seen without postionization of the biofilm with sulfadiazine (bottom trace of Figure 20), indicating that MALDI-like events did not occur here. These results support the argument that of all the neutrals laser desorbed from the biofilm, only sulfadiazine had sufficiently low ionization energy to undergo SPI at 7.87 eV. This selectivity is an important feature of LDPI-MS and will enable spatially resolved analysis of these antibiotics.

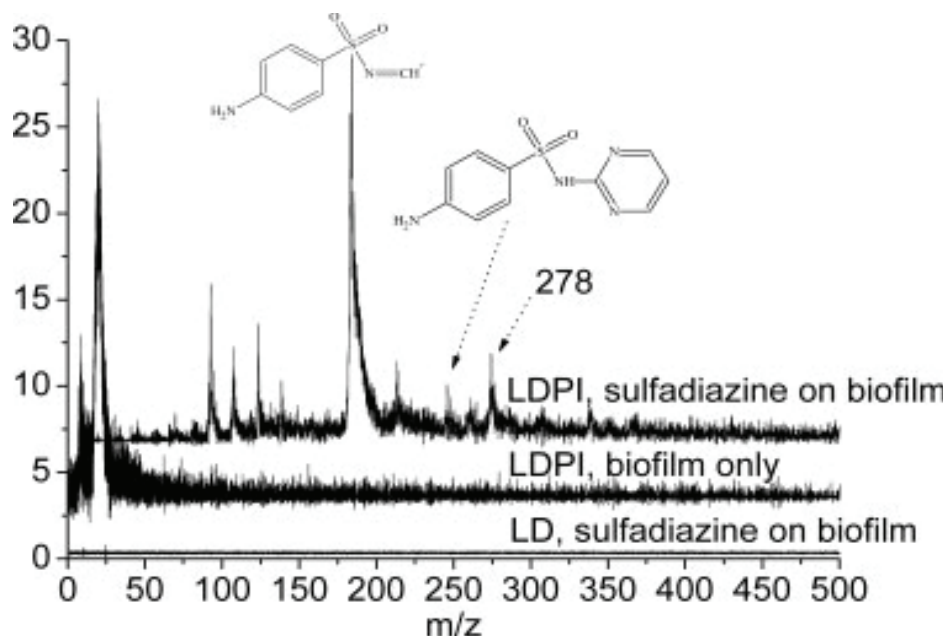


Figure 20: 7.87 eV LDPI-MS of antibiotic doped bacterial biofilms.

LDPI-MS of (top trace) 11 mM sulfadiazine in a *S. epidermidis* colony bacterial biofilm and (middle trace) the biofilms without any added antibiotic. (Bottom trace) laser desorption only MS (without postionization) of sulfadiazine in biofilm.

3.3.3 Bacterial Biofilm Viability Study

Antibiotic detection with biofilms should ideally be performed at inhibitory concentrations for the time of antibiotic exposure in a given trial. Viable *S. epidermidis* biofilms were transferred to agar plates with antibiotics at several concentrations for one hour, and so Figure 21 displays colony viability data under these conditions. The data is expressed as percent viable cells relative to the control. The control colonies averaged 5.8×10^8 total viable cells ($\pm 7\%$) with an average areal density of 3.1×10^8 viable cells/cm². For both the 4 and 14 mM concentrations of tetracycline, about 50% fewer viable cells were counted as compared to the control. Both of these concentrations were above the saturation concentration of tetracycline in aqueous solution, so the actual concentration of antibiotic was likely the same in both cases. Neither the 0.8 or 0.08 mM samples showed any significant inhibition of colony biofilm cell

growth during one hour of treatment. By contrast, the minimal inhibitory concentration of tetracycline for planktonic *S. epidermidis* cells was 0.86 μM .

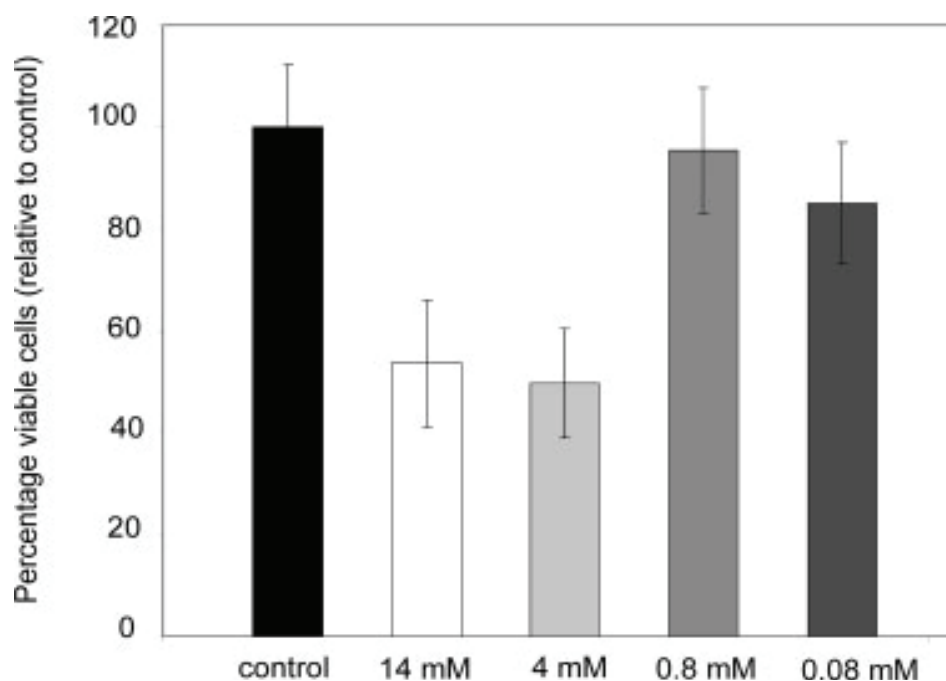


Figure 21: Viability study of *S. epidermidis* with tetracycline.

Percentage of viable cells relative to control for *S. epidermidis* colony biofilms grown for 1 h on tryptic soy agar with 0.08, 0.8, 4, and 14 mM (nominal) concentrations of tetracycline.

Figure 22 (top trace) displays LDPI-MS of a *S. epidermidis* colony biofilm transferred for one hour to an agar plate with 8 μM tetracycline with the laser desorption only spectrum displayed underneath (lower trace). LDPI-MS displayed the same characteristic ions for tetracycline above m/z 300, including the M^+ parent ion at m/z 444, the $[M-OH]^+$ fragment at m/z 427, the $[M-NMe_2]^+$ fragment at m/z 400, and the $[M-OHNMe_2]^+$ fragment at m/z 383. No significant ion signal was observed by laser desorption only from the tetracycline treated biofilm (bottom trace), as was the case for sulfadiazine. LDPI-MS with obvious peaks from tetracycline

were also obtained from biofilms similarly prepared at 14, 4, 0.8 and 0.08 mM tetracycline concentrations (data not shown). The antibiotic concentration in Figure 22 were similar to the concentrations of several other drugs detected by MALDI-MS in tissue (Reyzer and Caprioli, 2007; Stoeckli et al., 2007), indicating that LDPI-MS can reach useful limits of detection at least for this antibiotic. No matrix was added to any of the biofilms analyzed by LDPI-MS.

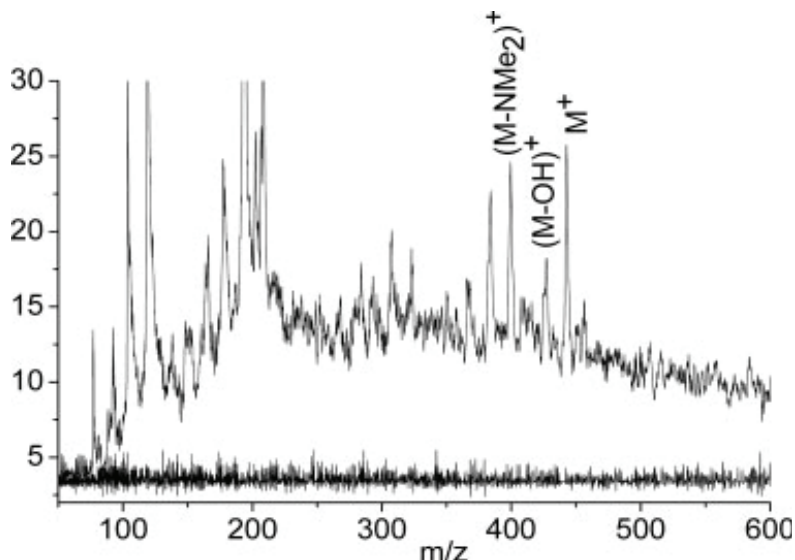


Figure 22: 7.87 eV LDPI-MS of 8 μ M tetracycline in colony biofilm. LDPI-MS (top trace) and laser desorption only (bottom trace, no postionization) of 8 μ M tetracycline in *S. epidermidis* colony biofilms.

LDPI-MS of the 8 μ M tetracycline in biofilm (Figure 22) showed much higher ion signal below m/z 300 than observed for 11 mM sulfadiazine in the biofilm (Figure 20). The more intense low mass signal for this low tetracycline concentration was due to the use of higher laser desorption powers of ~ 11 MW/cm² compared to ~ 3 MW/cm² for sulfadiazine. The higher laser power used at the lower concentration could have enhanced the low mass ion signal by ablation of a larger volume of biofilm per laser shot, generating more neutrals that could be postionized. Increased fragmentation of the antibiotic and biofilm components could have lead to the formation of small species that could be postionized. High power laser desorption of tetracycline

may have formed fragments with ionization energies below the 7.87 eV postionization photon energy while sulfadiazine either did not fragment (at the lower power densities) or the additional fragments it did form (beyond m/z 182/183) did not display ionization energy below 7.87 eV.

3.4 CONCLUSION

Prior work demonstrated that MS imaging of small molecules within intact biofilms is feasible by LDPI-MS (Edirisinghe et al., 2007). LDPI-MS is experimentally just a MALDI-MS experiment with a postionization laser, so most of the same considerations that allow imaging with MALDI-MS also permit imaging with LDPI-MS. Furthermore, LDPI-MS may allow higher sensitivity given its ability to exploit the larger neutral yields from laser desorption (Dreisewerd, 2003). However, perhaps the greater advantage of LDPI-MS with 7.87 eV radiation is its selectivity towards species with low ionization energies. This selectivity can be used to target analytes directly or via their chemical derivatization *in situ* to reduce interferences from the multitude of other compounds present in complex biological media such as bacterial biofilms.

LDPI-MS achieved micromolar LOD in bacterial biofilms without addition of any matrix compound. Therefore, addition of matrix in future experiments should allow an increase in LOD by enhancing neutral desorption yields. Prior studies have shown that some matrix compounds and mixtures can be added in such a fashion as to enhance desorption without increasing ionization yields (Dreisewerd, 2003; Edirisinghe et al., 2006).

**4 TUNABLE POSTIONIZATION OF LASER DESORBED NEUTRALS BY
SYNCHROTRON RADIATION TO DETECT ANTIBIOTICS AND
EXTRACELLULAR MATERIAL IN *STAPHYLOCOCCUS EPIDERMIDIS*
BACTERIAL BIOFILMS**

4.1 INTRODUCTION

Antibiotic resistance may derive from the extracellular polymeric substance, composed of polysaccharides, nucleic acids, and other species produced by the microbes, or from the fortified cell walls of *S. epidermidis* and similar gram positive microbes (Sousa et al., 2009). Studies of biofilm antimicrobial resistance would benefit from new methods in MS imaging that probe the intact biofilm and allow characterization of relevant components of the extracellular environment. Secondary ion mass spectrometry (SIMS) has been applied to biofilms (Tyler et al., 2006) and bacteria (Vaidyanathan et al., 2008; Esquenazi et al., 2009). Other methods in MS imaging also show promise for such analyses (Watrous et al., 2010), including matrix assisted laser desorption ionization MS of bacterial colonies grown on agar (Esquenazi et al., 2009).

Prior work with 7.87 eV VUV photons showed that LDPI-MS is a sensitive analytical tool to selectively probe analytes within intact bacterial biofilms. 7.87 eV LDPI-MS detected and imaged a concentration gradient of rifampicin in a *S. epidermidis* biofilm and several other antibiotics (see Chapter 3) (Akhmetov et al., 2010). Quorum sensing peptides in *Bacillus subtilis* have also been detected by 7.87 eV LDPI-MS (Edirisinghe et al., 2007). The use of 7.87 eV VUV photons in LDPI-MS is straightforward since they are produced by robust, commercially available excimer laser sources (Hanley and Zimmerman, 2009). However, the dearth of intense, pulsed, commercially available VUV sources for higher photon energies necessitates the use of synchrotron radiation for thorough evaluation of the application of SPI-MS to imaging strategies. Prior work has also shown the capability of tunable VUV synchrotron

radiation to detect sputtered neutrals for MS imaging (Takahashi et al., 2009; Zhou et al., 2010).

This chapter demonstrates the use of tunable 8.0 to 12.5 eV photon energies with LDPI-MS to detect antibiotics both neat and doped into drip flow grown biofilms. The photon energy tunability available with synchrotron sources allows for the determination of the most sensitive photon energy for antibiotic detection. This approach also permits characterization of extracellular substances within intact bacterial biofilms, including those formed in response to antibiotic treatment.

4.2 EXPERIMENTAL

This chapter's investigations were performed entirely on the Advanced Light Source's LDPI-MS instrument. Aside from some preliminary tests that ionized vaporous analyte for photoionization efficiency studies, LDPI-MS was conducted on rigid substrates of silicon and ITO for neat and biofilm samples. With the synchrotron, each sample was scanned for direct ionization by laser desorption (LD, no VUV) and synchrotron background (SB, no LD). Relative photon flux curves were obtained from 8.0 to 12.5 eV and used to correct the ion intensity at each photon energy. Data was collected when direct ionization and synchrotron background were not present in the spectrum. For additional instrumental details on LDPI-MS at the Advanced Light Source, see Section: 2.1.4. For additional instrumental details on biofilms grown by drip flow, see Section 2.2.3: Drip Flow Biofilms on ITO and Silicon Wafers for Biofilm Growth.

4.3 RESULTS AND DISCUSSION

4.3.1 Photoionization of Thermally Desorbed Neat Antibiotics.

Figure 23 shows a photoionization efficiency (PIE) curve of thermally desorbed neat antibiotics. This demonstrates the key concepts mentioned in Section: 1.2.2 on SPI. The synchrotron beam performed SPI on desorbed neat antibiotics of trimethoprim (MW: 290 Da), tetracycline (444), and rifampicin (823) to show increases of ion yield. The constant photon flux represents a constant photon intensity (I , from Eq. 1.1), and constant pressure represents a constant density of neutrals (N , from Eq. 1.1). With constant I and N , this result demonstrates higher photon energies increase photon absorption cross section (σ_{spi} , from eq. 1.1). Higher photoabsorption will be the basis of increasing ion yield and sensitivity for studies at photon energies above 7.87 eV.

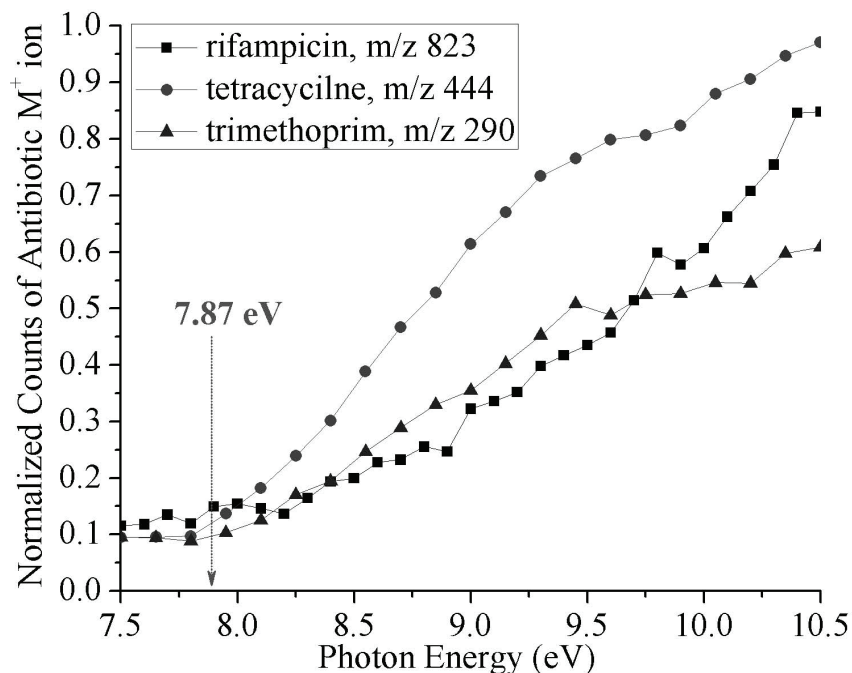


Figure 23: PIE of thermally desorbed neat antibiotics.

PIE of thermally desorbed neat antibiotics: rifampicin (MW: 823), tetracycline (444), trimethoprim (290). Constructed by Dr. Jia Zhou at the Chemical Dynamics Beamline, Lawrence Berkeley National Laboratories.

4.3.2 Detection of Neat Antibiotics.

Figure 24 displays the LDPI spectra of neat rifampicin adsorbed on ITO glass, recorded at VUV photon energies of 8.0, 9.0, 10.5, and 12.5 eV. Each spectrum is a plot of m/z versus ion signal corrected for photon flux variation with photon energy. The parent ion of rifampicin appears at m/z 823 and is observed at all photon energies, albeit at different intensities. All photon energies ≥ 8.0 eV are sensitive to this antibiotic, with the best signal to noise ratio occurring at 10.5 eV. Prior work found that the rifampicin parent ion was a radical cation (Hanley and Zimmerman, 2009). The enhanced ion signal at 9.0 eV vs. 10.5 eV presented in Figure 24 was not reproduced in replicate samples and probably resulted from spot-to-spot fluctuation in laser desorption efficiency.

Figure 24 also displays several fragments of rifampicin including m/z 99, 298, and 791 (indicated by asterisks) which correspond to a methylated piperazine fragment, naphthalene core, and methyl-ether fragment loss, respectively. Another dominant fragment, m/z 84, likely forms via methyl loss from the m/z 99 fragment ion. The m/z 284 fragment also appears to result from rifampicin. Antibiotic fragmentation pathways will be discussed in a separate publication.

Spectral complexity from m/z 100 to 400 increases with increasing photon energy. Ions below m/z 200 are especially predominant for 12.5 eV LDPI-MS due to both increased ionization and fragmentation of parent ions. Ionization of more chemical constituents occurs as the higher photon energies exceeds the ionization energies of a larger group of species. These additional species undergoing ionization at higher photon energies include water, adventitious hydrocarbons adsorbed from vacuum, and possibly neutral fragments of rifampicin that are photodissociated by the desorption laser.

Dissociative photoionization of parent ions also occurs due to excess internal energy imparted by the higher photon energy (Hanley and Zimmerman, 2009; Akhmetov et al., 2010).

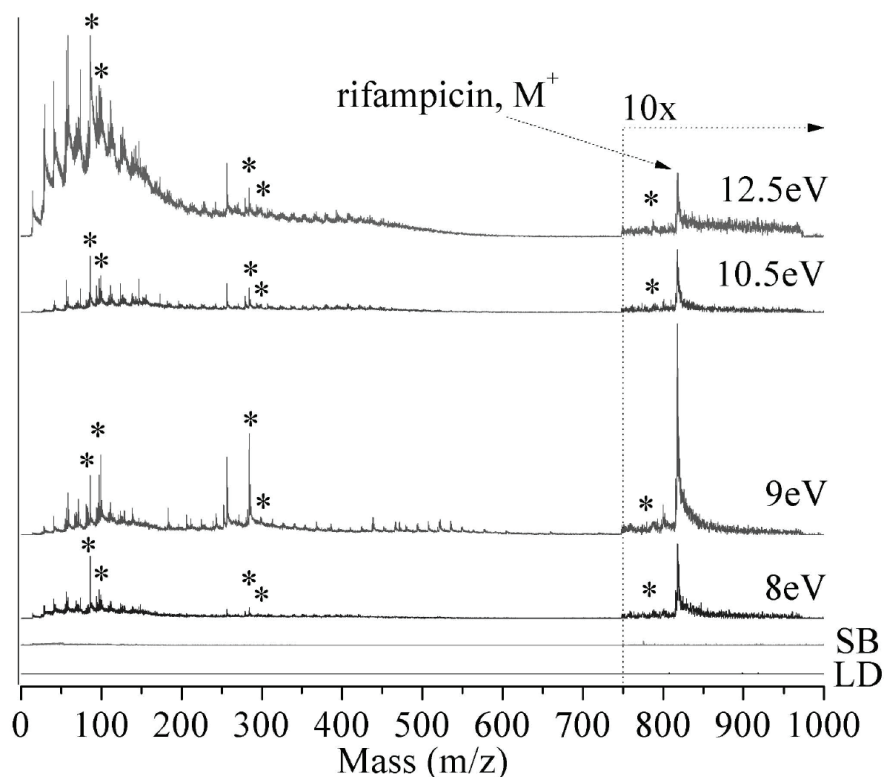


Figure 24: LDPI-MS of neat rifampicin at photon energies 8 – 12.5 eV. LDPI-MS of neat rifampicin at photon energies of 8.0 – 12.5 eV (indicated on each spectrum). Also shown are (LD) direct ionization by laser desorption without vacuum ultraviolet (VUV) radiation and (SB) synchrotron background at 12.5 eV photon energy (no LD). Ion signal is shown after correction for photon flux variation with photon energy. Asterisks indicate known rifampicin fragments. Spectra here and below are artificially offset to avoid peak overlap.

Also shown in Figure 24 are the 12.5 eV synchrotron background (SB) without laser desorption (LD) and LD without any VUV postionization: neither of these control spectra show significant signal contributions. There is a very slight synchrotron

background (SB) signal observed as a result of the beam grazing the sample surface and/or labile species subliming into the path of the synchrotron beam. For this reason, only the highest photon energy synchrotron background is shown, as this contribution is always larger than that observed at the lower photon energies.

Similar results are observed for the LDPI-MS of neat trimethoprim which displays an intact parent cation at m/z 290, as shown in Figure 25. Trimethoprim fragments to form $[M-NH_2]^+$ fragment due to loss of amine at m/z 274 and $[M-CH_3O]^+$ at m/z 259 due to loss of ethanol. Other dominant, but unidentified trimethoprim-derived peaks are observed at m/z 242 and 284. The few peaks observed in the synchrotron background in Figure 25 may indicate an artifact resulting from the synchrotron beam grazing the sample surface, as discussed earlier. Ion formation from VUV radiation grazing the sample surface was previously observed on this instrument when measuring organic surfaces.

Another spectral feature in the trimethoprim LDPI-MS of Figure 25 is an elevated baseline that appears as a step function following each peak in the mass spectra. This baseline step function results from the continuous ionization of slowly desorbing neutrals by the quasi-continuous wave VUV radiation. Shortening the extraction pulse is effective in reducing or eliminating this baseline, albeit at the expense of reduced sensitivity for higher m/z ions. However, care must be taken not to compromise mass resolution when lengthening the extraction pulse to gain sensitivity.

Any VUV radiation incident on metal electrodes in the ion extraction region produces photoelectrons that will be accelerated by electrostatic fields and potentially lead to electron ionization (Gamez et al., 2008). Some of this contribution could arise as

the SB signal discussed earlier, but photoelectron induced electron ionization appears minimal compared to the true photoionization signal.

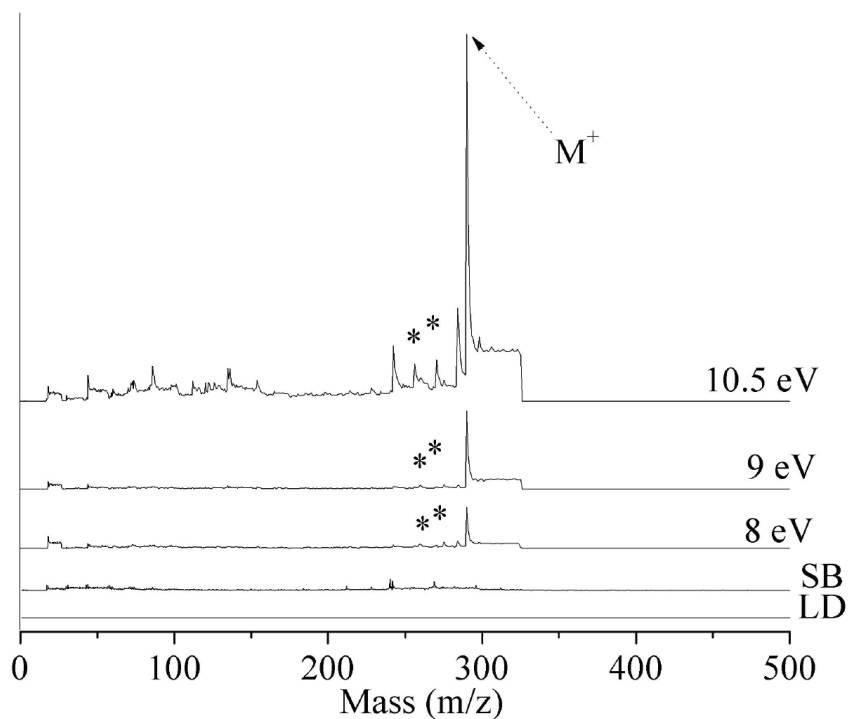


Figure 25: LDPI-MS of neat trimethoprim at photon energies 8 – 12.5 eV. 8.0 – 10.5 eV LDPI-MS of neat trimethoprim. Includes (LD) direct ionization by laser desorption and (SB) synchrotron background at 10.5 eV. Known trimethoprim fragments indicated by asterisks.

4.3.3 Analysis of Biofilms Treated with Rifampicin Antibiotic.

Figure 26 displays 8.0 – 12.5 eV LDPI-MS of drip flow biofilms grown on ITO glass and doped with 120 μ M rifampicin. The parent ion of rifampicin appears at m/z 823 for 9.0, 10.5, and 12.5 eV photon energies, but is buried in the baseline at 8.0 eV. Lower intensity fragments observed in neat rifampicin, such as m/z 791, are buried in the baseline but the m/z 84 and 284 rifampicin fragment peaks remain visible. These mass ions are also observed from 7.87 eV LDPI-MS of biofilms and are thought to result from

the desorption and ionization of a variety of low mass species, shown in Chapter 3 (Edirisinghe et al., 2007; Hanley and Zimmerman, 2009; Akhmetov et al., 2010). The higher peak intensities below m/z 200 at 12.5 eV photon energies is attributed to a loss of selective ionization and fragmentation, as discussed above for neat rifampicin.

A novel observation is that the rifampicin-treated biofilm spectra shown in Figure 26 display a polymeric series of peaks from $\sim m/z$ 1000 to 1800, with a consistent 74 Da mass separation. These polymeric peaks are observed at all photon energies, however the 10.5 eV LDPI-MS displays the best signal to noise ratio. The m/z values of the polymeric peaks do not vary with photon energy, and while the low and high mass limits vary somewhat, they appear near m/z 1000 and 1800, respectively. No definitive identification of these polymeric peaks can be made with the current instrumentation, which like many MS imaging instruments, lacks exact mass and tandem mass spectrometric capabilities. However, by examining the literature and based upon the peak spacing of ~ 74 Da that is always observed in the polymeric distribution, a tentative assignment can be made to peptidoglycans from the antibiotic-degraded cell wall.

The cell wall is made up of an approximately 50 nm thick peptidoglycan layer alternating units of *N*-acetylmuramic acid and *N*-acetylglucosamine linked by β -1,4-glycosidic bonds forming these glycan chains and crossed-linked by pentaglycine (Walsh, 2003). It is proposed that rifampicin lyses the cells leading to the release of peptidoglycan cell wall fragments with multiple strings of pentaglycine, which gives rise to the m/z 1000 – 1800 polymeric series of 5 to 15 peaks separated by ~ 74 Da observed in this work. The primary mode of action of rifampicin is inhibition of DNA and RNA synthesis (Walsh, 2003). However, rifampicin has also been shown to effectively

penetrate the thick extracellular polymeric substance that *S. epidermidis* microbes exude to anchor the biofilm (Zheng and Stewart, 2002). Furthermore, rifampicin deforms and/or lyses *S. epidermidis* cells in biofilms (Richards et al., 1989; Liang et al., 2006). Both processes are expected to result from cell wall degradation.

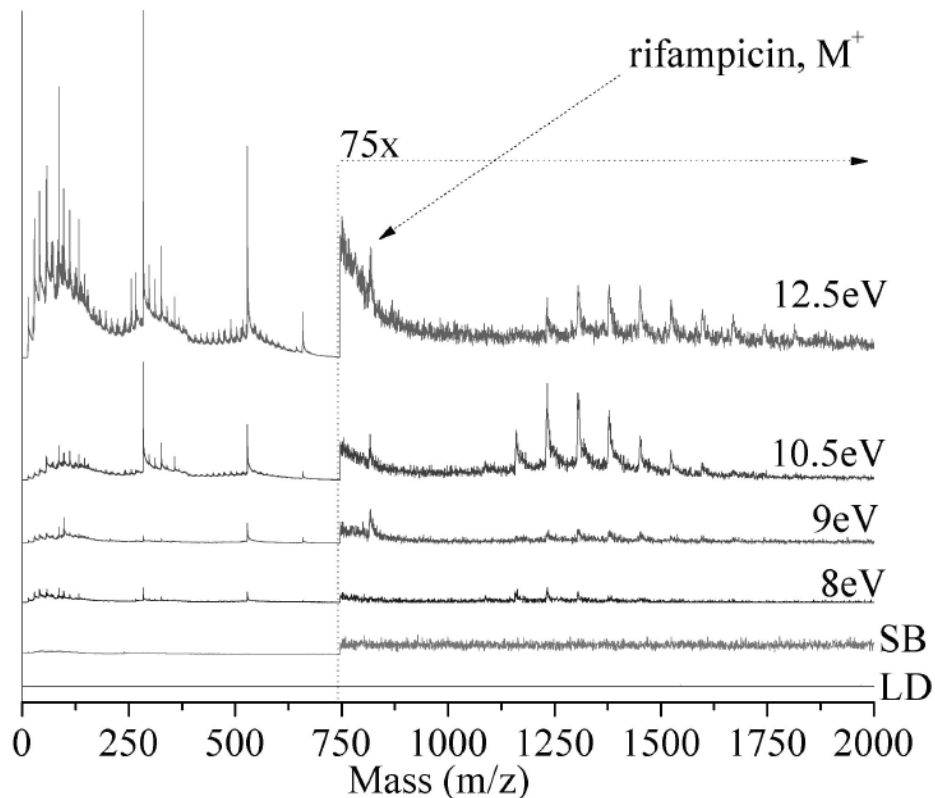


Figure 26: LDPI-MS of rifampicin doped biofilm at photon energies 8 – 12.5 eV. 8.0 – 12.5 eV LDPI-MS of 120 μ M rifampicin-treated biofilm. Includes (LD) direct ionization by laser desorption and (SB) synchrotron background at 12.5 eV.

Lysostaphin is an antimicrobial known to cleave the peptidoglycan crosslinking pentaglycine bridges of *Staphylococcus aureus*, thereby hydrolyzing the cell wall and lysing the bacteria (Kumar, 2008). Rifampicin and lysostaphin displayed a similar ability to deform and/or lyse *S. epiderimidis* biofilms (Liang et al., 2006). Peptidoglycan

fragments can be formed by autolysis or lysis of bacteria brought upon by specific antimicrobials (Cloud-Hansen et al., 2007). It follows that rifampicin might also cleave the pentaglycine bridges of the peptidoglycan cell wall of *S. epidermidis*, leading to the polymeric peak distribution observed here. The acetonitrile solvent used to dissolve the antibiotics can also contribute to cell lysis, but any such effect would have to be synergistic with that of rifampicin to play a role here (Rais et al., 2008).

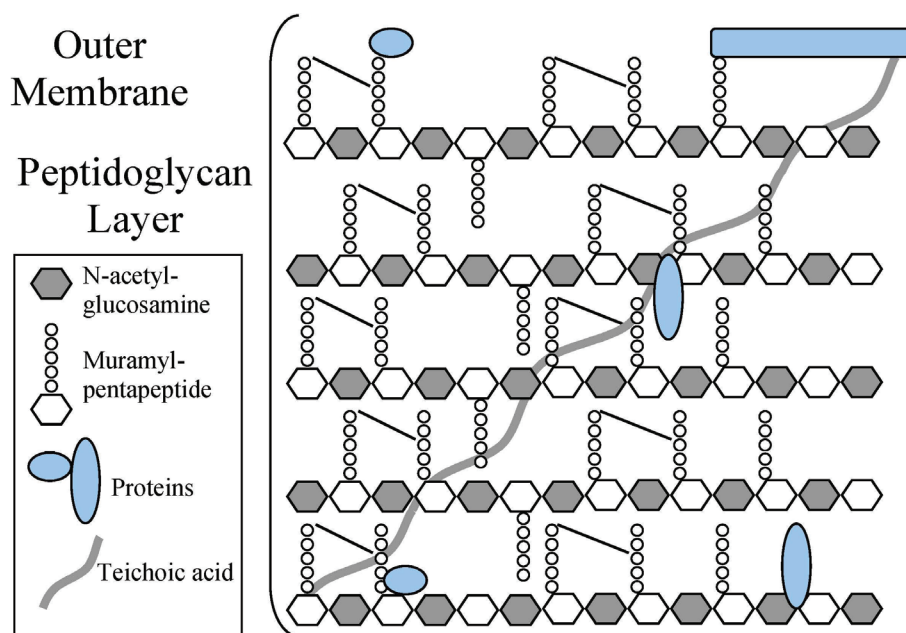


Figure 27: Peptidoglycan layer in the outer membrane of Gram-positive bacteria. Adapted from Walsh, 2004.

Several other assignments for the polymeric peak distribution are considered and excluded here. The polymeric series does not appear to result from adducts with rifampicin. Neither teichoic acid nor polysaccharides possess the required string of adjacent monomers to produce the ~ 74 Da mass separation between peaks (Swoboda et al., 2010). Inorganic species that could induce such a mass separation (Tong et al., 1999) are also ruled out. First, the peak widths do not increase in width as would be expected

with the addition of multiple KCl adducts due to the ^{35}Cl and ^{37}Cl isotopes. Second, adduction with $\text{Si}(\text{CH}_3)_2\text{O}$ from silicone in laboratory containers is ruled out by the appearance of the polymeric series only in the presence of rifampicin. Nevertheless, the assignment of the polymeric distribution to peptidoglycans is tentative and further work is required to characterize the observed species by other methods. Two unidentified peaks at m/z 521 and 662 also appear in Figure 26, and discussed in the next Section.

Synchrotron background contribution becomes more apparent at 12.5 eV photon energies in the rifampicin treated biofilm spectrum of Figure 26, especially compared to that of the neat rifampicin spectrum of Figure 24. The greater noise level in the synchrotron background in the former is likely due to the photoionization of volatile species subliming from the biofilm. Laser desorption without any VUV again showed no significant ionization.

4.3.4 LDPI-MS Comparison of Biofilms with and without Antibiotic Treatment.

Figure 28 displays LDPI-MS of a biofilm treated with 1.0 mM trimethoprim recorded at VUV photon energies of 8.0 and 10.5 eV. This trimethoprim-treated biofilm shows an eightfold enhancement of parent ion at m/z 290 when the photon energy is increased from 8.0 to 10.5 eV. Identifiable trimethoprim fragments observed from the biofilm include m/z 259 and 275, corresponding to losses of methylamide and methyl groups, respectively. The step-like feature in the spectrum immediately after the parent is a result of a pulsed extraction. Note the breadth of this step is 10 μsec in width as is the extraction.

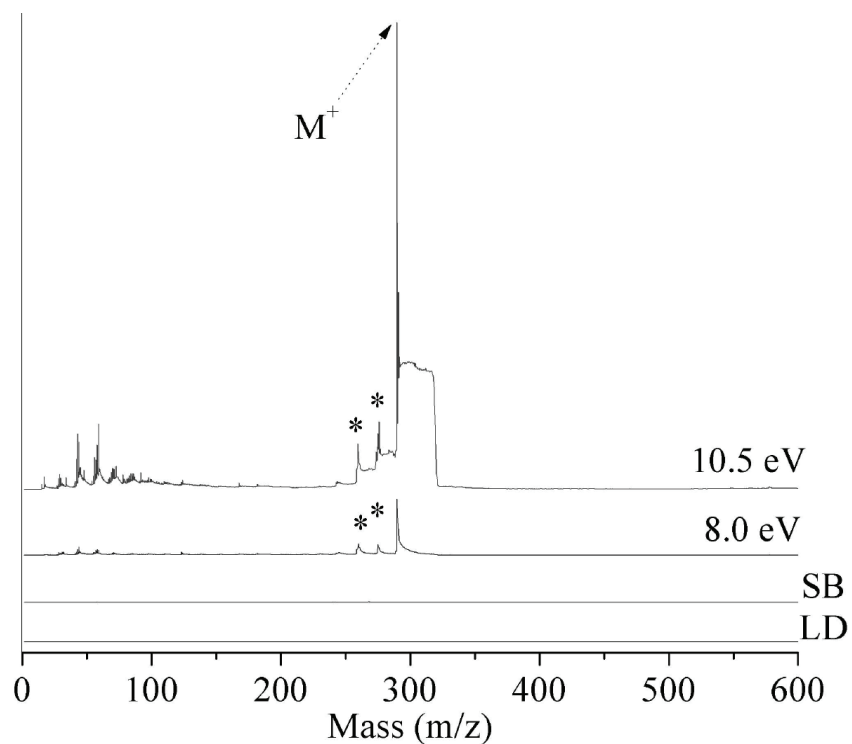


Figure 28: LDPI-MS of trimethoprim doped biofilm at photon energies 8 and 10.5 eV. 8.0 and 10.5 eV LDPI-MS of 1.0 mM trimethoprim-treated biofilm. Includes direct ionization by laser desorption (LD) and synchrotron background at 10.5 eV (SB). Asterisks indicate known fragments.

Figure 29 compares the 10.5 eV LDPI-MS of a trimethoprim-treated biofilm, a rifampicin-treated biofilm, and a control biofilm prepared without any antibiotic treatment. Neither the control biofilm without any antibiotic nor the trimethoprim-treated biofilm displayed the polymeric series of peaks observed above m/z 1000 in the presence of rifampicin (see prior section of chapter). Trimethoprim's antibiotic activity results from its ability to inhibit metabolism of folic acid, which leads to disruption of DNA replication and cessation of cell growth (Walsh, 2003). Thus, the release of peptidoglycans postulated above to explain the rifampicin-induced polymeric peak distribution is not expected for trimethoprim.

Two unidentified peaks at m/z 521 and 662 appear in Figures 26 and 29 only in the presence of rifampicin in the biofilm, and these peaks are visible at all photon energies from 8 to 12.5 eV. However, these two peaks are not seen either in the trimethoprim-treated biofilm or the control biofilm at any photon energy. The prominence of these peaks in the presence of rifampicin implies they represent a specific induced response by the biofilm to rifampicin.

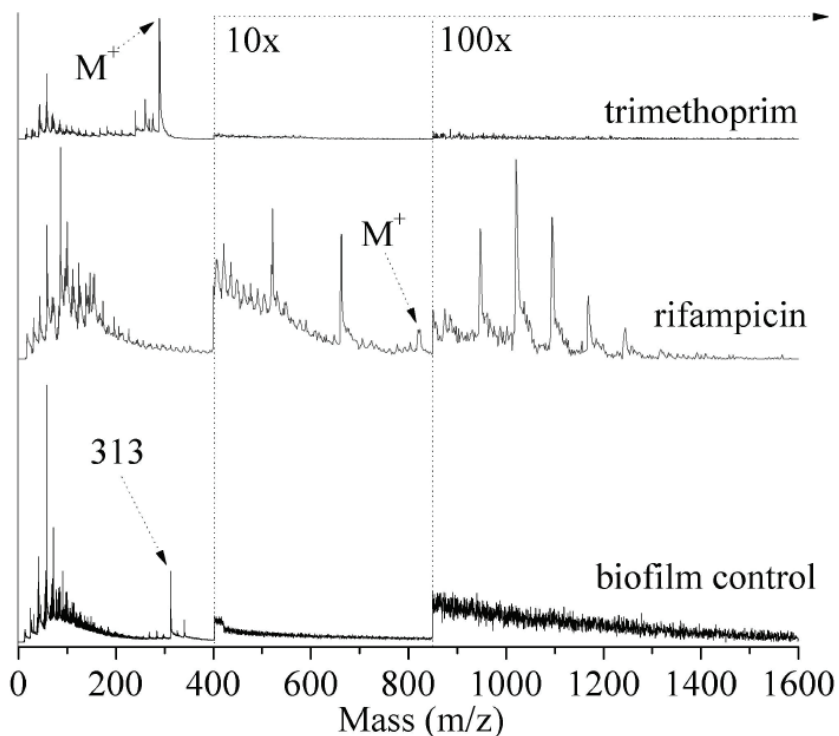


Figure 29: Comparison of biofilm control and antibiotic doped biofilm. 10.5 eV LDPI-MS of 1.0 mM trimethoprim-treated biofilm, 120 μ M rifampicin-treated biofilm, and biofilm control prepared without any antibiotic treatment.

The 10.5 eV LDPI-MS of the control biofilm shown in Figure 30 (bottom) displays the presence of unidentified cellular material with a dominant peak at m/z 313. Figure 30 displays 8.0 – 12.5 eV LDPI-MS of the biofilm control prepared without any antibiotic treatment on ITO glass. The m/z 313 peak, the adjacent peak at m/z 340, and

several others are observed even at 9.0 eV (see inset of Figure 30) and could derive from fragments of phospholipids (Goodacre et al., 1999). Increasing the photon energy to 10.5 and 12.5 eV leads to an increase in the intensity of peaks in this region, some potentially due to the detection of additional, as yet unidentified species. These peaks are not visible in either of the antibiotic doped biofilm spectra.

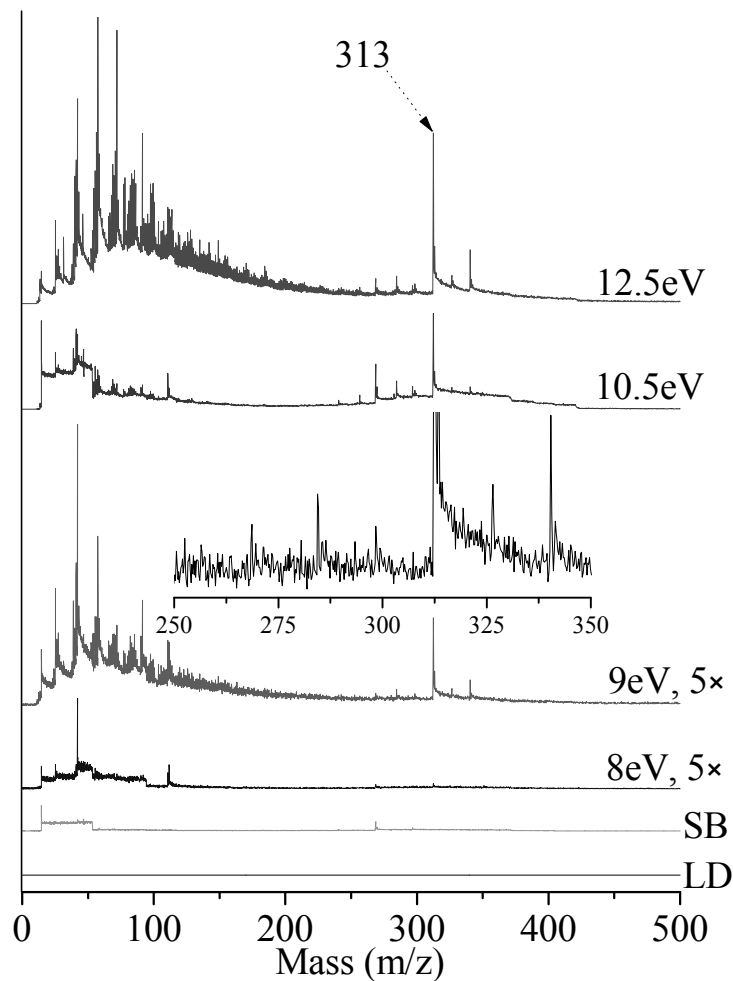


Figure 30: LDPI-MS of neat biofilm at photon energies 8 – 12.5 eV. 8.0 – 12.5 eV LDPI-MS of control doped drip flow biofilm (no antibiotic). Includes direct ionization by laser desorption (LD, no VUV) and (SB) synchrotron background at 12.5 eV (no LD). Inset displays expanded m/z 250 – 350 region of 9.0 eV LDPI-MS, with m/z 313 peak truncated.

Abundant peaks are also observed in the biofilm control spectra below m/z 200, and these are most pronounced with 12.5 eV LDPI-MS. Similar low mass peak distributions are observed in neat rifampicin, rifampicin doped biofilm, and the trimethoprim doped biofilm. At 12.5 eV photon energies, ≥ 3.5 eV of excess energy is available to the parent ion to enhance dissociation. Thus, the increased number of peaks below m/z 200 can be attributed to enhanced parent ion dissociation as well as detection of intact high ionization energy species.

4.3.5 Laser Desorption Effects.

All spectra presented here are the sum of 143,000 individual mass spectra recorded from a single ~ 300 μm diameter spot on the sample. Concern regarding the potential exhaustion of analyte signal during such extended laser desorption led to collection of data presented in Figure 31, which displays the signal decay of two important peaks from the 10.5 eV LDPI-MS of a rifampicin-treated biofilm. The rifampicin parent peak (m/z 823) signal decays to $1/e$ of its original value within 8200 laser shots or ~ 3.3 seconds. An abundant polymeric series peak at m/z 1389 is also monitored in Figure 31 and displays a decay that is 75% longer than that of m/z 823. Approximately half of the total ion signal is accumulated within 3.3 seconds and $\sim 90\%$ of all ion signal was collected within 22 seconds. However, running the data collection for the full ~ 57 seconds slightly improves the signal to noise and compensates for different decay times between different ions. Examination of the spectra accumulated on a single spot for various time periods does not show any dramatic changes in the relative peak intensities.

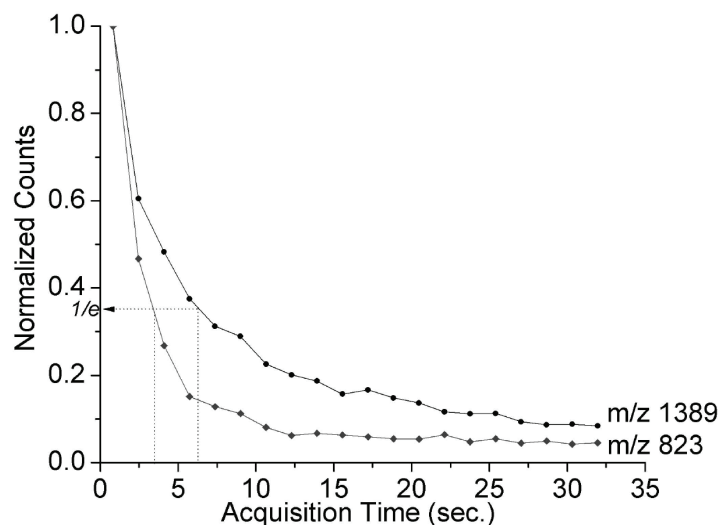


Figure 31: Decay curve of rifampicin LDPI-MS signal intensity.

Normalized ion signal decay curves from rifampicin doped biofilm with 10.5 eV LDPI-MS for (top curve) the polymeric peak which appears at m/z 1389 and (bottom curve) the rifampicin parent ion peak which appears at m/z 823.

A complete study of sensitivity was not performed, but a rough estimate of limit of detection can be made. 50 μL of rifampicin doped onto the biofilm at 120 μM concentration deposits 6 nmoles of analyte onto the 1 cm^2 ITO substrate. Under the current parameters a fixed desorption laser spot of 300 μm leaves a maximum of ~ 4 pmol of analyte available for analysis. If it is assumed that the analyte in this area is exhausted during an analysis and 55% of ion accumulation is reached at $1/e$ (see above), then it is possible to detect 2 pmol of analyte at $1/e$.

The relatively defocused, extended laser desorption utilized here is in contrast to the more focused laser desorption previously reported for 7.87 eV LDPI-MS of biofilms (Akhmetov et al., 2010). In the latter, the desorption laser was focused into a ~ 20 μm diameter spot on the sample and exhausted the analyte in $<10^2$ laser shots. Attempts in this study to increase the desorption efficiency by increasing the laser pulse energy only

form more pyrolysis type peaks in the mass spectra, as typified by ion signal appearing at nearly every mass unit up to $\sim m/z$ 500 (data not shown).

4.4 CONCLUSIONS

It has been shown that tunable VUV radiation can postionize laser desorbed neutrals of antibiotics and extracellular material from within intact bacterial biofilms. Much prior work has focused on the selectivity to species with low ionization energies that is afforded by SPI with 7.87 eV photons, also shown in Chapter 3 (Edirisinghe et al., 2007; Hanley and Zimmerman, 2009; Akhmetov et al., 2010), but the current work shows that higher photon energies dramatically improve sensitivity. Within the range of 8.0 – 12.5 eV, photon energies of 10.5 eV appear to provide the optimal balance between improved sensitivity and minimal fragmentation, at least for the biofilm-antibiotic combinations probed here. Furthermore, while 12.5 eV photons produce significant parent ion signal, signal for fragments and other low mass ions are also enhanced at this relatively high photon energy.

SIMS and MALDI-MS have been applied to image colonies of microbes (Tyler et al., 2006; Esquenazi et al., 2009), and further studies are needed to compare LDPI-MS to those methods. Nevertheless, the relatively low emitted ion/neutral ratios in SIMS and MALDI-MS (Akhmetov et al., 2010) argue for the use of postionization strategies to improve sensitivity and subsequent quantification (Adam and Zimmerman, 2007). SPI with VUV radiation is one of several postionization strategies under investigation for MS imaging (Kriegeskotte et al., 2009; Willingham et al., 2009; Nemes et al., 2010; Galhena et al., 2010). LDPI-MS has been shown to be competitive with other

desorption/ionization methods (Siegal et al., 1999), allowing detection of even high mass peptides (Marksteiner et al., 2009). The results presented here indicate that VUV postionization can contribute new and useful analytical information in MS imaging. This conclusion seems especially valid when taking into account the shortcomings of the current LDPI-MS configuration necessitated by the use of synchrotron radiation. These shortcomings include relatively low VUV intensities and a mismatched duty cycle resulting from combining pulsed desorption with continuous wave VUV radiation for SPI. However, new, higher photon energy pulsed VUV sources are being developed that should overcome these shortcomings in the future (Heinbuch et al., 2005; Hanley and Zimmerman, 2009; Akhmetov et al., 2010; Chen et al., 2009).

Another point to consider in LDPI-MS is that no matrix addition or other pretreatment is required to facilitate successful analysis. However, the current size of the desorption beam is not ideal and may contribute to thermal desorption. Nevertheless, even with the large number of laser shots on the same sample spot used here, no sample degradation is apparent once the desorption laser power is optimized. However, work with 7.87 eV LDPI-MS (Hanley and Zimmerman, 2009; Akhmetov et al., 2010), shown in Chapter 3, indicates that higher pulse energies focused into smaller spots might prove advantageous by inducing a desorption event closer to that known to occur in matrix-assisted laser desorption ionization (Knochenmuss et al., 2010). Future improvements in focusing capabilities of the laser desorption apparatus at the synchrotron and rastering the sample stage for MS imaging may provide a capability comparable to the laboratory VUV sources. Furthermore, work on infrared laser desorption coupled with postionization of animal tissue (Nemes et al., 2010) and femtosecond ablation of biofilms

(Milasinovic et al., 2010) imply that either matrix addition or other laser desorption schemes should be investigated to complement the techniques described here.

Several peaks are observed in the biofilm mass spectra presented here that remain unidentified, but their detection shows great potential for new discovery (Esquenazi et al., 2009). The polymeric peaks tentatively assigned as peptidoglycan fragments can function as signaling molecules in cell–cell communication (Cloud-Hansen et al., 2007), as virulence factors (Cloud-Hansen et al., 2007), and can aid in biofilm formation (Shank and Kolter et al., 2009). This potential ability to detect peptidoglycans within intact bacterial biofilms by LDPI-MS would be a useful new strategy for probing intercellular communication and interspecies interactions within biofilms.

**5 COMPARING VACUUM AND EXTREME ULTRAVIOLET RADIATION FOR
POSTIONIZATION OF LASER DESORBED NEUTRALS FROM BACTERIAL
BIOFILMS AND ORGANIC FULLERENES**

5.1 INTRODUCTION

Vacuum ultraviolet SPI of laser or ion desorbed neutrals has demonstrated sensitive detection and the capability for mass spectrometric imaging of atomic and molecular analytes (Hanley and Zimmerman, 2009; Akhmetov et al., 2010; Takahashi et al., 2009; Zhou et al., 2010). LDPI-MS of biofilms showed improved sensitivity above 8 eV photon energy with optimal signal to noise at 10.5 eV, given constant photon flux, as shown in Chapter 4. By contrast, multiple photon ionization of fullerenes and organic compounds showed increased spectral complexity (Wurz and Lykke, 1992; Pallix et al., 1989) with the absorption of many photons imparting excess energy and causing an inability to mitigate channels of dissociation and ionization (Hanley and Zimmerman, 2009). Prior researchers argue that extreme ultraviolet (EUV) radiation near 26 eV may reduce fragmentation for SPI of van der Waals and H-bonded clusters (Dong et al., 2006; Heinbuch et al., 2006; Dong et al., 2006b, Heinbuch et al., 2007) with spectra appearing similar to those obtained at 10.5 eV (Dong et al., 2009). Yet, considerable molecular fragmentation of small molecules was present in these investigations (Dong et al., 2006; Heinbuch et al., 2006; Dong et al., 2006b). The role of protonated clusters in these experiments to enhance ionization, reduce fragmentation, or facilitate cooling is unclear (Heinbuch et al., 2007). LDPI-MS data was collected here to compare postionization by VUV and EUV radiation. Two different thin film samples were examined: a pure fullerene derivative and a bacterial biofilm with dissolved antibiotic rifampicin.

5.2 EXPERIMENTAL

Investigations in this chapter were performed on the same ALS instrument as used in Chapter 4. Experiments investigated drip flow biofilms grown on rigid substrates, but on ITO

only. Refer to Figure 12 and Section: 2.1.4, for instrumental details. For details on biofilm growth, refer to Section: 2.2.3.

5.3 RESULTS AND DISCUSSION

5.3.1 EUV LDPI-MS of Neat Organic Samples.

LDPI-MS of neat [6.6] diphenyl C₆₂ bis(butyric acid methyl ester), referred to here as C₆₂, are displayed in Figure 32, using both VUV and EUV SPI. The parent ion peak (M⁺) at m/z 1100 was clearly observed at all six photon energies in the VUV and EUV. Three known fragments included m/z 190, 720, and 910, which correspond to the loss of one or two of the 190 Da side chains to the 720 Da C₆₀ core, as well as the core itself (chemical structure shown in Figure 33). Fragmentation of the ligand becomes more apparent at higher photon energies as the abundance of peaks from m/z 57 to 175 increased with respect to m/z 190. Prominent peaks at m/z 648 and 660 were observed at all photon energies, including at 7.87 and 8.5 eV (data not shown), indicating they are probably impurities of C₆₂. Mass resolution was ~1100 at m/z 720 (C₆₀) in the VUV and limited by the temporal energy distribution of ion extraction through a continuous source. Neither direct ionization by laser desorption (LD, no VUV) nor synchrotron background signal (SB, no LD) were observed. For comparison, Figure 34 provides 7.87 eV LDPI-MS spectra of neat C₆₂ performed at UIC on second generation instrumentation.

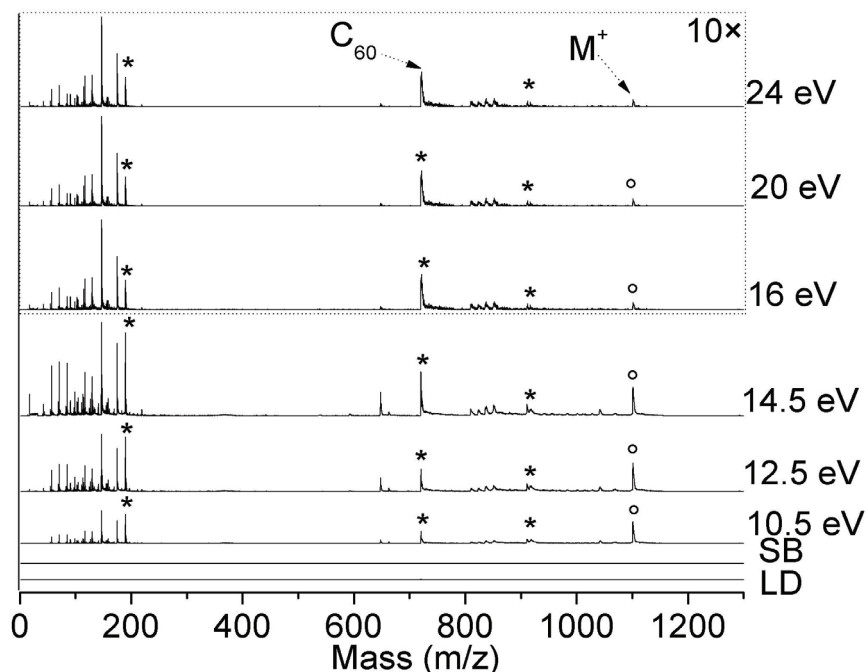


Figure 32: EUV LDPI-MS of fullerene.

LDPI-MS with VUV (<15 eV) as well as EUV photon energies (>15 eV) photon energies of neat C_{60} displaying parent ion (M^+). Asterisks indicate known fragments at m/z 190, 720, and 910, and circles indicate M^+ . EUV spectra were scaled by 10 \times . Synchrotron background (SB) was recorded at 20 eV.

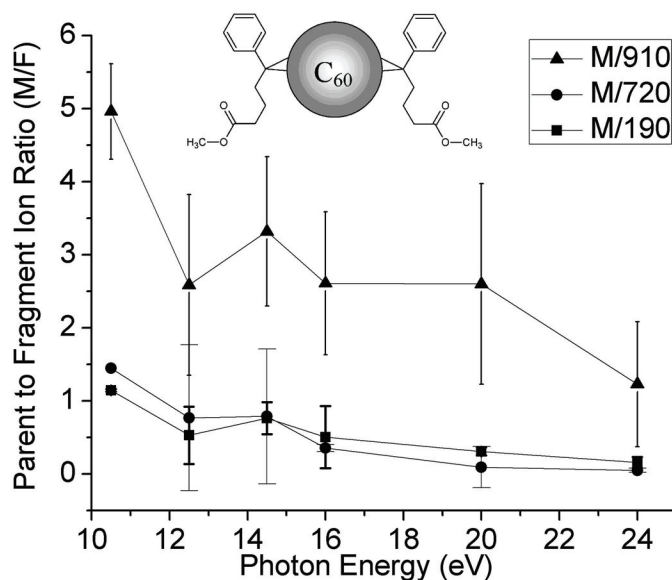


Figure 33: Parent to fragment signal profile by EUV LDPI-MS of neat fullerene.

Parent to fragment ion ratios (M/F) for known C_{60} fragments at m/z 190 ($C_{12}H_{24}O_2$), 720 (C_{60}), and 910 ($C_{60} + 190$).

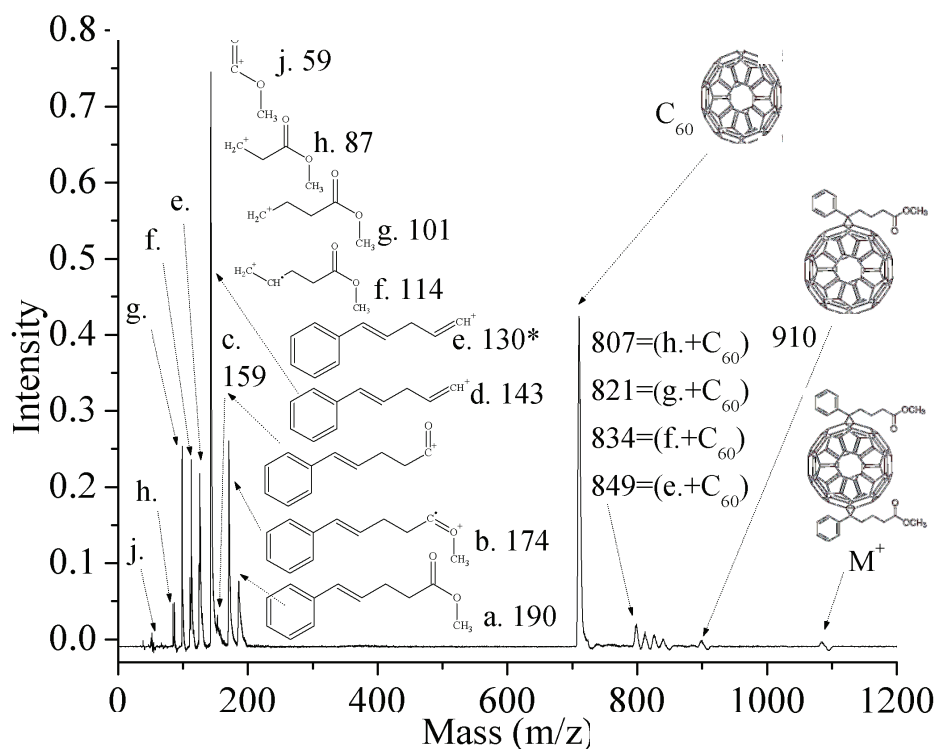


Figure 34: 7.87 eV LDPI-MS (UIC) of neat C_{62} . Major C_{62} peaks include: m/z 1100 $[M]^+$, 910 $[M-L]^+$, 720, C_{60} $[M-2L]^+$, and organic ligand at 190, a., $[L]^+$. Peaks b. through j. are listed above as ligand fragments. Peaks 807, 821, 834, and 849 are listed above as C_{60} combined various with ligand fragments.

Parent to fragment ion ratios (M/F) for m/z 190, 720, and 910 for the data from Figure 32 and another data set are shown in Figure 33. All M/F ratios decreased as the photon energy increased. From 10.5 to 24 eV, all three M/F values reduce to $\sim 33\%$. The relative abundance of m/z 910 was about 3 times less than either m/z 190 or 720 at most photon energies.

5.3.2 EUV LDPI-MS of Doped Bacterial Biofilms.

Rifampicin was doped at a concentration of 120 μM into a bacterial biofilm and measured by EUV LDPI-MS. Figure 35 shows a comparison of the result to similar spectra recorded at VUV (8.0 to 12.5 eV) photon energies (shown in Chapter 4). The rifampicin parent

ion at m/z 823 was barely observable above the noise in the EUV spectra, while it was readily observed in prior VUV spectra. Fragment ions at m/z 84, 284, 510, 524, 641, and 655 (indicated by asterisks) were observed at all three EUV photon energies, as previously identified by VUV LDPI-MS. Mass resolution was between 200 and 400 at major rifampicin fragment peaks.

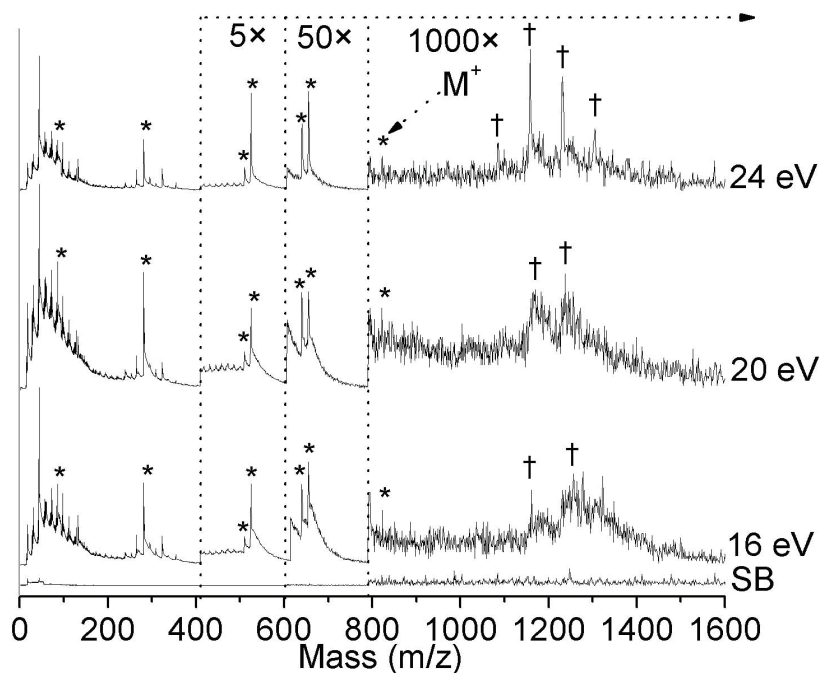


Figure 35: EUV LDPI-MS of rifampicin doped biofilm grown on ITO slide.

LDPI-MS with EUV radiation (16, 20, and 24 eV) of 120 μM concentration of rifampicin doped biofilm. Synchrotron background (SB) was recorded at 24 eV. Rifampicin fragment ions are denoted by asterisks, while polymeric peaks are indicated by crosses.

Peaks observed from m/z 1000 - 1400 derived from the biofilm response to rifampicin were also observed by both EUV and VUV LDPI-MS, as previously discussed in Chapter 4. Increasing the photon energy from 20 to 24 eV enhanced the signal to noise ratio for these peaks. Mass resolution ranged from 100 to 300 at m/z 1157 with the best resolved peaks at 24 eV.

Table 1 shows parent to fragment ion ratios (M/F) for LDPI-MS of rifampicin doped biofilm at known antibiotic fragments m/z 84, 284, and 655 at 10.5 and 20 eV photon energies. Sensitivity decreases rapidly above m/z 800 at 20 eV and is reflected in the M/F values. Table 1

shows the abundance of fragments increased 10 - 200 times from 10.5 to 20 eV. Yet, fragments m/z 84 and 284 increased and remain prominent at 20 eV. Studies by Nuutinen suggest this may result due to stabilization by a piperazine group, represented in these two rifampicin fragments, and dissociation from its methyl group (Nuutinen et al., 2001). Similar VUV work with neat rifampicin observed the prominence of fragments containing methylated piperazine (discussed in Chapter 4).

M/F	10.5 eV		20 eV	
	\bar{x}	σ	\bar{x}	σ
M/84	0.028	0.009	0.0011	0.0006
M/284	0.22	0.18	0.0012	0.0007
M/655	0.31	0.24	0.030	0.02

Table 1: Values of rifampicin parent to fragment ion ratios (M/F) for LDPI-MS of rifampicin doped biofilm at 10.5 and 20 eV.

Parent is compared to fragments: m/z 84, 284, and 655.

5.4 CONCLUSION

SPI with EUV radiation was effective for the two organic/biological systems examined here, but did induce more fragmentation compared with VUV radiation. However, fragmentation is sometimes an unavoidable consequence of the laser desorption process, and addition of matrix compounds or other methods for cooling and stabilizing the desorbed species prior to postionization might mitigate this effect. Further work is clearly required to explore whether the enhanced fragmentation observed here with EUV radiation occurs in other examples of laser desorption and if any such enhancement is offset by the overall increase in ionization efficiency for EUV vs. VUV radiation.

**6 MS IMAGING OF ANTIBIOTICS DISTRIBUTION AND UPTAKE WITHIN
BACTERIAL BIOFILMS BY 7.87 EV LASER DESORPTION POSTIONIZATION**

6.1 INTRODUCTION

MS imaging techniques can map the covariance of multiple chemical parameters critical to these biofilm recalcitrance hypotheses. These chemical parameters include metabolites and metabolic enzymes associated with varying nutrient levels as well as small secreted molecules involved in metabolite exchange. Understanding if and how these hypotheses contribute to biofilm antimicrobial tolerance is fundamental to controlling unwanted biofilms.

This chapter describes the development of LDPI-MS imaging of the distribution of antibiotics within intact *S. epidermidis* bacterial biofilms. 7.87 eV LDPI-MS imaging of antibiotics in biofilms is compared with and without the addition of a standard matrix used in MALDI-MS. Depth profiling is also demonstrated by imaging a biofilm cross section. Overall, these results show that LDPI-MS coupled with other MS imaging capabilities can characterize chemical distributions within intact biofilms.

6.2 EXPERIMENTAL

Most of the spectra presented here were collected using an ion optical design for the second generation LDPI-MS instrument at UIC. Under this design, ions were extracted along a serpentine path to the ToF analyzer which allowed complete discrimination between postionized neutrals which form a few mm above the sample and directly desorbed ions (Moore et al., 2010). Refer to Chapter 2, Sections: 2.1.2 and 2.1.4 for more instrumental details as well as Sections: 2.1.2.1, 2.1.2.2, and 2.1.5 for details on data collection.

However, the limit of detection data was collected after recent modifications to the instrument improved its sensitivity (the details of which are not otherwise included in this thesis). These modifications included the addition of a bipolar MCP detector (Photonis USA,

Sturbridge, MA, USA) and ion optics that improved ion extraction by collecting an ion packet of wider energetic and spatial distribution. MS imaging was accomplished using a vacuum compatible translation stage (Micos USA LLC, Irvine, CA). Optical images were taken with a digital camera (Nikon D300, Nikon Corporation, Japan) equipped with a microscope lens (Nikon ED, AF Micro Nikkor, 200 mm, 1:4D). Refer to Chapter 2, Section: 2.1.4 for SEM details.

Bacterial biofilms were sectioned on a cryomicrotome according to methods established for optical microscopy (Yu et al., 1994). Biofilms were grown on polycarbonate membranes as described in previous chapters, then placed on dry ice while optimal cutting temperature (OCT, Sakura Finetek USA Inc., Torrance, CA, USA) compound was applied on top to embed the biofilm. Details of these applications are explained in Chapter 2, Section: 2.2.4. Other detail regarding biofilm growth by membrane or drip flow can be found in Chapter 2, Sections: 2.2.2 and 2.2.3.

The matrix compound α -cyano-4-hydroxycinnamic acid (CHCA, Sigma-Aldrich) was applied to biofilm samples by either airbrush or nano spotter. Two to three coats were sufficient for these studies with ~30 s of drying between coats. Details of these applications are explained in Chapter 2, Section: 2.2.6.

6.3 RESULTS AND DISCUSSION

6.3.1 Determination of Parent Ions as Radical Cations.

LDPI-MS with 7.87 eV photons verified that the parent ions for several antibiotics were radical cations, as shown in Figure 36. Antibiotics were physisorbed onto stainless steel substrates to demonstrate detection by LDPI-MS and characterize fragmentation patterns in the absence of biofilms. Figure 36 shows the analysis of a mixture of rifampicin, ciprofloxacin, and

trimethoprim combined with a series of calibration compounds found that all three antibiotics formed radical cation parent ions. It is expected that radical cation formation dominated for all antibiotics studied here. Laser desorption power was sufficiently low to prevent direct ionization in the absence of postionization. Further, none of these samples showed any significant vapor pressure at room temperature in vacuum, as no postionization signal was observed in the absence of laser desorption.

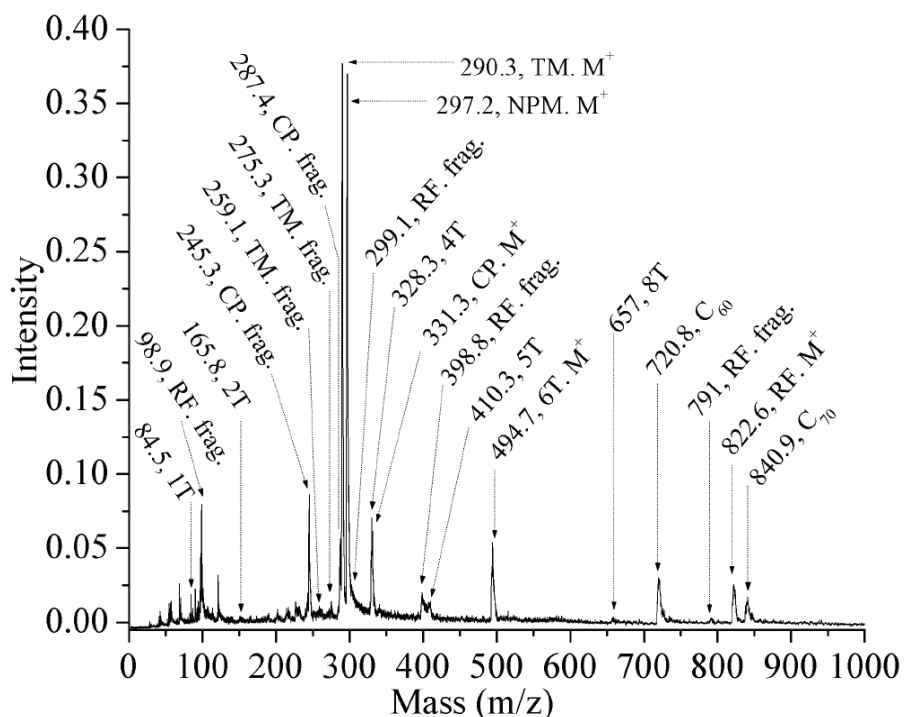


Figure 36: Showing radical cationization using 7.87 eV LDPI-MS.

7.87 eV LDPI-MS of a mixture of rifampicin (RF), ciprofloxacin (CP), and trimethoprim (TM) all displayed radical cation parent ions. Internal mass calibration was performed using four standards mixed into the sample: N-(1-pyrene)maleimide (NPM, mol. wt. 297.3 Da), sexithiophene (6T, 494.7 Da), and C_{60/70} (720.7 and 840.7 Da). 1T, 2T, 3T, 4T, 5T, and 8T correspond to the number of thiophene units from fragments or impurities of 6T.

6.3.2 Detection of Neat Antibiotics by LDPI-MS.

The ability to detect specific antibiotics by 7.87 eV LDPI-MS was first determined on neat samples. LDPI-MS analysis of neat antibiotics also allowed characterization of their

fragmentation patterns. Toloxatone, trimethoprim, ciprofloxacin, ampicillin, lincomycin, oxacillin, oxytetracycline, azithromycin, rifampicin, and coumermycin A1 were physisorbed onto separate stainless steel substrates for analysis by LDPI-MS. All but ampicillin and coumermycin A1 showed stable parent cations (see previous Section: 6.3.1), indicating direct radical cation formation via VUV SPI (Hanley and Zimmerman, 2009). Chapter 3 demonstrated neat detection of sulfadiazine, tetracycline, and novobiocin by 7.87 eV LDPI-MS. Most of the antibiotics detected possess secondary and tertiary aromatic amines which are expected to display ionization energies below 7.87 eV photon energies. Laser desorption power was sufficiently low to prevent direct ionization in the absence of postionization. Further, none of these samples showed any significant vapor pressure at room temperature in vacuum, as no postionization signal was observed in the absence of laser desorption (data not shown).

6.3.3 Assignment of Parent and Fragment Ions.

Toloxatone is an oxazolidinone antibiotic which displayed a prominent parent ion peak at m/z 207 and four fragments at m/z 163, 147, 133, and 115. Trimethoprim displayed a dominant parent ion at m/z 290 and $[M-NH_2]^+$ fragment due to loss of amine at m/z 274 and $[M-CH_3O]^+$ at m/z 259. Ciprofloxacin showed a prominent parent peak at m/z 331 and fragments at m/z 286 and 246. Lincomycin displayed a m/z 406 parent ion and fragments due to $[M-CH_3]^+$ at m/z 391 and $[M-CH_3SH]^+$ at m/z 359. Oxacillin displayed a parent ion at m/z 401 and fragments at m/z 356, 324, 243, and 186. The oxytetracycline parent appeared at m/z 460 while $[M-OH]^+$ and $[M-2OH]^+$ appeared at m/z 444 and 426, respectively. Azithromycin displayed a weak parent ion at m/z 748 and fragments at m/z 719, 704, 632, 588, 574, 415, 174, 158, and 116. Rifampicin showed an intense parent ion at m/z 823 with abundant fragments at m/z 399, 298, and 99.

Ampicillin (M.W. 349 Da) and coumermycin A1 (1110 Da) did not produce stable parent ions, but were verified according to fragments peaks identified in the literature.(Smyth et al., 2003; Kammerer et al., 2004) In addition to the absence of a parent ion, vancomycin (1449 Da) was not successfully detected due to extensive fragmentation, only displaying unidentified peaks below m/z 400.

All major peaks for all antibiotics are listed in Table 2 including their mass to charge ratio (m/z) and assigned structure. Table 2 also shows sulfadiazine and tetracycline peaks from previous work for comparison with oxytetracycline (see Chapter 3). Major spectral peaks were compared to chemical structures obtained from commercial fragmentation analysis software (ACD/MS Fragmenter, Advanced Chemistry Development Inc., Toronto, Ont., Canada) to assist elucidation of fragmentation pathways (shown in Appendix A, Figures A1 – A12). The software simulates fragmentation according to standard rules for electron ionization using specific fragmentation for all forms of hemolytic and heterolytic cleavages of both odd and even-electron ions including aromatic bond cleavage; resonance reactions; 1,3-shifts; 1,5-shifts; and McLafferty rearrangements. Both electron ionization and SPI result in the formation of a radical cation.

Figure 37 shows a number of neat antibiotics detect by 7.87 eV. LDPI-MS Toloxatone and lincomycin each showed a dominate parent peak with a parent-to-fragment (M/F) ion ratio exceeding unity. Neat trimethoprim displayed a M/F ratio of 20. Rifampicin and ciprofloxacin showed M/F values from 0.25 to 0.65 whereas those for oxacillin, oxytetracycline and azithromycin were between 0.03 and 0.05.

	CLASS	ANTIBIOTICS		Peaks			CLASS	ANTIBIOTICS		Peaks			CLASS	ANTIBIOTICS		Peaks					
		m/z	Structure	Neat	BF			m/z	Structure	Neat	BF			m/z	Structure	Neat	BF				
synthetic	oxaxolidinone	toloxatone					natural product	lincomycin					semi-synthetic	azithromycin							
		207 M ⁺		x	NA	406 M ⁺			x	NA	748 M ⁺			x	NA	719 [M-C ₂ H ₅] ⁺		x	NA		
		163 [M-CO ₂] ⁺		x	NA	391 [M-CH ₃] ⁺			x	NA	704 [M-C ₂ H ₆ N] ⁺			x	NA	588 [M-C ₈ H ₁₆ O ₃] ⁺		x	NA		
		147 [M-C ₂ H ₄ O ₂] ⁺		x	NA	372 [M-2OH] ⁺			x	NA	574 [M-C ₈ H ₁₆ NO ₃] ⁺			x	NA	415 [M-C ₁₆ H ₃₁ NO ₆] ⁺		x	NA		
		133 [M-C ₂ H ₂ O ₃] ⁺		x	NA	359 [M-CH ₃ S] ⁺			x	NA	174 [M-C ₃₀ H ₅₇ NO ₉] ⁺			x	NA	158 [M-C ₃₀ H ₅₆ NO ₁₀] ⁺		x	NA		
	115 [M-C ₇ H ₈] ⁺		x	NA	342 [M-CH ₄ OS] ⁺			x	NA	116 [M-C ₃₃ H ₆₂ NO ₁₀] ⁺		x		NA	43 [C ₂ H ₅ N] ⁺		x	NA			
	sulfonamide	sulfadiazine						β-lactam	oxacillin						rifamycin	rifampicin					
		250 M ⁺		x	x	401 M ⁺				x	NA	823 M ⁺				x	x	795 [M-CO] ⁺		x	x
		210 [M-C ₂ H ₂ N] ⁺		x	x	356 [M-CHO ₂] ⁺				x	NA	791 [M-CH ₃ O] ⁺				x	x	399 [M-C ₂₃ H ₃₅ O ₇] ⁺		x	x
		183 [M-C ₃ H ₃ N ₂] ⁺		x	x	324 [M-C ₆ H ₅] ⁺				x	NA	298 [M-C ₂₈ H ₄₆ N ₂ O ₇] ⁺				x	x	182 [C ₁₀ H ₁₆ NO ₂] ⁺		x	-
		trimethoprim				243 [M-C ₁₀ H ₈ NO] ⁺				x	NA	152 [C ₉ H ₁₄ NO] ⁺		x		-	99 [C ₅ H ₁₁ N ₂] ⁺		x	x	
	290 M ⁺		x	-	186 [M-C ₈ H ₁₁ N ₂ O ₃ S] ⁺				x	NA	157 [M-C ₉ H ₁₁ N ₂ O ₄ S] ⁺		x	NA		coumermycin A1					
	274 [M-NH ₂] ⁺		x	-	157 [M-C ₉ H ₁₁ N ₂ O ₄ S] ⁺				x	NA	1110 M ⁺		-	NA		512 Kammerer <i>et al.</i> 2004		x	NA		
	259 [M-CH ₃ O] ⁺		x	-	44 [CHO ₂] ⁺				x	NA	502 Kammerer <i>et al.</i> 2004		x	NA		487 Kammerer <i>et al.</i> 2004		x	NA		
	244 [M-C ₂ H ₆ O] ⁺		x	x	tetracycline						446 Kammerer <i>et al.</i> 2004		x	NA		395 Kammerer <i>et al.</i> 2004		x	NA		
	230 [M-C ₂ H ₄ O ₂] ⁺		x	x	444 M ⁺				x	x	265 [M-C ₄₁ H ₄₀ N ₄ O ₁₆] ⁺		x	NA		232 Kammerer <i>et al.</i> 2004		x	NA		
	168 [M-C ₅ H ₆ N ₄] ⁺		-	x	427 [M-OH] ⁺			x	x	206 Kammerer <i>et al.</i> 2004		x	NA	125 [M-C ₄₉ H ₅₂ N ₄ O ₁₈] ⁺		x	NA				
	150 [M-C ₅ H ₈ N ₄ O] ⁺		x	-	410 [M-2OH] ⁺			x	x	107 Kammerer <i>et al.</i> 2004		x	NA	aminocoumarin							
135 [M-C ₆ H ₁₁ N ₄ O] ⁺		x	x	400 [M-C ₂ H ₆ N] ⁺		x	x	ampicillin													
123 [M-C ₉ H ₁₁ O ₃] ⁺		x	x	383 [M-C ₂ H ₇ NO] ⁺		x	x	349 M ⁺		-	NA										
109 [M-C ₁₀ H ₃ O ₃] ⁺		x	x	373 [M-C ₂ HNO ₂] ⁺		x	x	333 Smyth <i>et al.</i> 2003		x	NA										
93 [C ₄ H ₃ N ₃] ⁺		x	x	357 [M-C ₃ H ₇ N ₂ O] ⁺		x	x	304 [M-CHO ₂] ⁺		-	NA										
quinolone	ciprofloxacin				337 [M-C ₂ HNO ₂] ⁺		x	x	289 Smyth <i>et al.</i> 2003		x	NA									
	331 M ⁺		x	x	337 [M-C ₂ HNO ₂] ⁺		x	x	215 [M-C ₈ H ₈ NO] ⁺		x	NA									
	286 [M-CHO ₂] ⁺		x	x	357 [M-C ₃ H ₇ N ₂ O] ⁺		x	x	200 [M-C ₈ H ₉ N ₂ O] ⁺		x	NA									
	246 [M-C ₄ H ₆ N ₂] ⁺		x	x	337 Gasper <i>et al.</i> 2008		x	x	192 Smyth <i>et al.</i> 2003		x	NA									
	ampicillin				332 [M-C ₄ H ₂ NO ₃] ⁺		x	x	170 [M-C ₉ H ₉ NO ₃] ⁺		x	NA									
natural product	β-lactam	ampicillin					polyketides	oxytetracycline					natural product	aminocoumarin							
		349 M ⁺		-	NA	460 M ⁺			x	x	1110 M ⁺			-	NA	512 Kammerer <i>et al.</i> 2004		x	NA		
		333 Smyth <i>et al.</i> 2003		x	NA	444 [M-NH ₂] ⁺			x	x	502 Kammerer <i>et al.</i> 2004			x	NA	487 Kammerer <i>et al.</i> 2004		x	NA		
		304 [M-CHO ₂] ⁺		-	NA	426 [M-2OH] ⁺			x	x	446 Kammerer <i>et al.</i> 2004			x	NA	395 Kammerer <i>et al.</i> 2004		x	NA		
		289 Smyth <i>et al.</i> 2003		x	NA	416 [M-C ₂ H ₆ N] ⁺			x	x	265 [M-C ₄₁ H ₄₀ N ₄ O ₁₆] ⁺			x	NA	232 Kammerer <i>et al.</i> 2004		x	NA		
		215 [M-C ₈ H ₈ NO] ⁺		x	NA	399 [M-C ₂ H ₇ NO] ⁺			x	x	206 Kammerer <i>et al.</i> 2004			x	NA	125 [M-C ₄₉ H ₅₂ N ₄ O ₁₈] ⁺		x	NA		
		200 [M-C ₈ H ₉ N ₂ O] ⁺		x	NA	382 [M-C ₂ H ₈ NO ₂] ⁺			x	x	107 Kammerer <i>et al.</i> 2004			x	NA	aminocoumarin					
		192 Smyth <i>et al.</i> 2003		x	NA	373 [M-C ₃ H ₇ N ₂ O] ⁺			x	-	ampicillin										
		170 [M-C ₉ H ₉ NO ₃] ⁺		x	NA	365 [M-C ₂ H ₉ NO ₃] ⁺			x	x	349 M ⁺			-	NA						
		155 [M-C ₉ H ₁₀ N ₂ O ₃] ⁺		x	NA	327 [M-C ₄ H ₉ N ₂ O ₃] ⁺			x	x	333 Smyth <i>et al.</i> 2003			x	NA						
		145 [M-C ₈ H ₆ N ₂ O ₃ S] ⁺		x	NA	polyketides				289 Smyth <i>et al.</i> 2003		x		NA							
		134 [M-C ₈ H ₁₁ N ₂ O ₃ S] ⁺		x	NA	polyketides				215 [M-C ₈ H ₈ NO] ⁺		x		NA							
		106 [M-C ₉ H ₁₂ N ₂ O ₄ S] ⁺		x	NA	polyketides				200 [M-C ₈ H ₉ N ₂ O] ⁺		x		NA							
77 [C ₆ H ₅] ⁺		x	NA	polyketides				192 Smyth <i>et al.</i> 2003		x	NA										
44 Smyth <i>et al.</i> 2003		x	NA	polyketides				170 [M-C ₉ H ₉ NO ₃] ⁺		x	NA										
28 Smyth <i>et al.</i> 2003		x	NA	polyketides				155 [M-C ₉ H ₁₀ N ₂ O ₃] ⁺		x	NA										

Table 2: Antibiotic fragmentation during 7.87 eV LDPI-MS.

Peaks denoted by “x” where observed, “-” absent, and antibiotics not tested in biofilms are listed as “NA.”

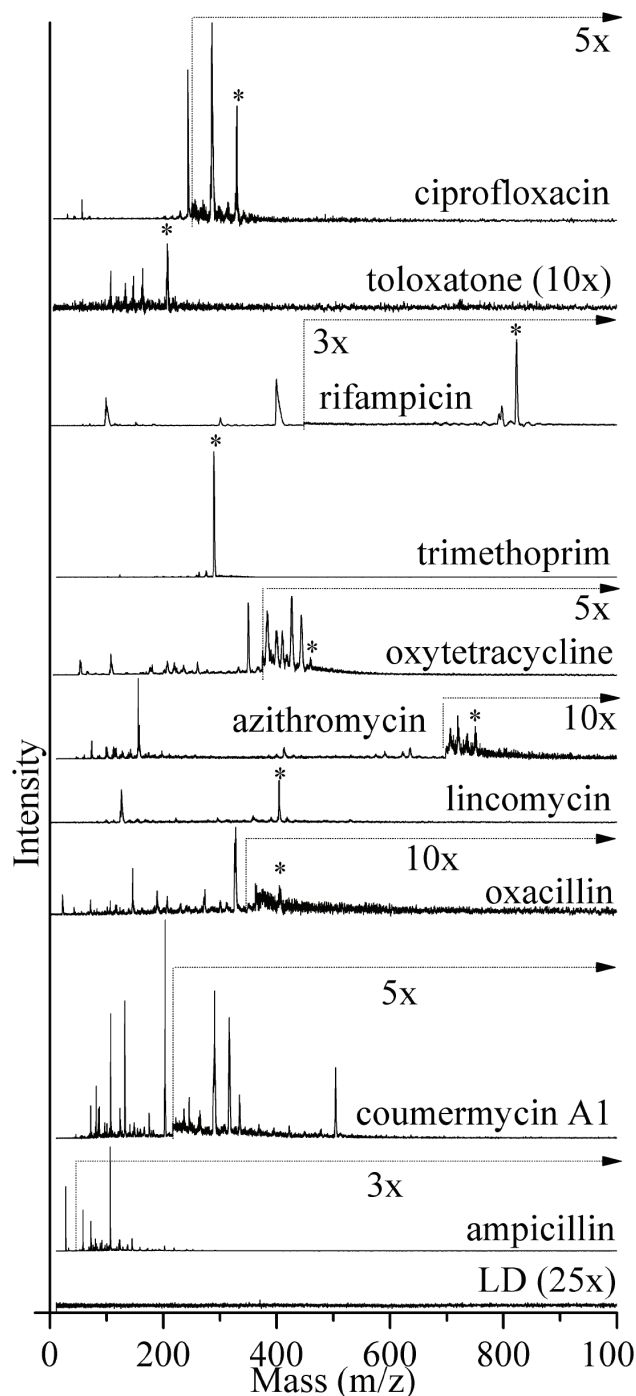


Figure 37: 7.87 eV LDPI-MS of ten neat antibiotics.

7.87 eV LDPI-MS of the following neat antibiotics from dried droplets on stainless steel substrates: ciprofloxacin (m/z 331 parent ion, marked by an asterick), toloxatone (m/z 207), rifampicin (m/z 823), trimethoprim (m/z 290), oxytetracycline (m/z 460), azithromycin (m/z 748), lincomycin (m/z 406), oxacillin (m/z 401), coumermycin A1, and ampicillin. Direct ionization (LD), in the absence of postionization, did not yield signal for any antibiotic, as shown for trimethoprim (bottom).

6.3.4 Detection of Antibiotics in Bacterial Biofilm by 7.87 eV LDPI-MS.

Various antibiotics were detected at concentrations from 0.3 to 1.7 mM in biofilms grown on polycarbonate membranes when the antibiotics were introduced through agar media and allowed to diffuse and equilibrate with the biofilm. Figure 38 shows the results of these studies. It was previously observed that the antibiotics affected cell viability in biofilms doped at these near clinical concentrations (refer to bacterial biofilm viability study in Chapter 3). Compared to neat studies, biofilm spectra reflect differences in antibiotic fragment abundances, with further discussion of the fragment ions provided in Table 2 and Section: 6.3.3. Chemical noise contribution from the biofilms was insignificant and absent during LD. Previous work detected constituents from the biofilms by LDPI-MS at photon energies above 8 eV, with ≥ 10.5 eV photon energies displaying improved antibiotic sensitivity (see Chapters 4 and 5).

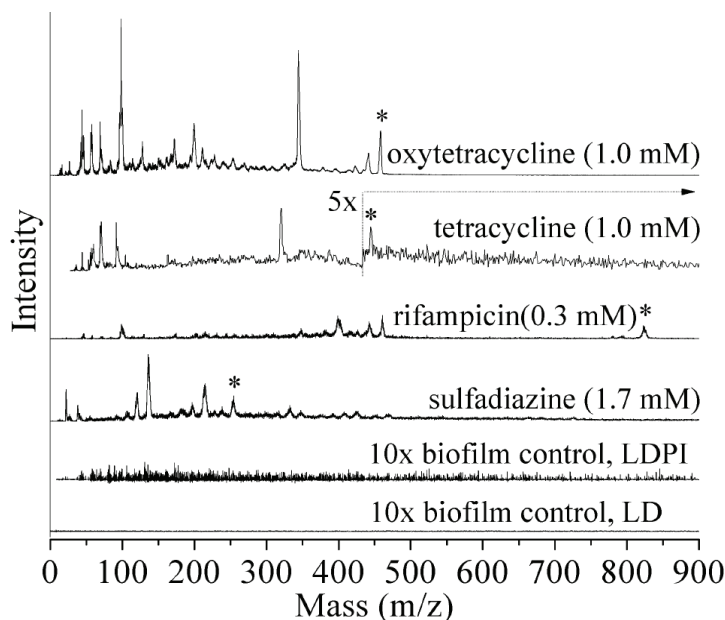


Figure 38: 7.87 eV LDPI-MS of antibiotic doped membrane biofilm.

LDPI-MS of *S. epidermidis* colony biofilm grown on polycarbonate membrane with 0.2 micron pore size was doped for one hour with respective antibiotics at listed concentrations (top to bottom): 1.0 mM oxytetracycline, 1.0 mM tetracycline, 0.3 mM rifampicin, and 1.7 mM sulfadiazine. LDPI and laser desorption only (LD) of biofilm control without antibiotic are also shown. Asterisks used to mark parent ions.

Control experiments were also performed on the membrane biofilm samples. Biofilms grown on a polycarbonate membrane without antibiotic did not show any direct ionization or significant LDPI-MS signal, as indicated by the LDPI and LD control spectra displayed at the bottom of Figure 38. However, the biofilm control measured with LDPI-MS did display considerable chemical noise and under higher desorption laser powers, significant signal below m/z 150. None of these four antibiotics in membrane biofilms displayed any direct ionization (LD only). Polycarbonate membranes without biofilm or antibiotic did not show LD or LDPI-MS signal except at very high laser desorption powers. The biofilm, nutrient supply, and tryptic soy agar, did not display any significant LD or LDPI-MS signal (most of the data described in this paragraph not shown).

6.3.5 Differences in Antibiotic Fragmentation Present in Biofilm

The detection of antibiotics by LDPI-MS displays changes in parent-to-fragment ion ratios (M/F) in the presence of the biofilm environment. Fragmentation increases in the biofilm spectra compared to the neat spectra, giving rise to additional peaks shown in Table 2. There was a 25 – 50% reduction in M/F value from neat to biofilm spectra.

In some cases, particular antibiotic fragments dominate the biofilm spectra. For example, oxytetracycline within the biofilm clearly showed signature fragments at m/z 445, 426, 400, and 384 with a significant enhancement of the m/z 356 fragment. Similarly, the intensity of tetracycline fragment at m/z 337 was enhanced in the biofilm, as seen previously. In other cases, spectral congestion appeared to obscure antibiotic peaks in the biofilm. For example, the m/z 185 fragment peak was used to identify trimethoprim in the biofilm cross section, since the trimethoprim parent peak appeared buried in the chemical noise envelope that dominated the

spectra. Sulfadiazine was a case where few differences were observed in biofilm spectra compared to those from neat samples.

Rifampicin was somewhat unique amongst the antibiotics examined as it presented a series of new peaks from the biofilms compared to those observed from neat samples. The biofilm presented the parent ion and signature fragments from the neat rifampicin spectra at m/z 795, 775, 398, 299, and 99 while continuing to display a very distinct baseline absent of intense fragments from m/z 500 to 775. However, the biofilm doped rifampicin also displayed new peaks at m/z 475, 450 and other lower masses. These new peaks could be justified as fragments of rifampicin or they may have resulted from new species released from the biofilm as the result of antibiotic treatment. Further work is investigating the origin of these new peaks.

6.3.6 MS Imaging Antibiotics without Matrix.

MS imaging experiments started with an investigation on a membrane biofilm that equilibrated with rifampicin doped into the nutrient medium (Hanley and Zimmerman, 2009). Figure 39 displays the result of imaging the rifampicin parent ion from a sector of the membrane biofilm. Biofilms grown on membranes were allowed to equilibrate for one hour with the agar doped with antibiotic, after which the biofilm was assumed to have reached the concentration of antibiotic in the agar. Prior work argued that the equilibration of a uniform, ~ 300 μm thick biofilm with 90% of bulk fluid concentration requires ~ 20 min. to equilibrate small antibiotics such as chlorhexidine (Stewart, 2003).

The contour plot of rifampicin (m/z 823), Figure 39 (right), displayed a uniform baseline signal outside the area of the biofilm. Within the biofilm, the distribution of the antibiotic was

non-uniform. This result was unexpected, given the antibiotic was provided nearly three times the time necessary to penetrate the biofilm bulk space and equilibrate.

This experiment was carried further with the preparation of a membrane biofilm given insufficient time for rifampicin to diffuse. Only five minutes were provided for a saturated solution of rifampicin to diffuse across the membrane biofilm before the sample was dehydrated to cease the solvent migration of the analyte. Diffusion constants were not known for rifampicin in a biofilm, so an accurate diffusion calculation was not performed. However, the previously mentioned times for diffusion do not describe the lateral diffusion in this experiment.

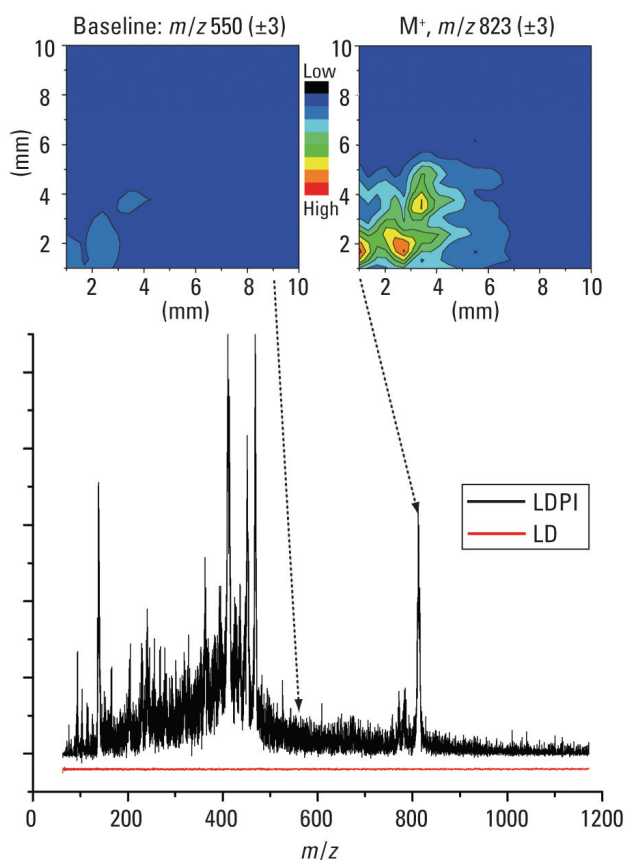


Figure 39: MS image of rifampicin distribution in sector of membrane biofilm. (top curve) 7.87 eV LDPI-MS for rifampicin (MW: 823) detected within an intact membrane *S. epidermidis* biofilm, (bottom curve) the LD-only mass spectrum. MS images: (top right) distribution of rifampicin parent at m/z 823 ± 3 , (top left) arbitrary mass from baseline at m/z 550 ± 3 displays no signal. Intensity represented by color scale.

Figure 40 displays the resulting MS image of rifampicin distributed throughout a membrane biofilm. The distribution represents less uniformity as a result of providing 25% of the theoretical time needed for a similar chemical compound to penetrate the bulk from a uniform administration. Once again, rifampicin was administered as a concentrated dose at the far left end of the membrane and allowed to diffuse laterally across the biofilm bulk.

The signal intensity was integrated to represent the signal change across the diffusion axis (x-axis) and shown in Figure 41. This plot clearly shows a concentration gradient of rifampicin across the biofilm and may indicate the major concentration front or an instrumental limit of detection near 32 mm.

Analysis of membrane biofilms is complicated by the difficulty of maintaining a flat surface. The polycarbonate membrane can also lead to charging which can distort MS collection. Biofilms grown on rigid substrate provides the advantage of producing thinner and flatter biofilms. Investigations using these models will be covered in the subsequent sections.

Next, LDPI-MS imaging was performed on an antibiotic in a biofilm. Sulfadiazine was administered into the nutrient supply of a drip flow biofilm, then the antibiotic distribution was imaged within the intact biofilm. Figure 42 (a) shows the LDPI-MS image mapping the non-uniform distribution of the dominant m/z 185 ± 2 fragment of sulfadiazine at 5.2 mM concentration in the bacterial biofilm. Other figure panels show (b) SEM and (c) optical images of the same $900 \times 900 \mu\text{m}^2$ area that was scanned near the substrate-biofilm boundary with the silicon substrate (Si) and biofilm (BF) visible in both images. Sulfadiazine signal was observed within the biofilm area and showed no accumulation near the edge of the biofilm-substrate interface. LDPI-MS image resolution was determined by scanning parameters that averaged spectra over a $100 \mu\text{m}$ vertical distance along each scan line, with the stage moving in $50 \mu\text{m}$

horizontal steps, resulting in a $100 \times 50 \mu\text{m}$ pixel (see below). The SEM and optical images show an intentional laser burn (post analysis) at the lower left hand corner for the purpose of alignment.

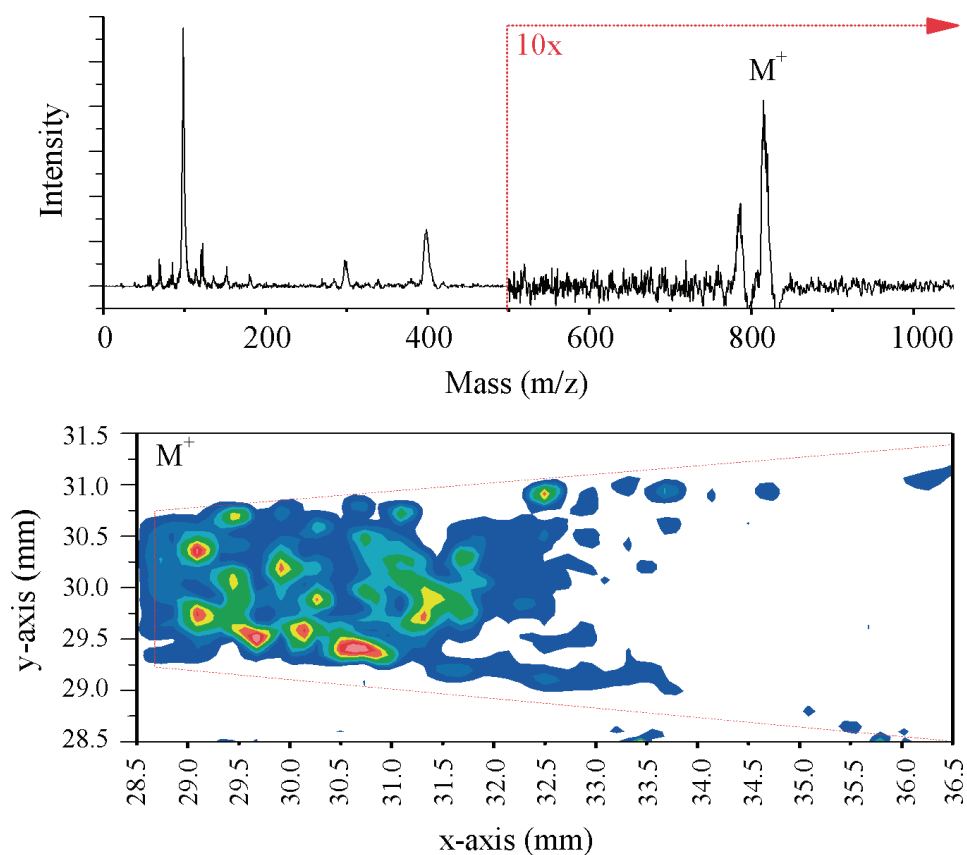


Figure 40: LDPI-MS image of rifampicin concentration gradient in biofilm. (top) LDPI-MS global spectrum of rifampicin detected within intact *S. epidermidis* biofilms grown on polycarbonate membrane. (bottom) concentration gradient of rifampicin parent ion $m/z 822 \pm 1$ within membrane biofilm cut into shape of wedge. Linear dependence of ion intensity in image indicated by color: Pink > red > yellow > green > aqua > blue.

Various control experiments were performed to verify that the images observed were not due to experimental artifacts. LDPI-MS experiments on a control film of $C_{60/70}$ demonstrated little variation in signal when the film appeared optically uniform, regardless of substrate. In the absence of laser desorption, postionization signal of triethylamine vapor at constant pressure also showed little fluctuation (these data not shown).

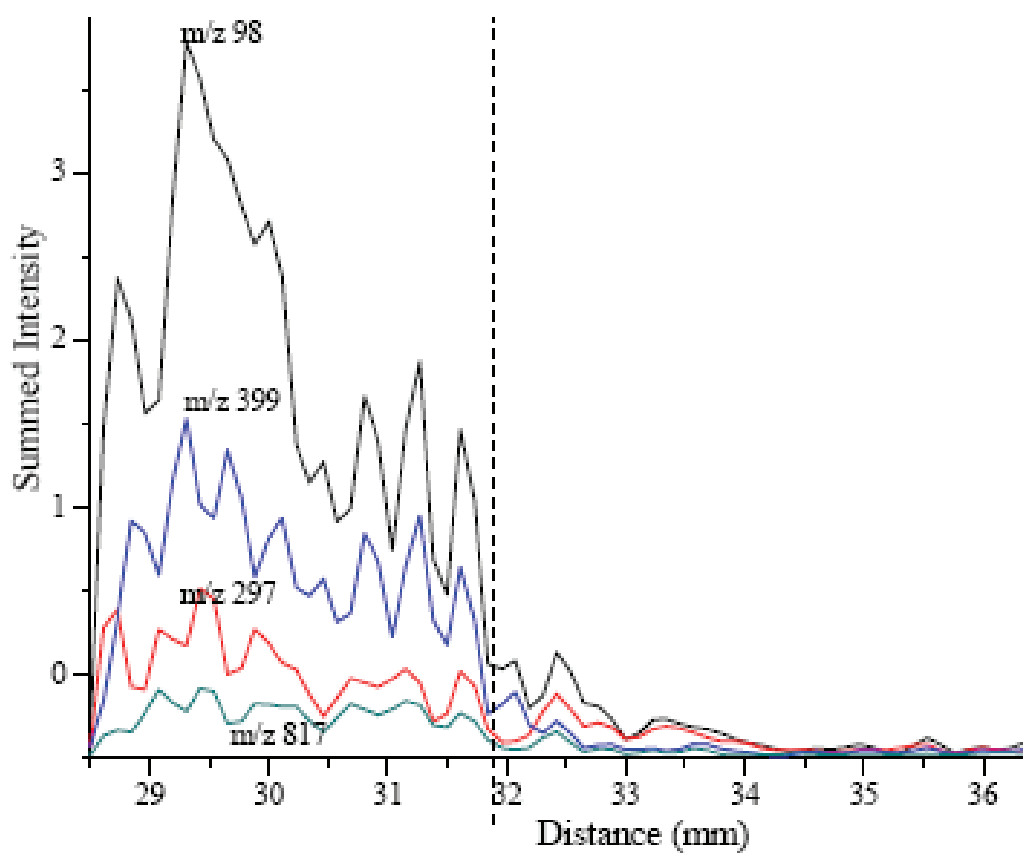


Figure 41: Integration of rifampicin signal intensity along gradient axis. Integrated signal of selected rifampicin peaks (m/z 823, 297, 399, and 99) along gradient axis. Dashed line near 32 mm may represent end of diffusion or instrumental limit of detection.

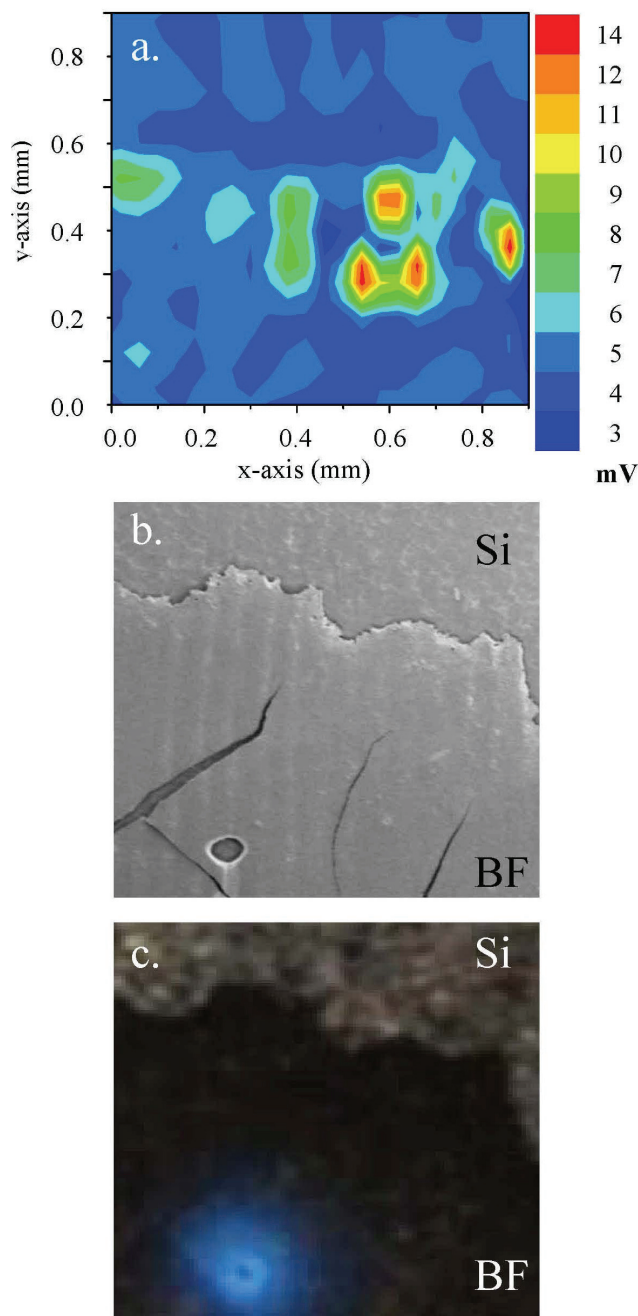


Figure 42: LDPI-MS image, SEM, and optical image of drop flow biofilm.

LDPI-MS, scanning electron microscopy (SEM), and optical images in bacterial biofilm grown by drip flow method with 5.2 mM sulfadiazine on silicon substrate. (a) Contour plot of m/z 185 ± 2 corresponding to sulfadiazine fragment distribution, (b) SEM image, and (c) optical image. Labels show biofilm (BF) and the silicon substrate (Si), with each image displaying the same $900 \times 900 \mu\text{m}^2$ area. Color scale on (a) corresponds to detector output voltage. Circular marks at lower left hand corner of (b) and (c) are laser burn created for reference. Scanning parameters were vertical velocity of $200 \mu\text{m}/\text{sec}$ and horizontal steps of $50 \mu\text{m}$.

6.3.7 MS Imaging Antibiotics with Matrix.

MALDI-MS imaging requires addition of a matrix compound to detect analyte ions (Seeley and Caprioli, 2008; Chughtai and Heeren, 2010). Matrix addition also slightly increased signal here. However, use of the revised experimental LDPI-MS configuration led to the greatest increase in sensitivity, giving a ~ 20 fmol limit of detection for ciprofloxacin in biofilm.

The LDPI-MS instrument with the new detector and ion optics was used to interrogate ciprofloxacin doped biofilms grown by drip flow on ITO glass slides. CHCA matrix was then applied to these biofilms by airbrush. Experiments monitored three characteristic peaks in ciprofloxacin that included the parent (M^+ , m/z 331) and fragment ions (m/z 286, 246), as shown in Figure 43. 25 μL aliquots of 2 μM ciprofloxacin solution were administered to a bacterial biofilm grown on an ITO glass slide with an area of 4 cm^2 , leading to an equilibrated biofilm concentration of ~ 10 pmol/ cm^2 . The desorption laser spot size was 25 μm which therefore removed ~ 0.5 femtomoles per laser shot. The ~ 50 fmol calculated from spectra averaged over 100 laser shots was extrapolated down to a ~ 20 fmol limit of detection at a signal to noise ratio of 3.

Peaks at m/z 355 and 370 were observed in all biofilm spectra recorded with added CHCA matrix, but were absent in the neat ciprofloxacin spectrum: these peaks along with m/z 318 derive from fragmented dimers of CHCA (Smirnov et al., 2004). All other fragments associated with ciprofloxacin were buried in the chemical noise. There were no distinguishable peaks above m/z 400, while matrix peaks dominated below m/z 200. The peaks at m/z 262 and 300 were assumed to be exogenous biofilm components as they could not be assigned to the matrix or antibiotic.

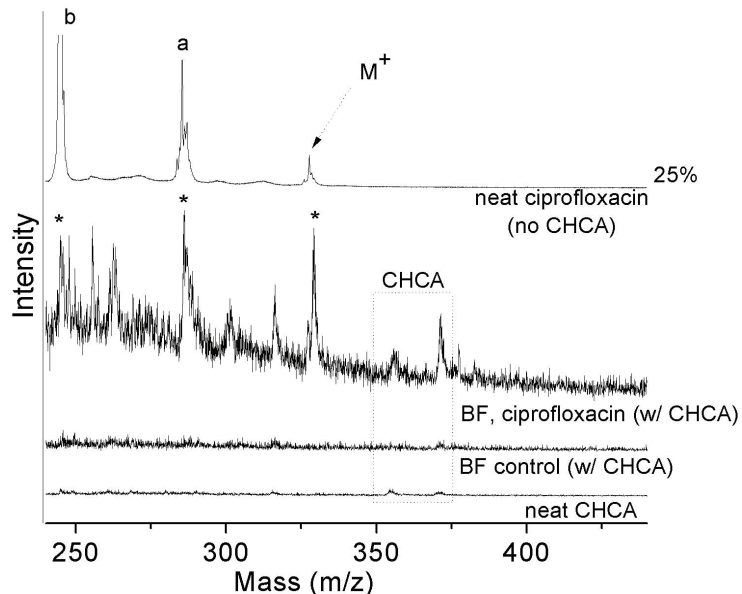


Figure 43: LDPI-MS spectra of ciprofloxacin fragments.

(a, b), and parent ions (M^+ , m/z 331) detected from drip flow biofilm grown on ITO coated glass slide airbrushed with CHCA matrix. Spectra included neat ciprofloxacin (no CHCA), and biofilm control (BF, no ciprofloxacin), both on ITO substrate. Note that neat ciprofloxacin was scaled by 25%.

Further experiments demonstrated the limited extent of matrix enhancement of desorbed neutrals via exploitation of the imaging capabilities of the LDPI-MS instrument. CHCA matrix was applied as small spots on ciprofloxacin-doped drip flow biofilms by airbrush and nano spotter methods (Végyvári et al., 2010): both showed parent ion enhancement and fragment ion suppression. Figure 44 shows a general cartoon of how the sample was prepared for the matrix experiment.

Figure 44 provides an introductory scheme for the matrix experiment covered in the subsequent text and Figure 45. A drip flow biofilm was grown on ITO substrate and doped with ciprofloxacin. The left-most third was airbrushed with CHCA matrix. The rest of the sample was

nano spotted with CHCA matrix. An MS imaging experiment was performed that represented both areas of matrix application.

Figure 45 displays LDPI-MS representing the sum of data collected from 110 spectra from each area with either airbrushed matrix or nano spotted matrix as well as a third area without matrix (refer to Figure 44). The labeled peaks represent a CHCA fragment peak at m/z 144, ciprofloxacin fragments, and the parent (M^+) ion at m/z 331 (ciprofloxacin peaks labeled by “*”). Ciprofloxacin fragments included: loss of fluorine at m/z 313, loss of carboxylic acid at m/z 286, loss of piperazine group (denoted $C_4H_9N_2$) at m/z 244, loss of both piperazine and hydroxyl at m/z 230, and loss of both piperazine and carboxylic acid at m/z 202.

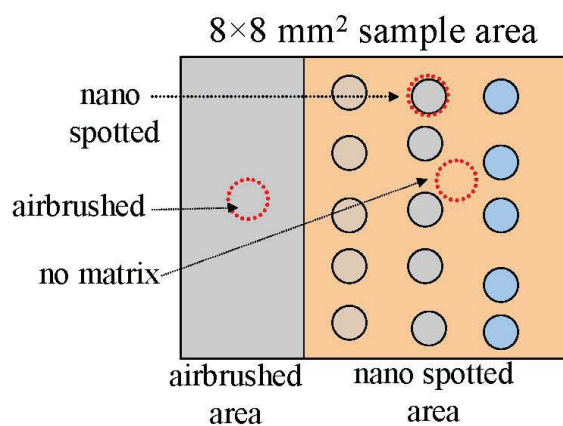


Figure 44: Cartoon of matrix experiment.

Ciprofloxacin doped drip flow biofilm with matrix applied by airbrush and by nano-spotter.

It is well known that matrix absorbs UV laser energy in a sample, leading to enhanced desorption and ionization while minimizing fragmentation in MALDI-MS (Chughtai and Heeren, 2010). The significance of matrix cooling for laser desorbed neutrals was probed here via ciprofloxacin parent to m/z 246 fragment ratios (M/F). Areas of airbrushed and nano spotted matrix represented 3 ± 1 and 10 ± 3 fold increases of M/F compared to the area with no CHCA matrix, respectively. This result suggests that fragmentation suppression contributed significantly

to parent ion enhancement and that changes in M/F may not have resulted solely from the enhancement of desorbed neutrals.

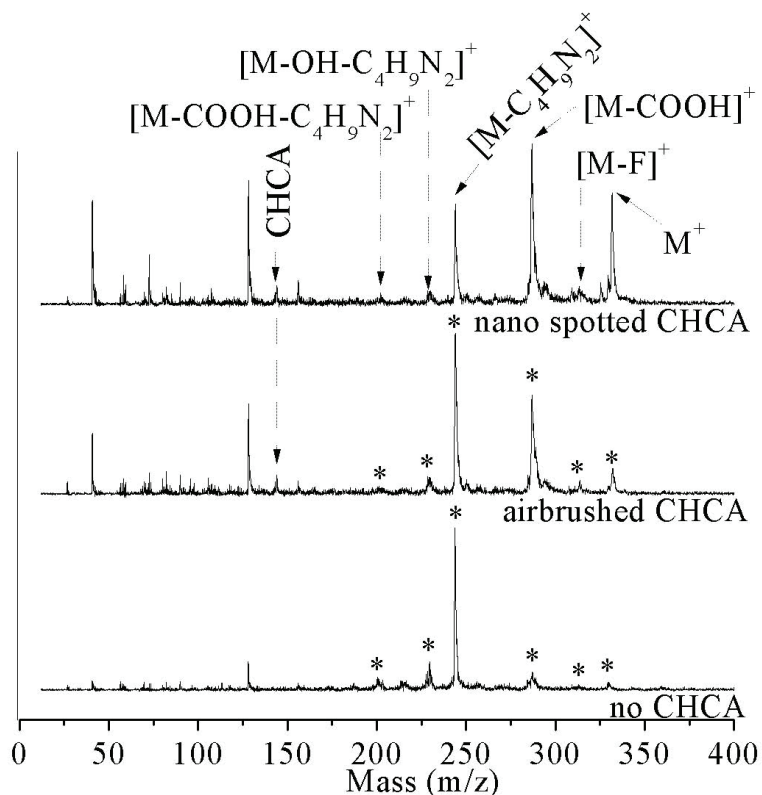


Figure 45: LDPI-MS spectra of regions of interest for matrix and non-matrix areas.

LDPI-MS spectra from representative areas: nano spotted matrix, airbrushed matrix, and no matrix. Peaks represent (CHCA) matrix, ciprofloxacin fragments, and (M^+) ciprofloxacin parent ion, m/z 331. Each spectrum is the sum of 110 spectra collected from a $250 \times 250 \mu\text{m}^2$ area. The fragments of ciprofloxacin peaks labeled by structures (i.e., parent ion after loss of piperazine [$M - C_4H_9N_2$] $^+$) and “*” are discussed within the text.

However, total ion signal from the three areas probed in Figure 45 were within 15% of each other, despite the presence of matrix. There was only slight overall enhancement in analyte ion signal upon addition of matrix, unlike MALDI-MS, indicating that an increase in neutral yield was not a major contributor to parent ion enhancement. Rather, fragmentation suppression

occurred via the cooling of neutrals (Bae et al., 2011), thereby reducing internal energy of the desorbed system and lowering the rate of molecular fragmentation.

A ciprofloxacin-doped drip flow biofilm was prepared to further investigate the fragment suppression occurring in the presence of matrix. In Figure 44, a sample area of 8×8 mm was imaged that included sprayed and nano spotted matrix. CHCA was applied by airbrush (left third of each panel) and nano spotter (right two thirds). The nano liter drops were deposited in three vertical columns (left to right: 5, 10, and 20 mg CHCA/mL). The three panels in Figure 46 represent MS images of CHCA fragment at m/z 143.9 ± 0.5 (panel a), ciprofloxacin fragment at m/z 244 ± 1.0 (panel b), and ciprofloxacin parent ion at m/z 331 ± 0.8 (panel c).

The changing abundance of respective peaks was monitored across matrix interfaces in order to characterize the desorption event. Images of parent to fragment ion ratios (M/F, data not shown) showed M/244 ratio to resemble parent ion images. Further, total ion counts (TIC) from the three areas, described in Figure 45, were within 15% of each other. This indicates an increase in neutral yield was not a major contributor to parent ion enhancement. Rather, it suggests fragmentation suppression occurred via the cooling of neutrals, thereby reducing internal energy of the desorbed molecules and lowering the extent of molecular fragmentation.

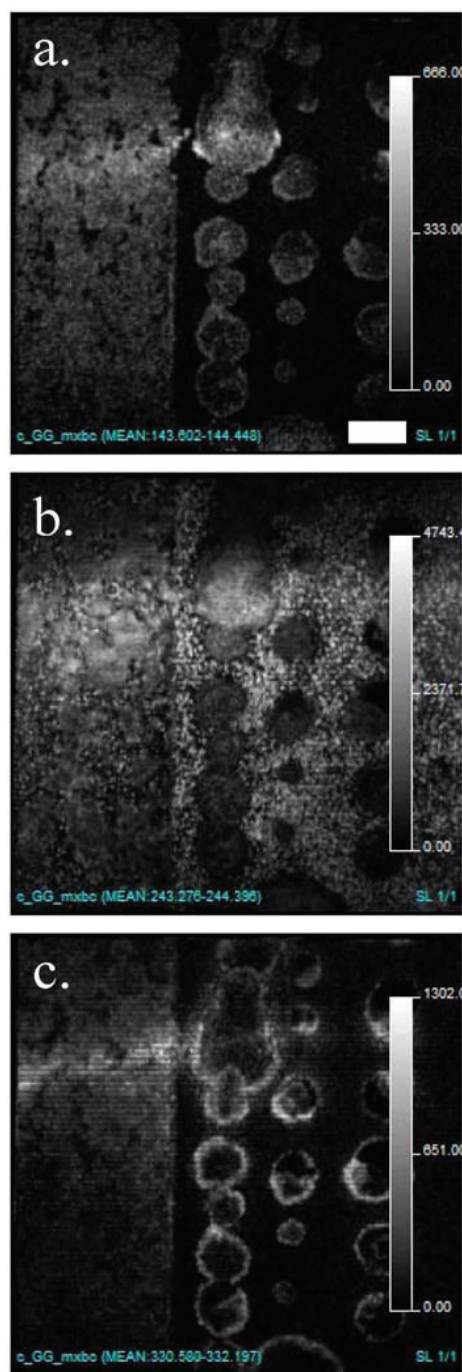


Figure 46: LDPI-MS images of ciprofloxacin doped biofilm with CHCA matrix.

MS images of a) CHCA fragment at m/z 143.9 ± 0.5 , b) ciprofloxacin fragment at m/z 244 ± 1.0 , and c) ciprofloxacin parent ion at m/z 331 ± 0.8 . CHCA was applied by airbrush (left third of each image), and nano spotter (right two thirds). Nano liter drops were deposited in three vertical columns (left to right, 5, 10, and 20 mg CHCA/mL). Image area is 8×8 mm, and white scale bar is 1 mm long. Units for intensity bar inset are mV.

6.3.8 Depth Profiling of Biofilm Cross Sections.

Established cross sectioning methods in optical microscopy (Yu et al., 1994) allow chemical mapping of an antibiotic distribution as a function of biofilm depth. These cross sectioning methods were adapted here for use in MS imaging to allow membrane biofilms to be imaged in the plane they were sectioned. Trimethoprim at a concentration of 3.5 mM was allowed to equilibrate with the biofilms as previously described in Chapter 3. Figure 47 shows the MS image of a trimethoprim fragment (m/z 135 \pm 2) of a 150 μm wide, 25 μm thick slice of biofilm that was laid on its side onto a Si substrate. The optical image shows the biofilm (BF, dark gray) along the center and silicon substrate (Si, light gray) above and below the biofilm. Additional labels were included to show the biofilm-nutrient (anaerobic) interface and the biofilm-air (aerobic) interface. The polycarbonate membrane is located on the anaerobic side of the biofilm and not distinguishable in the optical image. The MS image of the antibiotic shows a non uniform distribution throughout the biofilm, with no preference for either nutrient or oxygen interface. This lateral resolution also corresponds to the depth resolution of the sample, so wider cross sections of biofilms would be preferred for this strategy.

Optimal cutting temperature (OCT) compound was used to fix the cross section shown in Figure 47 prior to microtoming, but it did not contribute to the ion signal (nor did a sample of OCT applied to a stainless steel plate show any LDPI-MS signal). The difficulties in using OCT as a plasticizer and fixing agent included maintaining an application of OCT as thin as possible. However, OCT did appear to reduce laser desorption efficiency and required the use of somewhat higher desorption powers.

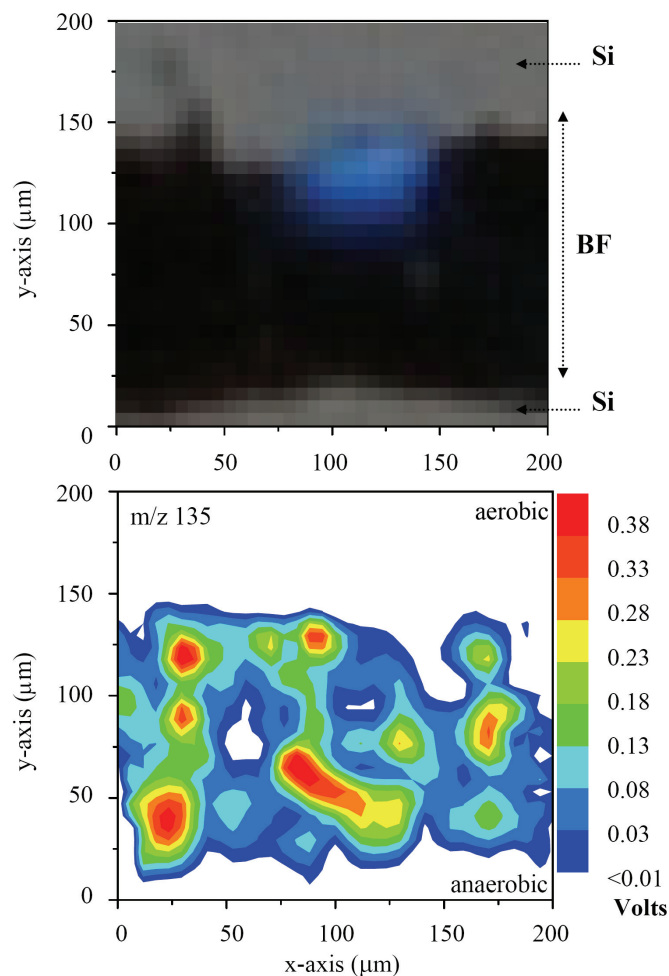


Figure 47: LDPI-MS image of trimethoprim doped biofilm cross section. LDPI-MS image of the m/z 135 ± 2 fragment a 3.5 mM trimethoprim doped biofilm cross section (image at bottom). Optical image of biofilm (top). Both images show cross sections with aerobic side of biofilm at top of frame and anaerobic side at bottom of frame. Scanning parameters were 200 $\mu\text{m}/\text{sec}$ vertical velocity with 10 μm horizontal steps.

6.3.9 Imaging Resolution, Speed, and Other Parameters.

Features in the MS image of Figure 47 were resolvable to ~ 30 μm , which was limited by the laser beam profile and mechanical vibrations. The desorption laser spot diameter was ~ 25 μm , as determined by microscopic observation of sample removed during the experiment. However, stage velocity and other instrumental parameters were also used to optimize MS image resolution. For example, the sectioned biofilm MS image of Figure 47 used scanning parameters

of 200 $\mu\text{m}/\text{sec}$ horizontal velocity with 10 μm vertical steps, with spectral averaging every ~ 14 μm . Thus, the small vertical step may have lead to some over-sampling here. The MS image in Figure 42 displays a resolution limited by the vertical step of 50 μm , compared with the optical image resolution of ~ 2 μm . In the case of Figure 48, a total of 32,500 spectra were collected in 100 min at an instrumental duty cycle of 100 Hz, covering an image area of 8×8 mm. At a stage velocity of 200 $\mu\text{m}/\text{sec}$ and 10 averages/spectrum, horizontal resolution was 20 μm between saved spectra, producing an image pixel of 20×50 μm .

MS imaging can be accomplished either spot-to-spot or by continuous motion sample scanning with respect to the desorption laser: continuous motion was employed here. Spot-to-spot sample scanning fires a given number of laser shots at a fixed point to permit signal averaging, then moves to a new spot, where the process is repeated until the entire target area is sampled. MS imaging was achieved here by rastering the laser at a continuous velocity horizontally across the surface in one direction, taking a vertical step, then continuing in the opposite horizontal direction. However, continuous motion sample scanning requires consideration of scanning velocity, laser repetition rate, and analyte decay. Characterizing the analyte decay in an experimental sample allows optimization of scanning parameters to reduce over-sampling during an imaging experiment. Prior work demonstrated that LDPI-MS can image a rifampicin antibiotic gradient in a biofilm grown on a polycarbonate membrane (Akhmetov et al., 2010), so a similar sample was used to evaluate scanning parameters. Analyte intensity of a prominent rifampicin fragment at m/z 298 ± 2 was monitored at twenty-two distinct spots on the biofilm, averaged, normalized, and plotted against time in Figure 48.

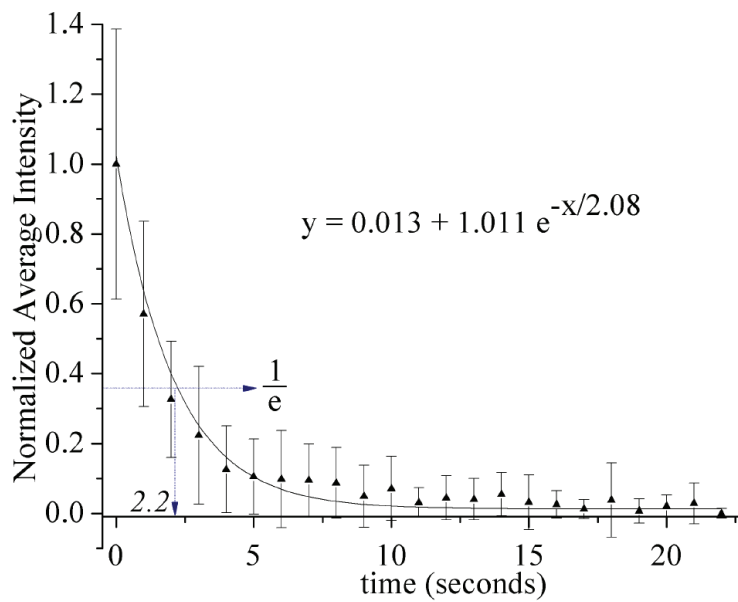


Figure 48: LPDI-MS signal decay of rifampicin doped membrane biofilm. Normalized signal decay at m/z 298 \pm 2 of rifampicin doped membrane biofilm resulting from averaging 22 analyte signal decays. Each decay study was performed at 5 Hz laser repetition rate. Equation is that of line fit to data points.

Several parameters were defined to determine the optimal scanning parameters without over-sampling by the desorption laser, whose diameter was defined as D on the sample. N was used to describe the number of laser shots before reaching $1/e$ of the maximum signal intensity from the analyte. The decay curve in Figure 48 shows that $1/e$ of the maximum analyte signal intensity in the biofilm occurred within ~ 2.2 sec when the laser repetition rate R was 5 Hz. Ignoring the unlikely possibility of rapid analyte diffusion within a dry sample in vacuum, N corresponded to ~ 11 laser shots.

The optimal parameters for translation stage motion were determined by combining the above signal decay measurements with simple geometric considerations. Rapid horizontal velocity of the translation stage was preferred to expedite sampling, but excessive velocity would lead to under-sampling that would reduce effective spatial resolution of the image. If G was the number of averaged spectra that were used to determine a single point on an image, then the

translation stage velocity V in $\mu\text{m}/\text{sec}$ was constrained by $D \cdot R/N \leq V \leq D \cdot R/G$ (thereby requiring $N \geq G$).

Recall that the translation stage motion was a zig-zag pattern which ran continuously in the horizontally direction, then made a discrete vertical step of size S followed by a reversal of continuous horizontal motion. A simple guideline for vertical step size S was that it should exceed the diameter of the desorption laser spot on the sample, D , to minimize the possibility of sampling damaged regions (Nemes et al., 2009). However, a less conservative approach attempted to compensate for the different overlap at the center versus the edge of each circular laser spot. Setting the vertical step $S \geq (D\sqrt{3})/2$ allows for improved resolution given the decay results of Figure 48.

The above analysis led to optimal parameters for vertical translation stage velocity $V \geq 200 \mu\text{m}/\text{sec}$ for laser repetition rate $R = 100 \text{ Hz}$ (effectively the maximum photoionization laser repetition rate available with this instrument) and desorption laser spot diameter $D \leq 20 \mu\text{m}$. Imaging rates of ~ 100 seconds per mm^2 were therefore possible when a horizontal raster step of $50 \mu\text{m}$ was used. Furthermore, it appears possible to optimize horizontal stage velocity, vertical step size, and number of spectra averaged per point such that $(D\sqrt{3})/2$ became the limiting feature for image resolution.

6.4 CONCLUSION

LDPI-MS imaging has been shown to be capable of characterizing the distribution of antibiotics within intact bacterial biofilms grown under nonshear colony biofilm and shear drop flow biofilm conditions. 7.87 eV LDPI-MS was used to detect several antibiotics neat and within intact biofilms grown both on membranes and by drip flow. Cross sectioning was used to depth

profile antibiotics within membrane biofilm slices with a depth resolution of $\sim 30 \mu\text{m}$. LDPI-MS produced images with a maximum resolution of $\sim 30 \mu\text{m}$ and a limit of detection of $\sim 20 \text{fmol}$. Addition of matrix enhanced parent ion signal by reducing fragmentation for the one antibiotic so tested, but did not increase overall ion signal. Prior LDPI-MS studies of antibiotics in biofilms indicates that the use of higher VUV photon energies will both enhance sensitivity and increase the variety of species detected, as seen in Chapter 4.

In the analysis of biological tissues, matrix-free techniques have the advantage of maintaining chemical and spatial integrity of the sample. However, addition of matrix demonstrated a ~ 10 fold enhancement in sensitivity for LDPI-MS for the single antibiotic examined here. Furthermore, matrix addition appeared to mostly reduce fragmentation of the parent ion at the expense of fragment ion signal. However, matrix crystal sizes that approach or exceed desorption laser beam diameter will also limit image resolution. Introduction of extraneous chemicals may contaminate or challenge the chemical and physiological integrity of samples (Malm et al., 2009). These disparities can compound existing ion suppression effects. MS images of matrix added to biofilm samples displayed signal fluctuations that reflect the method of matrix application and possibly also solvent migration effects. The modest signal enhancement and trade-offs of matrix addition indicate that further study is needed to determine if and when matrix addition is appropriate in LDPI-MS imaging.

ToF-SIMS was previously used to image lipid distributions relating the chemical composition to membrane shape in *T. thermophila* (Kurczy et al., 2010) SIMS images were acquired by rastering a 500 nm ion beam across a sample and resulted in image pixels of $\sim 1 \mu\text{m}^2$. It is clear that SIMS will provide much higher spatial resolution than either LDPI-MS or MALDI-MS. The $\sim 0.8 \mu\text{m}$ diameter cells of *S. epidermidis* would require a resolution of $\sim 50 \text{nm}$

to achieve a similar aspect ratio as *T. thermophila* by SIMS. However, such a high resolution is beyond the diffraction limit and currently unobtainable for laser desorption-based techniques. SIMS also typically displays more molecular fragmentation and lower high mass signal.

MALDI-MS imaging was used to show metabolic exchange between a co-culture of two strains of *Bacillus subtilis* (Liu et al., 2010). Image resolution was limited by the laser interval or spot-to-spot steps of $\sim 300\ \mu\text{m}$ (Yang et al., 2009). Matrix free laser desorption ionization MS of antibiotics released by symbiotic bacteria on insect cocoon surfaces achieved similar spatial resolution and sensitivity (Hölscher et al., 2009) to that reported here for LDPI-MS.

Depth profiling of biofilms via cross-sectioning was demonstrated here. Differences in antibiotic concentrations through the cross-section imply heterogeneities in cell densities or extracellular material that warrant further investigation. Lateral slicing is commonly used for depth profiling of animal tissue by MALDI-MS (Seeley and Caprioli, 2008; Chughtai and Heeren, 2010). However, unlike tissues, biofilms are often too thin or fragile to cross-section laterally.

Bacterial biofilms pose significant differences from other types of biological samples and present special issues for MS imaging. Animal and plant tissue typically display high structural segregation and cellular differentiation (Seeley and Caprioli, 2008; Chughtai and Heeren, 2010). MS imaging is enhanced by these discrete structural boundaries which often directly modulate ion signal. However, there is relatively little structural differentiation between microbes of the biofilms studied here which should differ only in metabolic activity. Biofilm growth techniques must also be considered when planning MS imaging experiments. Membrane biofilms produce thicker sessile films grown at the static interface of air-solid growth media. However, these polycarbonate membranes promote charging not only during LDPI-MS, but during MALDI-MS

and SIMS as well. Growth by drip flow occurs at a dynamic air-solid interface producing thinner and more robust biofilms. However, the drip flow method also displayed non-uniform channels of liquid nutrients flowing across the surface of the biofilm-substrate. Such heterogeneities indicate that future studies might move to different flow cell designs to grow more homogeneous biofilms.

LDPI-MS is a powerful technique coupled with imaging capabilities that compliments SIMS, MALDI-MS, and other MS imaging methods to characterize chemical distributions within biofilms. 7.87 eV LDPI-MS maintains selectivity to species with ionization energies near the photon energy while demonstrating depth profiling and imaging resolution at $\sim 30 \mu\text{m}$. The species detected can be expanded by increasing the photon energy (Hanley and Zimmerman, 2009) or via chemical tagging strategies (Akhmetov et al., 2010). Future work continues to improve the utility of LDPI-MS via higher photon energies, chemical tagging, further optimization of the ToF ion optics, and alternate matrix addition strategies.

CITED LITERATURE

- Adam, T., and Zimmermann, R.: Determination of single photon ionization cross sections for quantitative analysis of complex organic mixtures, Anal. Bioanal. Chem., 389:1941-1951, 2007.
- Akhmetov, A., Moore, J. F., Gasper, G. L., Koin, P. J., Hanley, L.: Laser desorption postionization for imaging MS of biological material, J. Mass Spectrom., 45:137-145, 2010.
- Altelaar, A.F.M, Taban, I.M., McDonnell, L.A., Verhaert, P.D.E.M, de Lange, R.P.J., Adan, R.A.H., Wolter J. Mooi, W.J., Heeren, R.M.A., Piersma, S.R.: High-resolution MALDI imaging mass spectrometry allows localization of peptide distributions at cellular length scales in pituitary tissue sections, International J. Mass Spectrom., 260:203–211, 2007.
- Bae, Y.J., Moon, J.H., Kim, M.S.: Expansion Cooling in the Matrix Plume Is under-Recognized in MALDI Mass Spectrometry. J. Amer. Soc. Mass Spectrom., 22:1070-1078, 2011.
- Baluya, D.L., Garrett, T.J., Yost, R.A.: Automated MALDI Matrix Deposition Method with Inkjet Printing for Imaging Mass Spectrometry, Anal. Chem., 79:6862-6867, 2007.
- Boesl, U.: Multiphoton Excitation and Mass-Selective Ion Detection for Neutral and Ion Spectroscopy. J. Phys. Chem., 95:2949-2962, 1991.
- Bridier, A., Dubois-Brissonnet, F., Greub, G., Thomas, V., Briandet, R.: Dynamics of the Action of Biocides in *Pseudomonas aeruginosa* Biofilms, Antimicrobial Agents and Chemotherapy, 55:2648–2654, 2011.
- Chan, K., Lanthier, P., Liu, X., Sandhu, J. K., Stanimirovic, D., Li, J.: MALDI mass spectrometry imaging of gangliosides in mouse brain using ionic liquid matrix, Anal. Chim. Acta, 639:57-61, 2009.
- Chen, Y., Allegood, J., Liu, Y., Wang, E., Cachón-González, B., Cox, T.M., Merrill, Jr. A.H., and Sullards, A.C.: Imaging MALDI Mass Spectrometry Using an Oscillating Capillary Nebulizer Matrix Coating System and Its Application to Analysis of Lipids in Brain from a Mouse Model of Tay-Sachs/Sandhoff Disease, Anal. Chem., 80:2780-2788, 2008.
- Chen, M.-C., Gerrity, M. R., Backus, S., Popmintchev, T., Zhou, X., Arpin, P., Zhang, X., Kapteyn, H. C., Murnane, M. M.: Spatially coherent, phase matched, high-order harmonic EUV beams at 50 kHz, Opt. Express, 17:17376-17383, 2009.
- Chen, Y. T., and Ling, Y. C.: Detection of water-soluble vitamins by matrix-assisted laser desorption/ionization time-of-flight mass spectrometry using porphyrin matrices, J. Mass Spectrom., 37:716-730, 2002.
- Chughtai, K., and Heeren, R.M.A.: Mass Spectrometric Imaging for Biomedical Tissue Analysis. Chem. Rev., 110:3237-3277, 2010.

- Cloud-Hansen, K. A., Peterson, S. B., Stabb, E. V., Goldman, W. E., McFall-Ngai, M. J., Handelsman, J.: Breaching the great wall: peptidoglycan and microbial interactions, Nat. Rev. Microbiol., 4:710-716, 2007.
- Coetser, S.E. and Cloete, T.E.: Biofouling and Biocorrosion in Industrial Water systems, Critical Reviews in Microbiology, 31:213 – 232, 2005.
- Dong F., Heinbuch, S., Rocca, J.J., and Bernstein, E.R.: Dynamics and fragmentation of van der Waals clusters: $(\text{H}_2\text{O})_n$, $(\text{CH}_3\text{OH})_n$, and $(\text{NH}_3)_n$ upon ionization by a 26.5 eV soft x-ray laser, J. Chem. Phys., 124:224319-1-17, 2006.
- Dong, F., Heinbuch, S., Xie, Y., Bernstein, E.R., Rocca, J.J., Wang, Z., Ding, X., He, H.: C=C Bond Cleavage on Neutral $\text{VO}_3(\text{V}_2\text{O}_5)_n$ Clusters, S. Am. Chem. Soc., 131:1057-1066, 2009.
- Dong, F., Heinbuch, S., Rocca, J.J., and Bernstein, E.R.: Single photon ionization of van der Waals clusters with a soft x-ray laser: $(\text{SO}_2)_n$ and $(\text{SO}_2)_n(\text{H}_2\text{O})_m$, J. Chem. Phys., 125:154317-1-9, 2006b.
- Dreisewerd, K.: The desorption process in MALDI. Chem. Rev., 103:395–425, 2003.
- Edirisinghe, P. D., Moore, J. F., Calaway, W. F., Veryovkin, I. V., Pellin, M.J., Hanley, L., Vacuum ultraviolet postionization of aromatic groups covalently bound to peptides. Anal. Chem., 78:5876–5883, 2006.
- Edirisinghe, P. D., Moore, J. F., Skinner-Nemec, K. A., Lindberg, C., Giometti, C. S., Veryovkin, I. V., Hunt, J. E., Pellin, M. J., Hanley, L.: Detection of In Situ Derivatized Peptides in Microbial Biofilms by Laser Desorption 7.87 eV Postionization Mass Spectrometry, Anal. Chem., 79:508-514, 2007.
- Esquenazi, E., Yang, Y.-L., Watrous, J., Gerwick, W. H., Dorrestein, P. C.: Visualizing the spatial distribution of secondary metabolites produced by marine cyanobacteria and sponges via MALDI-TOF imaging, Nat. Prod. Rep., 26:1521-570, 2009.
- Finch, J. W., Toerne, K. A., Schram, K. H., Denton, M. B.: Evaluation of a hydrogen laser vacuum ultraviolet source for photo-ionization mass spectrometry of pharmaceuticals. Rap. Commun. Mass Spectrom., 19:15–22, 2005.
- Flemming, H.-C., and Cloete, T.E. (2010): Environmental impact of controlling biofouling and biocorrosion in cooling water systems. In: Rajagopal, S., Jenner, H.A., Venugopalan, V.P. (eds.): Operational and Environmental Consequences of Large Industrial Cooling Water Systems.
- Flemming, H., and Wingender, J.: The biofilm matrix, Nat. Rev. Microbiol., 8:623-633, 2010.

- Fletcher, J.S., Henderson, A., Jarvis, R.M., Lockyer, N.P., Vickerman, J.C., Goodacre, R.: Rapid Discrimination of the Causal Agents of Urinary Tract Infection Using ToF-SIMS with Chemometric Cluster Analysis. Appl. Surf. Sci., 252:6869–6874, 2006.
- Fraud, S., Maillard, J.-Y., Denyer, S. P., Kaminski, M. A., Hanlon, G.W.: A simulated oral hygiene model to determine the efficacy of repeated exposure of amine oxide on the viability of *Staphylococcus mutans* biofilms. Eur. J. Oral Sci., 115:71–76, 2007.
- Galhena, A. S., Harris, G. A., Nyadong, L., Murray, K. K., Fernandez, F. M.: High-Throughput Small Molecule Ambient Mass Spectrometry Imaging by Infrared Laser Ablation Metastable-Induced Chemical Ionization, Anal. Chem., 82:2178-2181, 2010.
- Gamez, G., Zhu, L., Schmitz, T. A., Zenobi, R.: Photoelectron Emission as an Alternative Electron Impact Ionization Source for Ion Trap Mass Spectrometry, Anal. Chem., 80:6791-6795, 2008.
- Goeres, D.M., Hamilton, M.A., Beck, N.A., Buckingham-Meyer, K., Hilyard, J.D., Loetterle, L.R., Lorenz, L.A., Walker, D.K., Stewart, P.S.: A Method for Growing a Biofilm under Low Shear at the Air-Liquid Interface Using the Drip Flow Biofilm Reactor. Nat. Protocols., 4:783-788, 2009.
- Goodacre, R., Heald, J. K., Kell, D. B.: Characterisation of intact microorganisms using electrospray ionisation mass spectrometry, FEMS Microbiol. Lett., 176:17-24, 1999.
- Götz, F.: *Staphylococcus* and Biofilms. Mol. Microbiol. 43:1367-1378, 2002.
- Hankin, J. A., Barkley, R. M., Murphy, R. C.: Sublimation as a Method of Matrix Application for Mass Spectrometric Imaging, J. Am. Soc. Mass Spectrom., 18:1646-1652, 2007.
- Hanley, L., Edirisinghe, P.D., Calaway, W.F., Veryovkin, I.V., Pellin, M.J., Moore, J.F.: 7.87 eV postionization of peptides containing tryptophan or derivatized with fluorescein. Appl. Surf. Sci., 252:6723–6726, 2006.
- Hanley, L., and Zimmermann, R.: Light and Molecular Ions: The Emergence of Vacuum UV Single-Photon Ionization in MS, Anal. Chem., 81:4174-4182, 2009.
- Heeren, R. M. A., Smith, D. F., Stauber, J., Kükrer-Kaletas, B., Macaleese, L. A.: Imaging Mass Spectrometry: Hype or Hope?, J. Am. Soc. Mass Spectrom., 20:1006-1014, 2009.
- Heimann, P.A., Koike, M., Hsu, C.W., Blank, D., Yang, X.M., Suits, A.G., Lee, Y.T., Evans, M., Ng, C.Y., Flaim, C., Padmore, H.A.: Performance of the vacuum ultraviolet high-resolution and high-flux beamline for chemical dynamics studies at the Advanced Light Source. Rev. Sci. Instrum., 68:1945-1951, 1997.

- Heinbuch, S., Dong, F., Rocca, J.J., Bernstein, E.R.: Single photon ionization of hydrogen bonded clusters with a soft x-ray laser: $(\text{HCOOH})_x$ and $(\text{HCOOH})_y(\text{H}_2\text{O})_z$. J. Chem. Phys. 126:244301-1-11, 2007.
- Heinbuch, S., Dong, F., Rocca, J.J., Bernstein, E.R.: Single photon ionization of van der Waals clusters with a soft x-ray laser: $(\text{CO}_2)_n$ and $(\text{CO}_2)_n(\text{H}_2\text{O})_m$. J. Chem. Phys., 125:154316-1-7, 2006.
- Heinbuch, S., Grisham, M., Martz, D., Rocca, J.J.: Demonstration of a desk-top size high repetition rate soft x-ray laser based on a fast capillary discharge. Opt. Express., 13:4050-4055, 2005.
- Hexter, R.M.: X-Ray Microscopy of Thin Sections of Striated Muscle and of Polystyrene Microspheres. Proc. N.Y. Acad. Sci., 342:331-349, 1980.
- Hölscher, D., Shroff, R., Knop, K., Gottschaldt, M., Crecelius, A., Schneider, B., Heckel, D.G., Schubert, U.S., Svatoš, A.: Matrix-Free UV-Laser Desorption/Ionization (LDI) Mass Spectrometric Imaging at the Single-Cell Level: Distribution of Secondary Metabolites of *Arabidopsis Thaliana* and *Hypericum* Species. Plant J., 60:907-918, 2009.
- Huang, C.T., Xu, K.D., McFeters, G.A., Stewart, P.S.: Spatial patterns of alkaline phosphatase expression within bacterial colonies and biofilms in response to phosphate starvation. Appl. Environ. Microbiol., 64:1526–1531, 1998.
- Jackson, S. N., Wang, H. Y., Woods, A. S.: In Situ Structural Characterization of Phosphatidylcholines in Brain Tissue Using MALDI-MS/MS, J. Am. Soc. Mass Spectrom., 16:2052-2056, 2005.
- Jones, E.A., Lockyer, N.P., Vickerman, J.C.: Depth Profiling Brain Tissue Sections with a SIMS Method: 40 keV C60+ Primary Ion Beam, Anal. Chem., 80:2125-2132, 2008.
- Jorabchi, K., and Smith, L.M.: Single Droplet Separations and Surface Partition Coefficient Measurements Using Laser Ablation Mass Spectrometry, Anal. Chem., 81:9682–9688, 2009.
- Knochenmuss, R., and Zhigilei, L.V.: Molecular dynamics simulations of MALDI: laser fluence and pulse width dependence of plume characteristics and consequences for matrix and analyte ionization. J. Mass Spectrom., 45:333-346, 2010.
- Kraft, M.L., Weber, P.K., Longo, M.L., Hutcheon, I.D., Boxer, S.G.: Phase Separation of Lipid Membranes Analyzed with High-Resolution Secondary Ion Mass Spectrometry, Science, 313:1948-1951, 2006.
- Kriegeskotte, C., Cantz, T., Haberland, J., Zibert, A., Haier, J., Köhler, G., Schöler, H. R., Schmidt, H. H. J., Arlinghaus, H. F.: Laser secondary neutral mass spectrometry for copper detection in micro-scale biopsies, J. Mass Spectrom., 44:1417-1422, 2009.

- Kroiss, J., Kaltenpoth, M., Schneider, B., Schwinger, M.-G., Hertweck, C., Maddula, R.K., Strohm, E., Svatos, A.: Symbiotic Streptomyces Provide Antibiotic Combination Prophylaxis for Wasp Offspring. Nat. Chem. Biol., 6:261-263, 2010.
- Kudo, H., Cheng, K.J., Costerton, J.W.: Interactions between *Treponema bryantii* and cellulolytic bacteria in the in vitro degradation of straw cellulose. Can. J. Microbiol., 33:244-248, 1987.
- Kumar, J. K.: Lysostaphin: an antistaphylococcal agent, Appl. Microbiol. Biotechnol., 80:555-561, 2008.
- Kurczyk, M.E., Piehowski, P.D., Van Bell, C.T., Heien, M.L., Winograd, N., Ewing, A.G.: Mass Spectrometry Imaging of Mating Tetrahymena Show That Changes in Cell Morphology Regulate Lipid Domain Formation. Proc. Nat. Acad. Sci. U.S.A., 107:2751-2756, 2010.
- Latimer, J., Stokes, S.L., Graham, A.I., Bunch, J., Jackson, R.J., McLeod, C.W., Poole, R.K., A novel method for exploring elemental composition of microbial communities: Laser ablation-inductively coupled plasma-mass spectrometry of intact bacterial colonies, J. Microbiol. Meth., 79:329-335, 2009.
- Lechene, C., Luyten, Y., McMahon, G., Distel, D.L., Quantitative imaging of nitrogen fixation by individual bacteria within animal cells. Science, 317:1563-1566, 2007.
- Lemaire, R., Wisztorski, M., Desmons, A., Tabet, J.C., Day, R., Salzet, M., Fournier, I.: MALDI-MS Direct Tissue Analysis of Proteins: Improving Signal Sensitivity Using Organic Treatments, Anal. Chem., 78:7145-7153, 2006.
- Lewis, K.: Persister Cells. Ann. Rev. Microbiol., 64:357-372, 2010.
- Liang, X., Wang, A., Cao, T., Tang, H., McAllister, J. P., II, Salley, S. O., Ng, K. Y. S.: Effect of cast molded rifampicin/silicone on staphylococcus epidermidis biofilm formation, J. Biomed. Mater. Res., Part A., 76:580-588, 2006.
- Ling, Y. C., Lin, L., Chen, Y. T.: Quantitative Analysis of Antibiotics by Matrix assisted Laser Desorption/Ionization Time-of-flight Mass Spectrometry, Rapid Commun. Mass Spectrom., 12:317-327, 1998.
- Liu, W.-T., Yang, Y.-L., Xu, Y., Lamsa, A., Haste, N.M., Yang, J.Y., Ng, J., Gonzalez, D., Ellermeier, C.D., Straight, P.D., Pevzner, P.A., Pogliano, J., Nizet, V., Pogliano, K., Dorrestein, P.C.: Imaging Mass Spectrometry of Intraspecies Metabolic Exchange Revealed the Cannibalistic Factors of *Bacillus Subtilis*. Proc. Nat. Acad. Sci. U.S.A. 107:16286-16290, 2010.
- Lopez, D., Vlamakis, H., Kolter, R.: Biofilms. Cold Spring Harb. Perspect. Biol., 2:a000398-1-11, 2010.

- Malm, J., Giannaras, D., Riehle, M.O., Gadegaard, N., Sjøvall, P.: Fixation and Drying Protocols for the Preparation of Cell Samples for Time-of-Flight Secondary Ion Mass Spectrometry Analysis. Anal. Chem., 81:7197-7205, 2009.
- Marksteiner, M., Haslinger, P., Sclafani, M., Ulbricht, H., Arndt, M.: UV and VUV ionization of organic molecules, clusters and complexes, J. Phys. Chem. A., 113:9952-9957, 2009.
- McDonnell, L.A., and Heeren, R.M.A.: Imaging mass spectrometry, Mass Spectrom. Rev., 26:606– 643, 2007.
- McLean, J. A., Stumpo, K. A., Russell, D. H.: Size-Selected (2-10 nm) Gold Nanoparticles for Matrix Assisted Laser Desorption Ionization of Peptides, J. Am. Chem. Soc., 127:5304-5305, 2005.
- Méndez-Vilas, A., Gallardo-Moreno, A.M., González-Martín, M.L., Calzado-Montero, R., Nuevo, M.J., Bruque, J.M., Pérez-Giraldo, C.: Surface characterisation of two strains of *Staphylococcus epidermidis* with different slime-production by AFM, Appl. Surf. Sci., 238:18–23, 2004.
- Milasinovic, S., Liu, Y., Gasper, G.L., Zhao, Y., Johnston, J.L., Gordon, R.J., Hanley, L.: Ultrashort pulse laser ablation for depth profiling of bacterial biofilms, J. Vac. Sci. Technol., A., 28:647-651, 2010.
- Moore, J.F., Gasper, G., Akhmetov, A., Hanley, L. In A Serpentine Extraction Ion Source for a Laser Desorption Postionization Microprobe Imaging MS, 58th ASMS Conference on Mass Spectrometry and Allied Topics, Salt Lake City, UT, May 23 - 28, 2010; Salt Lake City, UT, 2010.
- Murphy, R. C., Hankin, J. A., Barkley, R. M.: Imaging of lipid species by MALDI mass spectrometry, J. Lipid Res., 50:S317-S322, 2009.
- Musk, D.J.J., and Hergenrother, P.J.: Chemical Countermeasures for the Control of Bacterial Biofilms: Effective Compounds and Promising Targets. Curr. Medic. Chem. 13:2163-2177, 2006.
- Nemes, P., Barton, A.A., Vertes, A.: Three-Dimensional Imaging of Metabolites in Tissues under Ambient Conditions by Laser Ablation Electrospray Ionization Mass Spectrometry. Anal. Chem., 81:6668-6675, 2009.
- Nemes, P., Woods, A. S., Vertes, A.: Simultaneous Imaging of Small Metabolites and Lipids in Rat Brain Tissues at Atmospheric Pressure by Laser Ablation Electrospray Ionization Mass Spectrometry, Anal. Chem., 82:982-988, 2010.
- Nuutinen, J.M.J., Ratilainen, J., Rissanen, K., Vainiotalo, P.: Mass spectrometric studies on small open-chain piperazine-containing ligands and their transition metal complexes, J. Mass Spectrom., 36:902-910, 2001.

- O’Gara.: *Staphylococcus epidermidis* biofilms: importance and implications, J. Med. Microbiol., 50:582 – 587, 2001.
- Ostrowski, S.G., van Bell, C.T., Winograd, N., Ewing, A.G.: Mass spectrometric imaging of highly curved membranes during *Tetrahymena* mating. Science, 305:71–73, 2004.
- Otto, M.: *Staphylococcus epidermidis* - the ‘accidental’ pathogen, Nat. Rev. Microbiol., 7:555–567, 2009.
- Pallix, J.B., Schuhle, U., Becker, C.H., Huestis, D.L.: Advantages of Single-Photon Ionization over Multiphoton Ionization for Mass Spectrometric Surface Analysis of Bulk Organic Polymers, Anal. Chem., 61:811-819, 1989.
- Planchon, S., Desvaux, M., Chafsey, I., Chambon, C., Leroy, S., Hébraud, M., Talon, R.: Comparative Subproteome Analyses of Planktonic and Sessile *Staphylococcus xylosum* C2a: New Insight in Cell Physiology of a Coagulase-Negative *Staphylococcus* in Biofilm, J. Proteom. Res., 8:1797–1809, 2009.
- Pradier, C.M., Rubio, C., Poleunis, C., Bertrand, P., Marcus, P., Compère, C.: Surface Characterization of Three Marine Bacterial Strains by Fourier Transform Ir, X-Ray Photoelectron Spectroscopy, and Time-of-Flight Secondary-Ion Mass Spectrometry, Correlation with Adhesion on Stainless Steel Surfaces. J. Phys. Chem. B, 109:9540-9549, 2005.
- Puolitaival, S.M., Burnum, K.E., Cornett, D. S., Caprioli, R.M.: Solvent-free matrix dry-coating for MALDI imaging of phospholipids, J. Am. Soc. Mass Spectrom., 19:882-886, 2008.
- Rais, R., Gonzalez, P.M., Zheng, X., Wring, S.A., Polli, J.E.: Method to screen substrates of apical sodium-dependent bile acid transporter, AAPS J., 10:596-605, 2008.
- Ray, R., Lizewski, S., Fitzgerald, L.A., Little, B., Ringeisen, B.R.: Methods for imaging *Shewanella oneidensis* MR-1 nanofilaments, J. Microbiol. Meth., 82:187–191, 2010.
- Reyzer, M.L., and Caprioli, R.M.: MALDI-MS-based imaging of small molecules and proteins in tissues. Curr. Opin. Chem. Biol., 11:29–35, 2007.
- Richards, G.K., Prentis, J., Gagnon, R.F. : Antibiotic activity against *Staphylococcus epidermidis* biofilms in dialysis fluids. Adv. Perit. Dial., 5:133-137, 1989.
- Sampson, J.S., and Muddiman, D.C.: Atmospheric pressure infrared (10.6mm) laser desorption electrospray ionization (IR-LDESI) coupled to a LTQ Fourier transform ion cyclotron resonance mass Spectrometer, Rapid Commun. Mass Spectrom., 23:1989–1992, 2009.

- Seeley, E.H., and Caprioli, R.M.: Molecular Imaging of Proteins in Tissues by Mass Spectrometry. Proc. Nat. Acad. Sci., U.S.A., 105:18126-18131, 2008.
- Shank, E. A., and Kolter, R.: New developments in microbial interspecies signaling, Curr. Opin. Microbiol., 12:205-214, 2009.
- Shiea, J., Yuan, C., Huang, M., Cheng, S., Ma, Y., Tseng, W., Chang, H., Hung, W.: Detection of Native Protein Ions in Aqueous Solution under Ambient Conditions by Electrospray Laser Desorption/Ionization Mass Spectrometry, Anal. Chem., 80:4845–4852, 2008.
- Shimma, S., Sugiura, Y., Hayasaka, T., Hoshikawa, Y., Noda, T., Setou, M.: MALDI-based imaging mass spectrometry revealed abnormal distribution of phospholipids in colon cancer liver metastasis, J. Chromatogr., B., 855:98-103, 2007.
- Siegal, M. M., Tabei, K., Tsao, R., Pastel, M. J., Pandey, R. K., Berkenkamp, S., Hillenkamp, F., de Vries, M. S.: Comparative mass spectrometric analyses of Photofrin oligomers by fast atom bombardment mass spectrometry, UV and IR matrix-assisted laser desorption/ionization mass spectrometry, electrospray ionization mass spectrometry and laser desorption/jet-cooling photoionization mass spectrometry, J. Mass Spectrom., 34:661-669, 1999.
- Smirnov, P., Zhu, X., Taylor, T., Huang, Y., Ross, P., Papayanopoulos, I.A., Martin, S.A., Pappin, D.J.: Suppression of a-Cyano-4-Hydroxycinnamic Acid Matrix Clusters and Reduction of Chemical Noise in MALDI-ToF Mass Spectrometry. Anal. Chem., 76:2958-2965, 2004.
- Sousa, C., Teixeira, P., Oliveira, R.: The role of extracellular polymers on Staphylococcus epidermidis biofilm biomass and metabolic activity, J. Basic Microbiol., 49:363-370, 2009.
- Stewart, P.S., Rayner, J., Roe, F., Rees, W.M.: Biofilm Penetration and Disinfection Efficacy of Alkaline Hypochlorite and Chlorosulfamates. J. Appl. Microbiol., 91:525-532, 2001.
- Stewart, P.S.: Diffusion in Biofilms. J. Bacteriol., 185:1485-1491, 2003.
- Stewart, P. S., Mukherjee, P. K., Ghannoum, M., Biofilm antimicrobial resistance. in: Ghannoum, M., O’Toole, G. A. (Eds.), Microbial Biofilms, ASM Press, Washington, D.C. 2004, pp. 250–268.
- Stewart, P.S., and Franklin, M.J.: Physiological Heterogeneity in Biofilms. Nat. Rev. Microbiol., 6:199-210, 2008.
- Stoeckli, M., Staab, D., Schweitzer, A., Compound and metabolite distribution measured by MALDI mass spectrometric imaging in whole-body tissue sections. Inter. J. Mass Spectrom., 260:195–202, 2007.

- Straight, P.D., and Kolter, R.: Interspecies Chemical Communication in Bacterial Development. Ann. Rev. Microbiol., 63:99-118, 2009.
- Su, C. L., and Tseng, W. L.: Gold Nanoparticles as Assisted Matrix for Determining Neutral Small Carbohydrates through Laser Desorption/Ionization Time-of-Flight Mass Spectrometry, Anal. Chem., 79:1626-33, 2007.
- Sugiura, Y., Konishi, Y., Zaima, N., Kajihara, S., Nakanishi, H., Taguchi, R., Setou, M.: Visualization of the cell-selective distribution of PUFA-containing phosphatidylcholines in mouse brain by imaging mass spectrometry, J. Lipid Res., 50:1776-1788, 2009.
- Sugiura, Y., Shimma, S., Setou, M.: Two-Step Matrix Application Technique To Improve Ionization Efficiency for Matrix-Assisted Laser Desorption/Ionization in Imaging Mass Spectrometry, Anal. Chem., 78:8227-8235, 2006.
- Svatoš, A.: Mass spectrometric imaging of small Molecules, Trends Biotechnol., 28:425-434, 2010.
- Swoboda, J. G., Campbell, J., Meredith, T. C., Walker, S.: Wall Teichoic Acid Function, Biosynthesis, and Inhibition, Chem. Bio. Chem., 11:35-45, 2010.
- Takahashi, L. K., Zhou, J., Wilson, K. R., Leone, S. R., Ahmed, M.: Imaging with Mass Spectrometry: A Secondary Ion and VUV-Photoionization Study of Ion-Sputtered Atoms and Clusters from GaAs and Au, J. Phys. Chem. A., 113: 4035-4044, 2009.
- Thiel, V., Heim, C., Arp, G., Hahmann, U., Sjövall, P., Lausmaa, J.: Biomarkers at the Microscopic Range: ToF-SIMS Molecular Imaging of Archaea-Derived Lipids in a Microbial Mat. Geobiol., 5:413-421, 2007.
- Thomas, J.G., Ramage, G., Lopez-Ribot, J.L.: Biofilms and implant infections. in: Ghannoum, M., O'Toole, G. A. (Eds.), Microbial Biofilms, ASM Press, Washington, D.C. 2004, pp. 269-293.
- Todd, P.J., Schaaff, T.G., Chaurand, P., Caprioli, R.M.: Organic ion imaging of biological tissue with secondary ion mass spectrometry and matrix-assisted laser desorption/ionization. J. Mass Spectrom., 36:355-369, 2001.
- Tong, H., Bell, D., Tabei, K., Siegel, M.M.: Automated data massaging, interpretation, and e-mailing modules for high throughput open access mass spectrometry, J. Am. Soc. Mass Spectrom., 10:1174-1187, 1999.
- Tyler, B.J., Rangarajan, S., Möller, J., Beumer, A., Arlinghaus, H.F.: ToF-Sims Imaging of Chlorhexidine-Digluconate Transport in Frozen Hydrated Biofilms of the Fungus *Candida Albicans*. Appl. Surf. Sci., 252:6712-6715, 2006.

- Vaidyanathan, S., Fletcher, J.S., Goodacre, R., Lockyer, N.P., Micklefield, J., Vickerman, J.C.: Subsurface Biomolecular Imaging of *Streptomyces Coelicolor* Using Secondary Ion Mass Spectrometry. Anal. Chem., 80:1942-1951, 2008.
- Végvári, Á., Fehniger, T.E., Gustavsson, L., Nilsson, A., Andrén, P.E., Kenne, K., Nilsson, J., Laurell, T., Marko-Varga, G.: Essential Tactics of Tissue Preparation and Matrix Nano-Spotting for Successful Compound Imaging Mass Spectrometry. J. Proteom., 73:1270-1278, 2010.
- Vogel, A., Venugopalan, V.: Mechanisms of Pulsed Laser Ablation of Biological Tissues. Chem. Rev., 103:577-644, 2003.
- Wagner, M.: Single-Cell Ecophysiology of Microbes as Revealed by Raman Microspectroscopy or Secondary Ion Mass Spectrometry Imaging. Ann. Rev. Microbiol., 63:411-429, 2009.
- Walsh, C. Antibiotics: Actions, Origins, Resistance; ASM Press: Washington, DC, 2003.
- Watrous, J., Hendricks, N., Meehan, M., Dorrestein, P.C.: Capturing bacterial metabolic exchange using thin film desorption electrospray ionization-imaging mass spectrometry, Anal. Chem. 82:1598-15600, 2010.
- Watrous, J.D., Alexandrov, T., Dorrestein, P.C.: The Evolving Field of Imaging Mass Spectrometry and Its Impact on Future Biological Research. J. Mass Spectrom., 46:209-222, 2011.
- Wei, J., Buriak, J.M., Siuzdak, G.: Desorption/ionization mass spectrometry on porous silicon. Nature, 399:243–246, 1999.
- Wilkins, C. L., Lay, J. O.: Identification of Microorganisms by Mass Spectrometry, Wiley, New York, 2006.
- Willingham, D., Brenes, D.A., Wucher, A., Winograd, N.: Strong-field Photoionization of Sputtered Neutral Molecules for Molecular Depth Profiling. J. Phys. Chem. C., 114:5391-5399, 2010.
- Wurz, P., and Lykke, K.R., Multiphoton Excitation, Dissociation, and Ionization of C60. J. Phys. Chem., 96: 10129-10149, 1992.
- Xu, K.D., Stewart, P.S., Xia, F., Huang, C.T., McFeters, G.A.: Spatial physiological heterogeneity in *Pseudomonas aeruginosa* biofilm is determined by oxygen availability. Appl. Environ. Microbiol., 64:4035–4039, 1998.
- Yang, Y.-L., Xu, Y., Straight, P., Dorrestein, P.C.: Translating Metabolic Exchange with Imaging Mass Spectrometry. Nat. Chem. Biol., 5:885-887, 2009.

Yu, F.P., Callis, G.M., Stewart, P.S., Griebe, T., McFeters, G.A.: Cryosectioning of Biofilms for Microscopic Examination. Biofoul., 8:85-91, 1994.

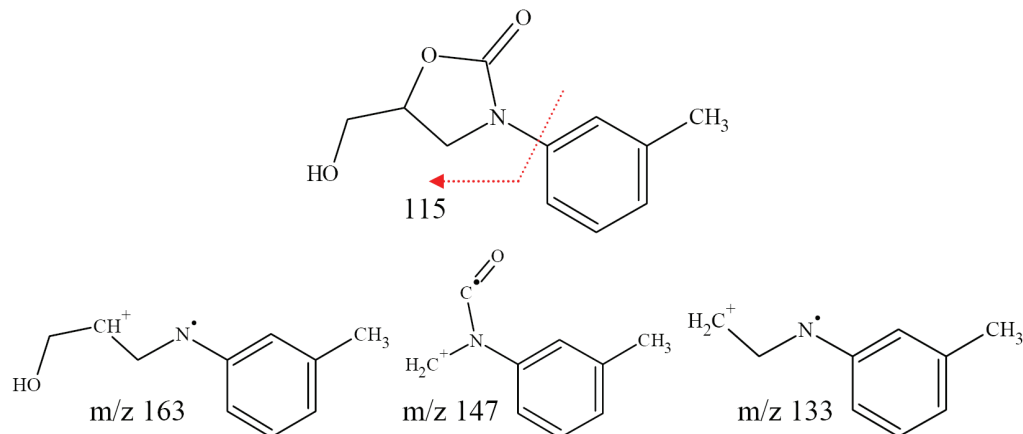
Zheng, Z., and Stewart, P.S.: Penetration of Rifampin through *Staphylococcus epidermidis* Biofilms. Antimicrob. Agents Chemother., 46:900-903, 2002.

Zhou, J., Takahashi, L.K., Wilson, K.R., Leone, S.R., Ahmed, M.: Internal Energies of Ion Sputtered Neutral Tryptophan and Thymine Molecules Determined by Vacuum Ultraviolet Photoionization. Anal. Chem., 82:3905-3913, 2010.

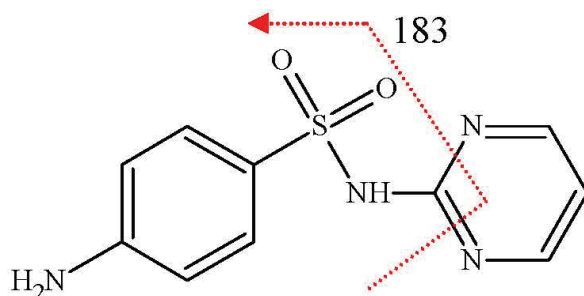
Zhou, M., Wu, C., Akhmetov, A., Edirisinghe, P.D., Drummond, J.L., Hanley, L.: 7.87 eV laser desorption postionization mass spectrometry of adsorbed and covalently bound bisphenol A diglycidyl methacrylate. J. Am. Soc. Mass Spectrom., 18:1097–1108, 2007.

APPENDIX A. Antibiotic chemical structures and fragmentation

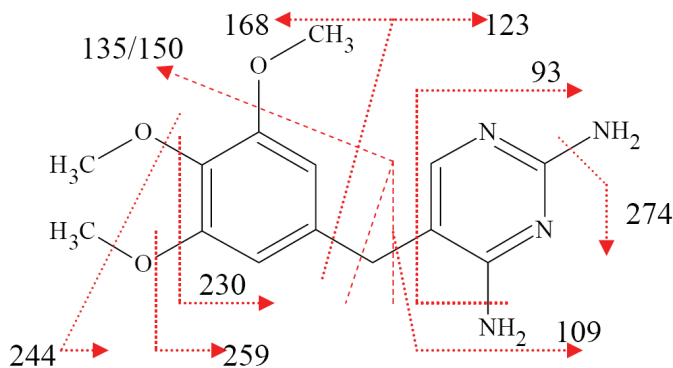
The proceeding text and Figures (A1 – A12) provide further discussion of Table 2 (Chapter 6) and fragmentation patterns for the various antibiotics.



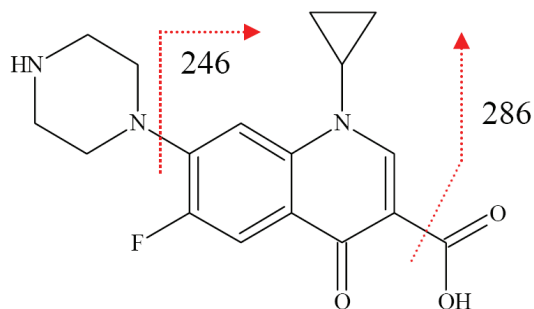
A1. Toloxatone (M.W. 207 Da) fragments via internal fragmentation of the five-membered oxazolidine group.



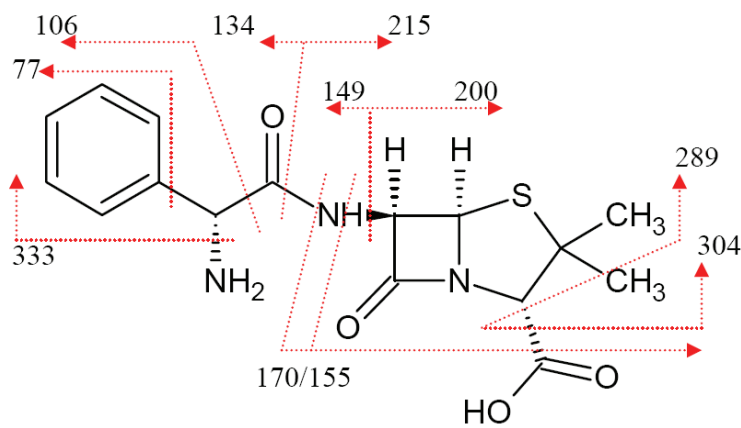
A2. Sulfadiazine (250 Da) showed two major fragments. The source of the m/z 183 peak is shown above. The peak at m/z 210 was not identified.



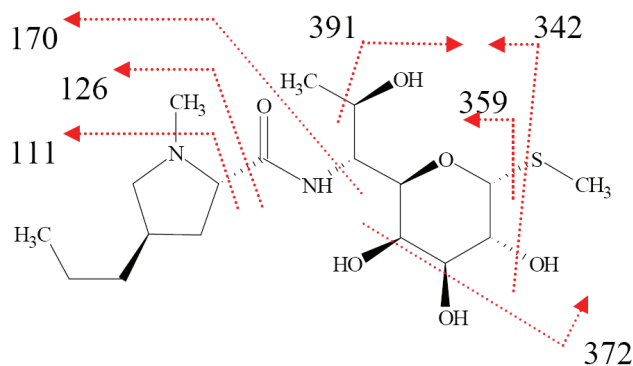
A3. Trimethoprim (290 Da) fragmentation did not break the pyrimidine ring and mainly comprised various combinations of methyl and methoxy loss.



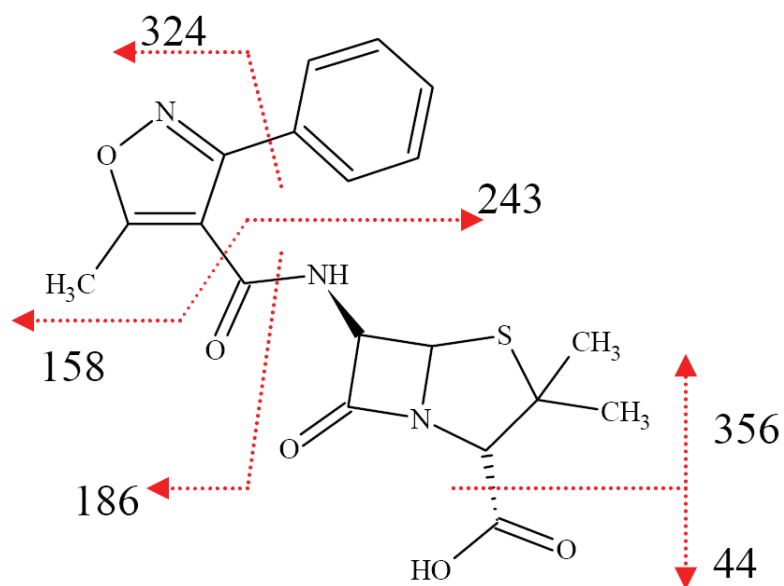
A4. Ciprofloxacin (331 Da) was stable with only a carboxylic acid and piperazine loss.



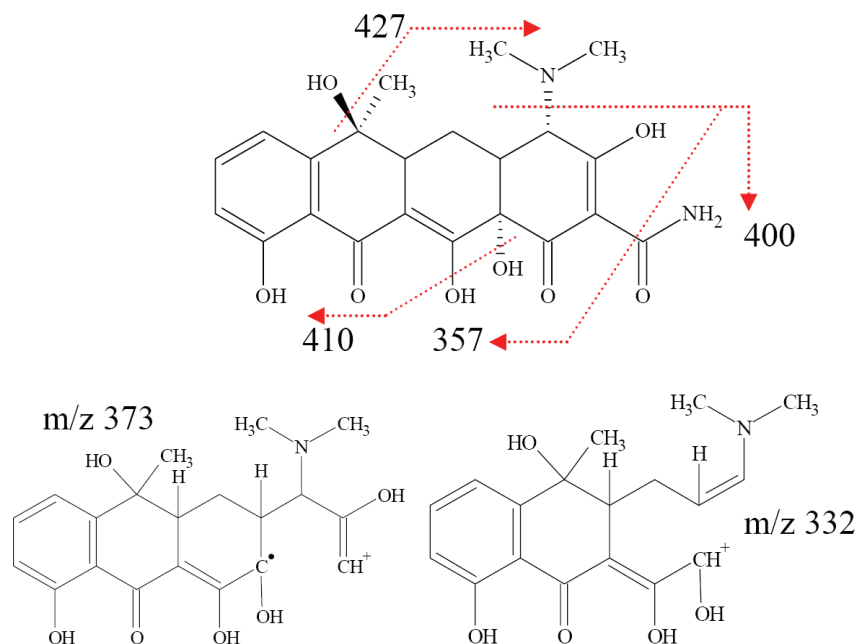
A5. Ampicillin (349 Da) fragmentation was accompanied by pathways that did not break the beta-lactam ring. Ampicillin fragmented around the beta-lactam with fragments at m/z 215, 200, 170, 155, along with combined losses of carboxylic acid and methyl (m/z 304, 289). Aside from a loss of amine (m/z 333), other peaks resulted from the fragmentation between the beta-lactam and the phenyl group (m/z 149, 134, 106, 77).



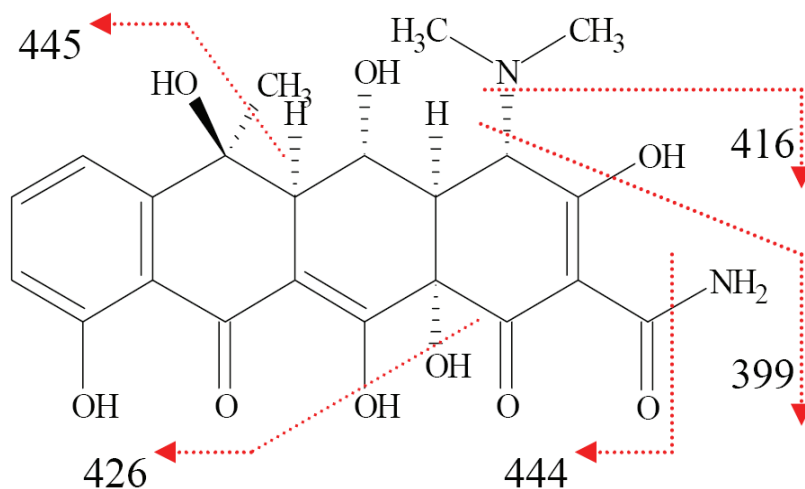
A6: Lincomycin (406 Da) had corresponding fragments due to combinations of methyl, hydroxyl, and methylsulfanyl loss, and breaks between the 5-membered pyrrolidine ring and 6-membered cyclic ether.



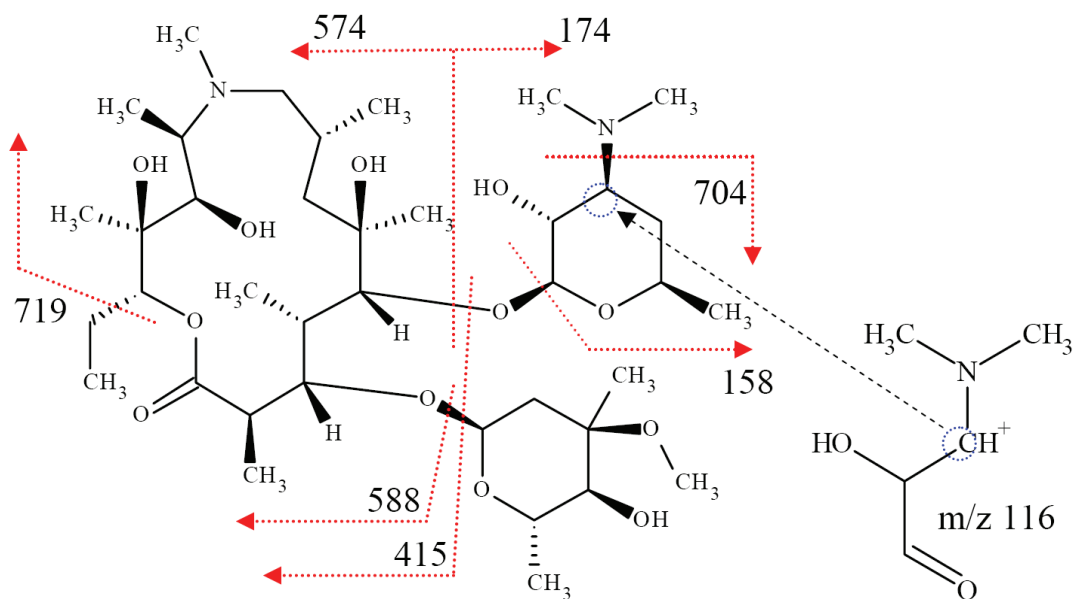
A7: Oxacillin (401 Da) had corresponding fragments due to the loss of carboxylic acid and phenyl loss, a break between benzylic 5-membered ring and the beta-lactam at either side of the carbonyl group.



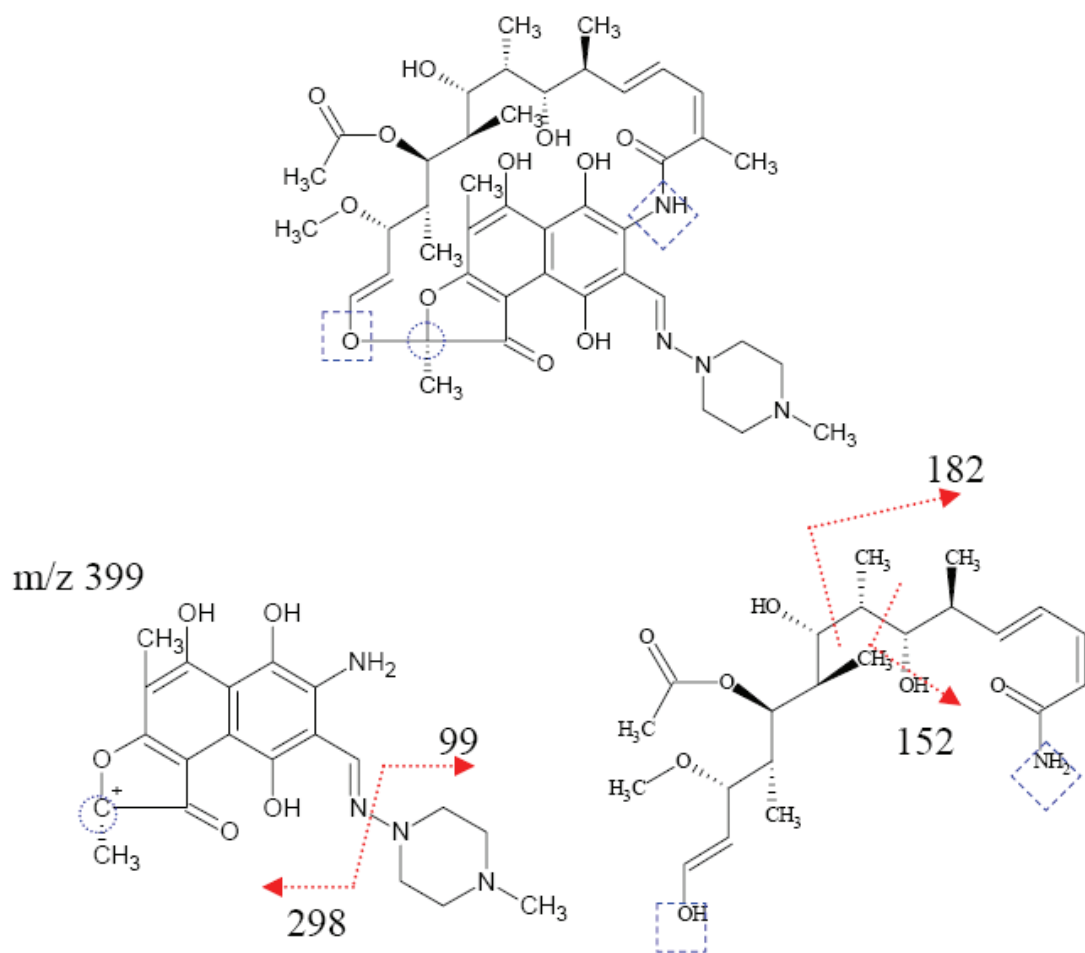
A8: Tetracycline (444 Da) fragments were the result of combinations of methyl, hydroxyl, amide and dimethyl amide losses.



A9: Oxytetracycline (460 Da) fragments similarly to tetracycline.

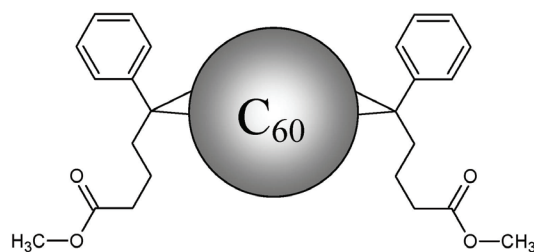


A10: Azithromycin (748 Da) preserved its 15-membered N-substituted lactone ring and fragmented mainly by loss of its two sugars.



A11: Rifampicin (823 Da) showed major fragments due to loss of methylated piperazine, and the 17-membered linear portion from the three fused rings.

Coumermycin A1 peaks were assigned from the literature except for the unidentified peaks at m/z 265 and 125. As shown in the neat spectra, ampicillin and oxacillin both contain β -lactams which undergo extensive fragmentation making them less suitable for biofilm studies.



A12: [6,6] diphenyl C_{60} bis(butyric acid methyl ester) (1100 Da) showed fragmentation of ligands (m/z 190) to produce peaks at m/z 910 $[M-L]^+$, 720, C_{60} , $[M-2L]^+$, and 190.

CIRRICULUM VITA

GERALD L. GASPER

OBJECTIVE

Obtain an industrial post doctoral position applying novel methods in MS imaging.

EDUCATION

Doctor of Philosophy in Analytical Chemistry, University of Illinois at Chicago, 2011

Title: MS Imaging of Antibiotics within Bacterial Biofilms by Laser Desorption Postionization.

Master of Science in Chemistry, University of Illinois at Chicago, awarded 2007

Bachelor of Science in Chemistry, University of Illinois at Chicago, awarded 2005

QUALIFACTION SUMMARY

- Experience in applied research environment developing analytical instrumentation.
- Experience with LC/MS applications.
- Effective problem solving of MS instrumentation through dedicated troubleshooting.
- Over four years of applied experience with CAD for mechanical design.
- Supervisory experience of graduate and undergraduate researchers.
- Extensive knowledge and maintenance of surface analysis techniques and vacuum systems such as: MALDI-MS, SIMS, LDPI-MS, SNMS, SPI.
- Operational knowledge of analytical instrumentation: HPLC, GCMS, ESI/APCI/APPI, XPS, SEM, DESI, LA-ICP-MS, FTIR, TPD, XRD.
- Outstanding written and verbal communication.
- Demonstrated success through publications and presentations.

SKILLS

Mechanical drafting, Analytical method development, Method validation, Multivariate analysis by PCA

Software: AutoCAD, Origin8.0, MatLab, Rhino4.0, SIMION 8, LabView, ChemDraw, Gaussian

ACADEMIC and RESEARCH POSITIONS

Research Assistant, Analytical | 2006 - present | University of Illinois at Chicago | Chicago, IL

- Developed imaging MS instrumentation to probe small molecule distribution in *Staphylococcus epidermidis*.
- Senior draftsman of CAD designs for manufacturing of custom-built mechanical hardware for instruments.
- Oversaw vacuum equipment through regularly scheduled maintenance, repairs, and updates.
- Initiated building of Hanley Biofilm Laboratory by acquiring certificates, equipment, and supplies.
- Trained graduate and undergraduate group members on instruments, protocols, and software packages.
- Published papers and presented work at scientific conferences.

Synchrotron User | 2009 - 2010 | Lawrence Berkeley National Laboratory | Berkeley, CA

- Characterized small molecules in biological systems with tunable VUV and EUV synchrotron radiation.
- Tested hybridized systems using molecular ion beams, laser desorption, and synchrotron ionization.
- Published papers and presented work at scientific conferences.

Biofilm Research Assistant | 2006 | Center for Biofilm Engineering, Montana State | Bozeman, MT

- Practiced methods to grow bacterial biofilms of *Staphylococcus epidermidis*.

Teaching Assistant Coordinator | 2005 - 2006 | University of Illinois at Chicago | Chicago, IL

- Oversaw teaching assistants.
- Prepared experiments for teaching laboratories.

Undergraduate Analytical/Physical Chemistry Research | 2004 - 2005 | University of Illinois at Chicago

- Produced model collagen substrates for laser damage analysis studies.
- Characterized laser damage by z-scans of pulsed femtosecond laser with phase contrast microscope.

Undergraduate Research, Department of Mathematics | 2002 | University of Illinois at Chicago

- Developed statistical algorithm to tabulate letter frequency from English, Italian, and Spanish literature.
- Produced fourth-order word generator from statistical tables of English, Italian, and Spanish literature.

PUBLICATIONS

Brominated Tyrosine and Polyelectrolyte Multilayer Analysis by Laser Desorption VUV Postionization and Secondary Ion Mass Spectrometry. M. Blaze M.T, L.K. Takahashi, J. Zhou, M. Ahmed, G.L. Gasper, F.D. Pleticha, L. Hanley. *Analytical Chemistry, ASAP*.

MS Imaging of Antibiotics Distribution and Uptake within Bacterial Biofilms by 7.87 eV Laser Desorption Postionization. G.L. Gasper, J.F. Moore, A. Akhmetov, B.A. Sevinc, M. Blaze, Y. Cui, L. Hanley. *Submitted to Journal of the American Society for Mass Spectrometry, 5/30/11*.

Comparing Vacuum and Extreme Ultraviolet Radiation for Postionization of Laser Desorbed Neutrals from Bacterial Biofilms and Organic Fullerenes. G.L. Gasper, L.K. Takahashi, J. Zhou, M. Ahmed, J.F. Moore, L. Hanley. *Nuclear Instrumentation and Methods A*. 2011, doi:10.1016/j.nima.2010.12.024.

Laser Desorption Postionization Mass Spectrometry of Antibiotic-Treated Bacterial Biofilms Using Tunable Vacuum Ultraviolet Radiation. G.L. Gasper, L.K. Takahashi, J. Zhou, M. Ahmed, J.F. Moore, L. Hanley. *Anal. Chem.* 2010, 82, 7472-7478.

Ultrashort Pulse Laser Ablation for Depth Profiling of Bacterial Biofilms. S. Milasinovic, Y. Liu, G.L. Gasper, Y. Zhao, J.L. Johnston, R.J. Gordon, L. Hanley., *Journal of Vacuum Science and Technology A*. 2010, 28, 647-651.

Laser Desorption Postionization for Imaging MS of Biological Material. A. Akhmetov, J.F. Moore, G.L. Gasper, P.J. Koin, L. Hanley. *Journal of Mass Spectrometry*. 2010, 45, 137-145.

Laser Desorption 7.87 eV Postionization Mass Spectrometry of Antibiotics in *Staphylococcus epidermidis* Bacterial Biofilms. G.L. Gasper, R. Carlson, A. Akhmetov, J.F. Moore, L. Hanley. *Journal of Proteomics*. 2008, 8, 3816-3821.

AWARDS

Baxter Innovation Award, 2009

Graduate College Presenters Award: 2008, 2009, and 2010, University of Illinois at Chicago

Graduate Student Council Travel Award: 2008, 2009, and 2010, University of Illinois at Chicago

Department of Mathematics, VIGRE Research Award, 2002, University of Illinois at Chicago

AFFILIATIONS AND SCHOLARLY ACTIVITIES

American Society for Mass Spectrometry (ASMS)

AVS Science and Technology Society

Chicago Mass Spectrometry Discussion Group (CMSDG)

Midwest Microscopy and Microanalysis Society (M3S)

Society of Applied Spectroscopy (SAS), Chicago Chapter

PRESENTATIONS

Baxter, Round Lake, IL 2011.

MS Imaging of Antibiotics within Bacterial Biofilms by Laser Desorption Postionization.

Pacific Northwest National Laboratory, Richland, WA, 2011.

MS Imaging of Antibiotics within Bacterial Biofilms by Laser Desorption Postionization.

Baxter, Innovation Award Presentation, Deerfield, IL, 2009.

Imaging Mass Spectrometry of Antibiotics in *Staphylococcus epidermidis* Bacterial Biofilms by Laser Desorption 7.87 eV Postionization.

PITTCON, Chicago, IL, 2009

Imaging Mass Spectrometry of Antibiotics in *Staphylococcus epidermidis* Bacterial Biofilms using Laser Desorption 7.87 eV Postionization. G.L. Gasper, R. Carlson, A. Akhmetov, J.F. Moore, P. Lu, A.V. Walker, L. Hanley.

Chicago Biomedical Consortium, Chicago, IL, 2007.

Laser Desorption Vacuum Ultraviolet Postionization Mass Spectrometry of Antibiotics in Bacterial Biofilms. G.L. Gasper, A. Akhmetov, R. Carlson, L. Hanley.

Poster Presentations

16th Pan-American Synchrotron Radiation Instrumentation Conf., Argonne National Laboratory, Chicago, IL, 2010.

Comparing VUV and EUV Radiation for Postionization of Laser Desorbed Neutrals from Bacterial Biofilms and Organic Compounds. G.L. Gasper, L.K. Takahashi, J. Zhou, M. Ahmed, J.F. Moore, L. Hanley.

American Society of Mass Spectrometry, Salt Lake City, UT, 2010.

Tunable Postionization of Laser Desorbed Neutrals by Synchrotron Radiation to Detect Antibiotics in *Staphylococcus epidermidis* Bacterial Biofilms. G.L. Gasper, L.K. Takahashi, J. Zhou, M. Ahmed, L. Hanley.

American Society of Mass Spectrometry, Philadelphia, PA, 2009.

Imaging Mass Spectrometry of Antibiotics in *Staphylococcus epidermidis* Bacterial Biofilms using Laser Desorption 7.87 eV Postionization. G.L. Gasper, R. Carlson, A. Akhmetov, J.F. Moore, L. Hanley.

American Society of Mass Spectrometry, Denver, CO, 2008.

Laser Desorption 7.87 eV Postionization Mass Spectrometry of Antibiotics in *Staphylococcus epidermidis* Bacterial Biofilms. G.L. Gasper, R. Carlson, A. Akhmetov, J.F. Moore, L. Hanley.

Advanced Vacuum Society for Applied Surface Analysis, Penn State, Philadelphia, PA, 2008

Laser Desorption 7.87 eV Postionization Mass Spectrometry of Antibiotics in *Staphylococcus epidermidis* Bacterial Biofilms. G.L. Gasper, R. Carlson, A. Akhmetov, J.F. Moore, L. Hanley.